FUSION ENERGY SCIENCES
FY 2017 JOINT RESEARCH TARGET (JRT)
SUMMARY MILESTONE REPORT

By

S. Allen[1], Vlad Soukhanovskii[2], and Brian LaBombard[3]

[1] Lawrence Livermore National Laboratory @ DIII-D, Livermore, CA
[2] Lawrence Livermore National Laboratory @ NSTX-U, Livermore, CA
[3] Massachusetts Institute of Technology, Boston, MA
[4] Princeton Plasma Physics Laboratory, Princeton, NJ
[5] General Atomics, San Diego, CA

Prepared for the U.S. Department of Energy
DE-AC52-07NA27344[1,2], DE-FC02-99ER54512[3],
DE-AC02-09CH11466[4], and DE-FC02-04ER54698[5].

DISCLAIMER

This report was prepared as an account of work sponsored by an agency of the United States Government. Neither the United States Government nor any agency thereof, nor any of their employees, makes any warranty, express or implied, or assumes any legal liability or responsibility for the accuracy, completeness, or usefulness of any information, apparatus, product, or process disclosed, or represents that its use would not infringe privately owned rights. Reference herein to any specific commercial product, process, or service by trade name, trademark, manufacturer, or otherwise, does not necessarily constitute or imply its endorsement, recommendation, or favoring by the United States Government or any agency thereof. The views and opinions of authors expressed herein do not necessarily state or reflect those of the United States Government or any agency thereof.

Executive Summary

In support of the 2017 JRT, the DIII-D, NSTX-U and C-Mod teams performed coordinated research, focused on the subjects of dissipative divertor physics and divertor heat flux footprints. As evident in this report, good progress was made on many fronts toward assembling informed pictures of the plasma physics. The teams chose research topics that would best utilize the unique capabilities of DIII-D, NSTX and C-Mod – access to interesting divertor magnetic configurations and geometries, excellent diagnostic sets and extended parameter regimes. The research took advantage of dedicated experimental investigations on DIII-D and archived data analyses from NSTX and C-Mod – all targeted to address keys questions for tokamak power exhaust handling.

DIII-D dedicated significant run time to support the 2017 JRT. This included coordinated experiments to investigate an NSTX-like, high flux expansion divertor configuration to compare its detachment response to that seen in NSTX. DIII-D implemented divertor diagnostic upgrades as well and operated with a 'small angle slot' divertor to investigate this 'closed' divertor configuration. Follow-on experiments are planned to utilize these tools.

Analysis of archived data from NSTX and C-Mod was designed to exploit the wealth of information that had been collected during prior experimental campaigns. These investigations included the influence of high poloidal flux expansion on detachment onset (NSTX), magnetic flux balance dependencies of the power exhaust footprints (NSTX and C-Mod), power exhaust channel widths at poloidal magnetic fields greater than 1 Tesla, in the I-mode confinement regime and in response to divertor nitrogen seeding (C-Mod).

Preliminary results on all these topics are detailed in this report. Among these, some common themes emerged.

Approach to divertor detachment
In response to a programmed plasma density increase, the transition to a detached plasma state was seen to be abrupt in DIII-D and NSTX. Experimental results from DIII-D combined with modeling suggest that ExB drifts may play a role in setting up a bifurcated response. In NSTX, the effect of magnetic flux expansion on detachment onset was explored with data and modeling. High poloidal flux expansion (reduced x-point height) was seen to promote detachment of the outer divertor target in the experiment. Modeling produces a sharp 'cliff-like' transition to detachment for low poloidal expansion (increased x-point height) but a softer transition to detachment at high poloidal flux expansion. For this latter case, an increased impurity and Balmer line emission was predicted in the model, which is qualitatively consistent with experiment.

Sensitivity of separatrix density (and divertor detachment) to gas puffing; open versus closed divertor configurations
The influence of gas fueling location on the divertor detachment threshold was investigated in DIII-D with a divertor magnetic configuration very similar to what had been explored previously in NSTX – and with no divertor cryopumping. The divertor detachment threshold was found to be *insensitive* to the location of the gas puff in DIII-D

while NSTX experiments had found the divertor detachment threshold to be *sensitive* to gas puff location. The reason for the difference is likely connected to the separatrix density response. In DIII-D, the separatrix density increased in response to the gas puff at a rate independent of puff location. On NSTX, the separatrix density was found to be insensitive to gas puffs. This idea of separating the neutral pressure response in the divertor from and the core plasma density response has motivated, in part, the implementation of a closed, small angle slot divertor on DIII-D.

Divertor target heat flux response in near double-null configurations; sensitivity to divertor plate geometry

The NSTX and C-Mod teams examined the influence of upper-lower null magnetic flux balance on divertor target footprints. Both investigations found that the power e-folding length in the common flux region of the outer divertor leg is insensitive to magnetic flux balance. The 'spreading parameter', S, which is used to characterize the heat flux falloff in the private zone, was found to decrease sharply in NSTX as double-null is approached. In C-Mod, the profile in the private flux zone appears to be more appropriately described as a shorter e-folding length, rather than a spreading. Fitted values of S for the outer strike points were found to be insensitive to magnetic flux balance. In general, the values of S were found in C-Mod to be insensitive to divertor geometry – similar for the upper and lower divertors, despite the upper being a 'flat target plate' geometry and the lower being a 'vertical target plate' geometry.

Fusion Energy Sciences
FY 2017 Joint Research Target (JRT)
Summary Milestone Report

Annual Target: Conduct research to examine the effect of configuration on operating space for dissipative divertors. Handling plasma power and particle exhaust in the divertor region is a critical issue for future burning plasma devices, including ITER. The very narrow edge power exhaust channel projected for tokamak devices that operate at high poloidal magnetic field is of particular concern. Increased and controlled divertor radiation, coupled with optimization of the divertor configuration, are envisioned as the leading approaches to reducing peak heat flux on the divertor targets and increasing the operating window for dissipative divertors. Data obtained from DIII-D and NSTX-U and archived from Alcator C-Mod will be used to assess the impact of edge magnetic configurations and divertor geometries on dissipative regimes, as well as their effect on the width of the power exhaust channel, thus providing essential data to test and validate leading boundary plasma models.

Quarter 4 Milestone

Fourth Quarter: Consolidation of efforts of the analysis of previous data, along with the results of new experiments on DIII-D. Prepare a joint report documenting the progress made toward the joint research target goals.

Completion of 4th Quarter Milestone – Summary Report

The deliverable for the Office of Fusion Energy Science Joint Research Target milestone in FY17 was accomplished by experiments on DIII-D, including an experiment led by a NSTX-U staff member, and detailed analysis of C-MOD and NSTX-U data that was obtained previously. New divertor diagnostic measurements were developed on DIII-D during the year, along with an initial test of a new Small Angle Slot (SAS) divertor geometry. As both C-MOD and NSTX-U had a backlog of physics analysis of previous data on heat flux control and divertors, the FY17 JRT was an opportunity for these groups to focus on data analysis leading to a summary of the previous experiments.

One highlight of the JRT was that a NSTX-U researcher led an experiment on DIII-D to examine the effect of the location of gas puffing (used for divertor detachment) in a plasma shape that was similar to NSTX-U. Deuterium gas puffing is often used to increase the radiation in the divertor region, which in turn reduces the heat exhaust before it reaches the divertor plate. Preliminary analysis indicates that in contrast to NSTX-U results where the gas puff location is important, on DIII-D the plasma conditions are not significantly affected by the location of the gas puff.

On DIII-D, there was a concerted effort to add new diagnostics to address important physics issues of divertor detachment. The divertor "detaches" when the plasma near the divertor plate becomes very cold (~1 eV measured by Divertor Thomson Scattering (DTS) on DIII-D), the ion flux measured by Langmuir probes in the target plate decreases, and (most importantly) the divertor heat flux (measured by IR cameras on DIII-D) is reduced; in particular the peak heat flux is reduced. During the year, several important divertor diagnostics were developed. The first was calibrated coherence imaging to measure carbon (and Helium in Helium plasmas) flow profiles in the divertor and the main SOL; this work was completed during the run campaign and new data was obtained. These results will be presented as an invited talk at the upcoming American Physical Society Division of Plasma Physics conference (Samuell, et al.). The second was Divertor SPRED, an extreme ultraviolet (EUV) spectrometer to measure the main resonance lines of carbon and deuterium, along with molecular deuterium emissions. Comparison of fluid models of the Scrape Off Layer (SOL) and divertor (SOPLS and UEDGE codes) with experimental measurements of the total radiation have discovered that the codes underestimate the radiation, resulting in a so-called "radiation shortfall". As this effect is seen across multiple codes and machines (with different wall materials), it may point towards needed improvements in measurements and modeling of molecules. The installation of the Divertor SPRED instrument was completed at the end of the third quarter, commissioning was started at the end of the FY17 campaign, and initial data is expected from DIII-D in the FY18 campaign which starts in October 2017.

On DIII-D, a new Small-Angle-Slot (SAS) divertor was installed in FY17, and initial tests were completed. On DIII-D, control of the density is important to maintain the plasma below cutoff of the 110 GHz Electron Cyclotron Resonance Heating (ECRH)

system (possibly resulting in reflected power into diagnostic ports). However, one technique used to detach the divertor, gas puffing to increase the divertor radiation, results in an increase in the core plasma density. The goal of the SAS divertor, whose design was guided by SOLPS modeling, is to detach the plasma at a controlled (central) plasma density less than the ECRH cutoff. Initial results will be presented as an invited talk at the APS DPP meeting November 2017 (Guo).

Comparison of NSTX-U and DIII-D Divertor Detachment Experiment

Vlad Soukhanovskii, a NSTX-U researcher, planned and led a ½ day experiment on DIII-D in June: MP2017-08-02 "Divertor detachment NSTX/NSTX-U Similarity Plasmas for JRT 2017" This was the first experiment in the NSTX-U experimental campaign on DIII-D (the "-08-" in the experiment number denotes an experiment in this campaign). This experiment was motivated by several observations on NSTX-U during deuterium gas puffing used to detach the divertor.

- Access to stable partial detachment was facilitated in the strongly shaped NSTX-U plasmas (comparing divertor characteristics in weakly and strongly shaped configurations)
- Density ramps up to the Greenwald density did not produce any partial detachment
- Stable partial detachment was obtained only with additional divertor gas injection
- Midplane gas injection at the same rate resulted in transient partial detachment during the gas flow, and re-attachment without the gas flow
- Experiments with varying poloidal angle in the strongly-shaped configuration suggested that partial detachment onset was affected by the angle between the magnetic field and the divertor target. The angle controls where the recycling flux is directed, i.e., toward or away from the separatrix. When the angle is below 90 degrees and the recycling flux is directed toward the separatrix, the configuration attains the properties of the vertical plate divertor. In addition, the magnetic configuration and its transparency to neutrals (and the ability to entrap them) plays a role.

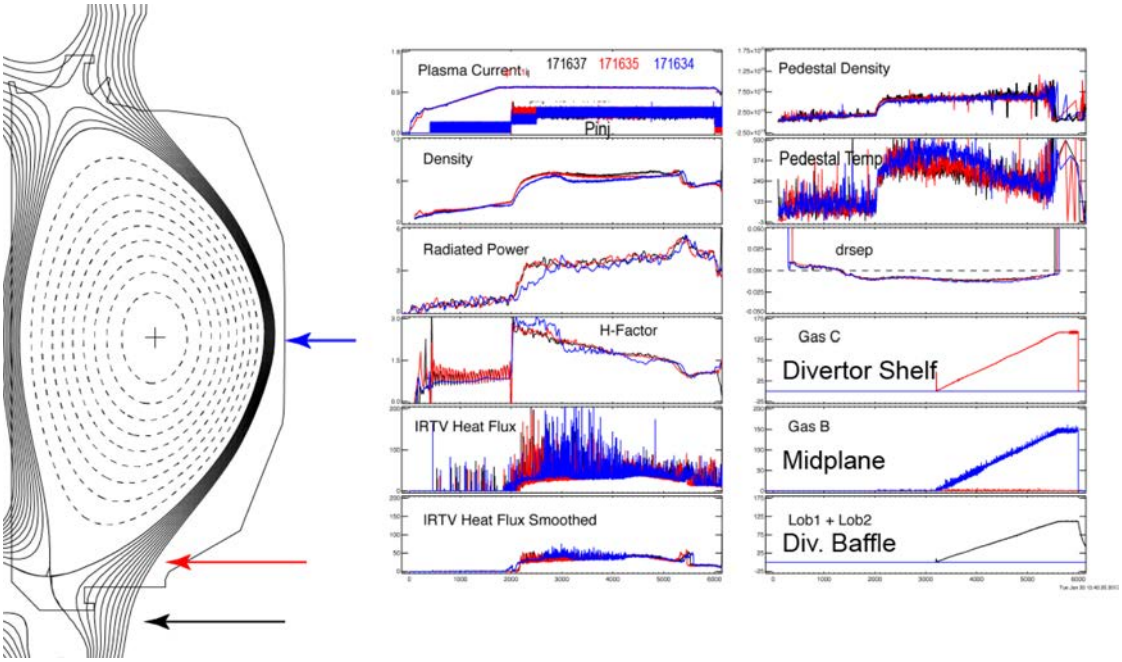

Figure 1. The NSTX-U plasma shape in DIII-D. Three gas puff locations used for divertor detachment were compared in these three shots. In contrast to NSTX-U results, the plasma conditions on DIII-D (in the NSTX-U shape) are not sensitive to the location of the gas puff used for detachment. This is consistent with previous DIII-D results in lower triangularity plasmas.

Preliminary results from the DIII-D experiment are summarized as follows.

- An NSTX-like high-triangularity double null shape with strong bias toward the lower divertor (and ion grad B drift toward the lower divertor), and with high divertor poloidal flux expansion was developed. The 4MW, 1 MA H-mode target plasma was used to study how divertor detachment characteristics depend on the poloidal gas injection location. Three gas injectors were used, as shown in the Figure 1, one midplane injector, one far-scrape off layer (SOL) injector, and one divertor injector in the vicinity of the outer strike point.
- Density control in the discharges with gas puffing proved to be difficult as the lower cryo-pump was not used in this experiment. The experiment aimed at using the H-mode with basic lower density and added gas injection rate ramps from 0 to 150 Torr L/s. It was expected that at some point in the ramp, the increasing density would reach the detachment onset threshold. Analysis of the divertor data, namely the heat flux profiles from infrared (IR)TV, divertor Balmer spectroscopy, divertor C III and D_α camera data and Langmuir probes indicated that a partial detachment was induced with each of the three injectors. However, preliminary observations suggest that the

deuterium gas puff location used to detach the divertor had much less influence on DIII-D than on NSTX.

The short, preliminary summary is that it appears that the gas injection location used for divertor detachment affects the plasma conditions on NSTX-U, while on DIII-D (with the NSTX-U shape) the results are much less sensitive. More details are presented as part of the overall NSTX analysis.

Participation in International Tokamak Physics Activity: Divertor and SOL

The ITPA group focused on the Divertor and SOL includes US members Russell Dorner (UCSD), Mike Jaworski (PPPL), Brian La Bombard (MIT), Tony Leonard(GA), and Maxim Umanski (LLNL). Houyang Guo of DIII-D is the chair of the group, and a meeting was held in May, 2017. There were several presentations relevant to the JRT research, including: *Modeling C-MOD Detachment using SOLPS-ITER with Drifts* by W. Dekeyser, *Updated Analysis and Final Experiment for Alcator C-MOD Ne and Ne-Seeded H-modes* by M. Reinke, and *C-Mode Heat Flux Width at B_p above 1 T* by D. Brunner. Some of these results are included in the C-MOD analysis section of this report. DIII-D postdoc Aaro Jaervinen also presented *Experimental and Numerical Investigations of the Impact of Cross-field Drifts on Divertor Detachment Characteristics in DIII-D*, and a summary of this presentation follows, as it is particularly relevant to divertor detachment research on DIII-D.

Dedicated analysis efforts were conducted to understand the impact of cross-field drift effects on the onset of outer divertor target detachment in DIII-D. In lower single null L-mode plasmas at 1.3 MA and 2.1 T, the outer target reaches target electron temperature lower than 2 eV, indicative of the onset of detachment, at 10% *lower* upstream density when the $\mathbf{B}\times\nabla B$-drift is towards the divertor (forward B_T) than when the $\mathbf{B}\times\nabla B$-drift is away the divertor (reversed B_T) (Fig. 2a, b). This finding is qualitatively consistent with UEDGE simulations including cross-field drifts (Fig. 2b). The UEDGE simulations indicate that in the forward B_T configuration, the radial $\mathbf{E}\times\mathbf{B}$-drift accumulates particles from the common SOL towards the strike point increasing density and reducing temperature in this region, therefore, facilitating onset of

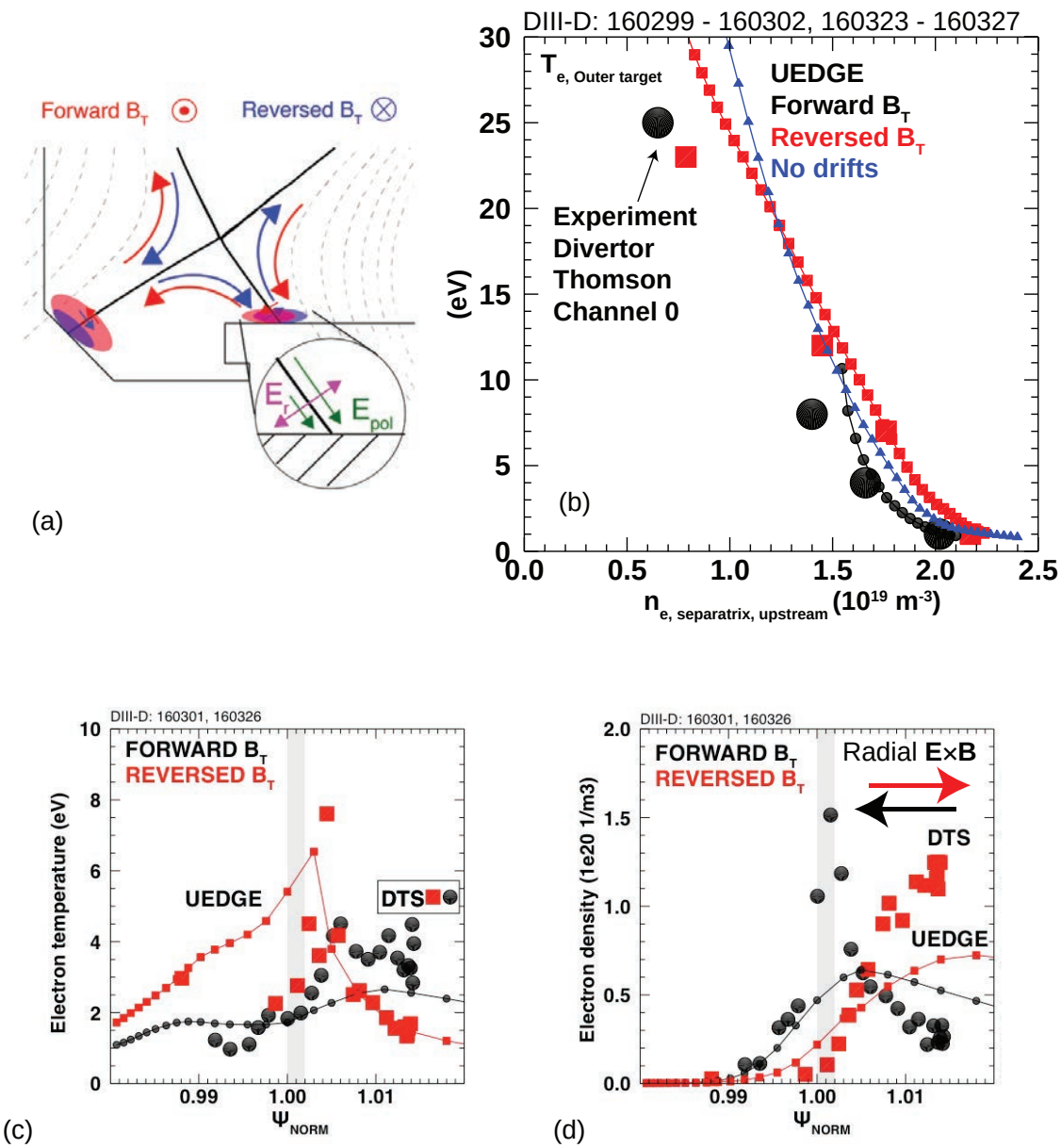

Figure 2. (a) Schematic of cross-field drift directions in forward B_T (red) and reversed B_T configurations. (b) Measured (solid circles and squares) and predicted (connected solid symbols) outer target peak electron temperature as a function of upstream separatrix electron density in L-mode conditions. Black color symbols represent forward B_T configuration, red color symbols represent reversed B_T configuration, and blue symbols are used for simulations without cross-field drifts. (c, d) Comparison of measured and predicted electron temperature (c) and density (d) profiles at the outer target. The strike point region is illustrated with a grey bar.

detachment at lower upstream density (Figs. 2c, d). In reversed B_T configuration, on the other hand, the radial **E**×**B**-drift leads to particle transport form the strike point region towards the far SOL, reducing the strike point density and increasing the temperature,

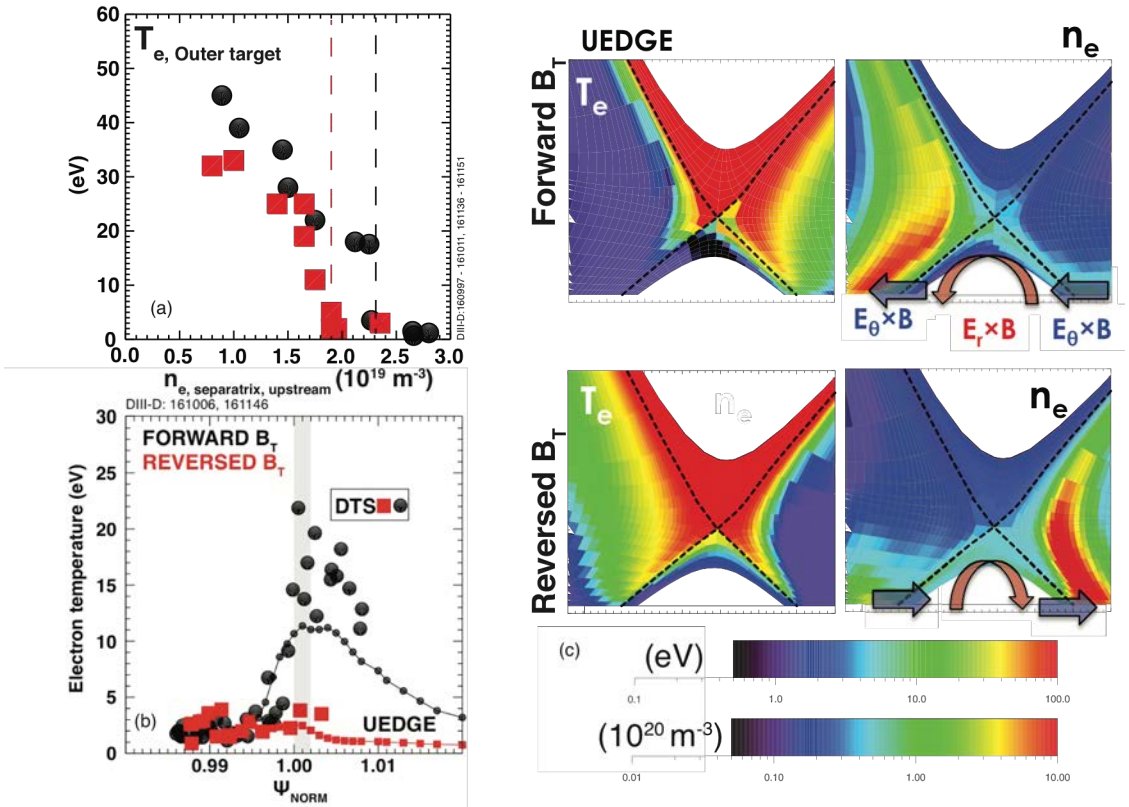

*Figure 3. (a) Measured outer target electron temperature as a function of upstream separatrix electron density in H-mode conditions. Black circles represent forward B_T plasmas and red squares represent reversed B_T plasmas. (b) Measured and predicted outer target electron temperature profiles at a measured upstream separatrix density of 2.2×10^{19} m^{-3}. (c) Predicted 2D profiles of electron temperature (left column) and electron density (right column) in forward B_T (upper row) and reversed B_T (lower row) configurations. The poloidal (red) and radial (blue) **E**×**B**-drifts are schematically illustrated on the 2D electron density profiles.*

therefore, increasing the upstream density required for onset of detachment (Figs. 2c, d). Although, the simulations do capture qualitatively the impact of cross-field drifts on the detachment threshold, the peak densities in front of the outer target are still underestimated by a factor of 2 (Fig. 2d).

On the other hand, in H-mode plasmas at 0.9 MA and 1.8 T with 4 MW of input power, the outer target reaches target electron temperature lower than 2 eV at 20% *higher* upstream density when the **B**×∇B-drift is towards the divertor (forward B_T) than when the **B**×∇B-drift is away the divertor (reversed B_T) (Fig. 3a). This observation is also qualitatively consistent with UEDGE predictions including cross-field drifts (Figs. 3 b,c). In H-mode conditions, the UEDGE simulations indicate that the relatively strong poloidal **E**×**B**-drift in the private flux region below the X-point drives strong in-out asymmetric

transport between the divertor legs. This flow circulation reduces densities and increases temperatures in the outer target for a given upstream density in forward B_T, therefore increasing the upstream density required for the onset of outer target detachment (Fig. 3c). In reversed B_T, in contrast, the poloidal **E**×**B**-drift in the private flux region leads to particle accumulation towards the outer target, increasing densities and reducing temperatures in the outer divertor, therefore reducing the upstream density required for the onset of detachment.

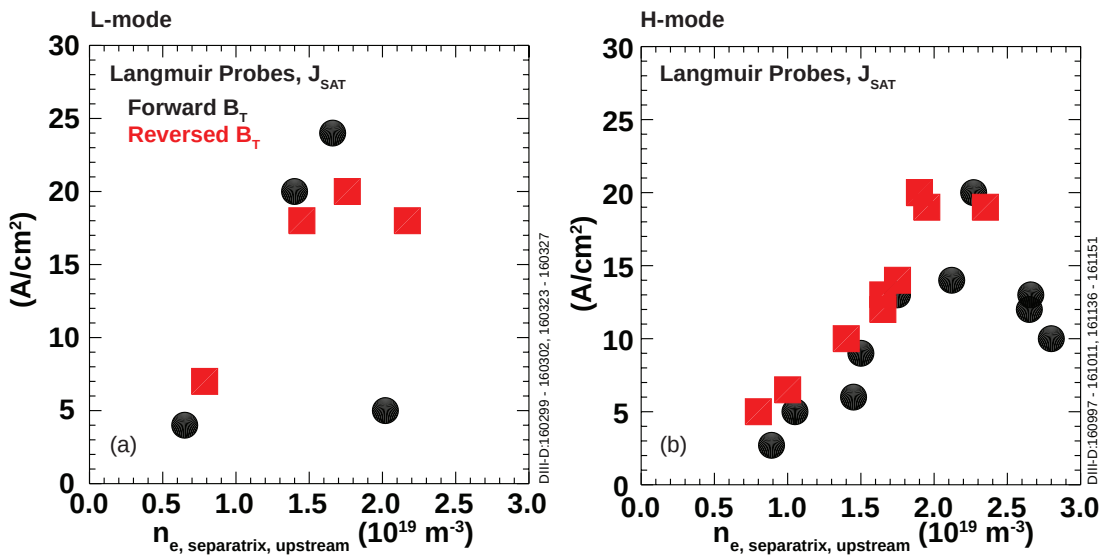

Even though the onset of detachment at the outer target, defined as $T_{e,\ target} < 2$ eV, has an opposite dependence on toroidal field direction in L- and H-mode plasmas, both in L- and H-mode plasmas, the forward B_T configurations reach a strong outer target saturation current roll-over, whereas the reversed B_T configurations show saturation only of outer target saturation current (Figs. 4 a,b). Since most of the operational tokamaks do not have a divertor Thomson system, roll-over of the target saturation current is often used as an indicator of divertor detachment. However, in this series of plasmas this would lead to confusing conclusion in the H-mode series, since the divertor Thomson indicates that the reversed B_T reaches outer target temperatures below 2 eV at 20% lower upstream separatrix density than the forward B_T configuration, whereas based on the outer target saturation currents one could conclude that reversed B_T configurations struggle to detach at the outer target in both L- and H-mode conditions (Figs. 3a, 4). The root causes of the shallow saturation current roll-over in reversed B_T are still a subject of research.

However, the leading hypothesis is that the radial **E**×**B**-drift in the outer divertor leg depletes the outer strike point region from density in reversed B_T limiting the density build up at the onset of detachment. This limits the degree of detachment and the saturation current roll-over.

In H-mode conditions in the forward B_T configuration, the outer target typically undergoes a rapid onset of detachment, where the outer target electron temperature drops from 10 – 20 eV down to 1 eV abruptly with increasing upstream density (Fig. 3a). There is no operational space between these two divertor condition states. This type of step transition between the attached and detached divertor conditions would be a significant challenge for the active control systems in the next step devices aiming to avoid strong transient re-attachment as well as overshoot of divertor detachment at all times during the operation. The UEDGE simulations with full cross-field drifts conducted within this project are the first series of 2D multi-fluid simulations that qualitatively capture this step-like onset of detached conditions. The simulations indicate that the interdependence of divertor conditions and **E**×**B**-drifts can drive a strongly non-linear transition from well attached outer target conditions to deeply detached outer target conditions. In attached divertor conditions, the radial and poloidal potential gradients in the divertor drive strong **E**×**B**-drift fluxes from the outer divertor to the inner divertor (Fig. 5). These fluxes are of the order of 10 – 20% of the total ionization rate in the outer divertor common SOL (Fig. 5). These fluxes help to maintain low density, high temperature divertor conditions with increasing upstream separatrix density. At sufficiently high upstream separatrix density, another stable divertor solution exists, where the divertor has evolved to high density, low temperature, deeply detached conditions with significantly diminished **E**×**B**-drift circulation between the divertor legs (Fig. 5). In the simulations, the divertor conditions are bifurcated between these two conditions. In the experiment, the plasmas at the detachment threshold show dithering detachment characteristics, which may suggest that the sources of fluctuations in the experiment are sufficient to enable the divertor solution to jump between the two conditions.

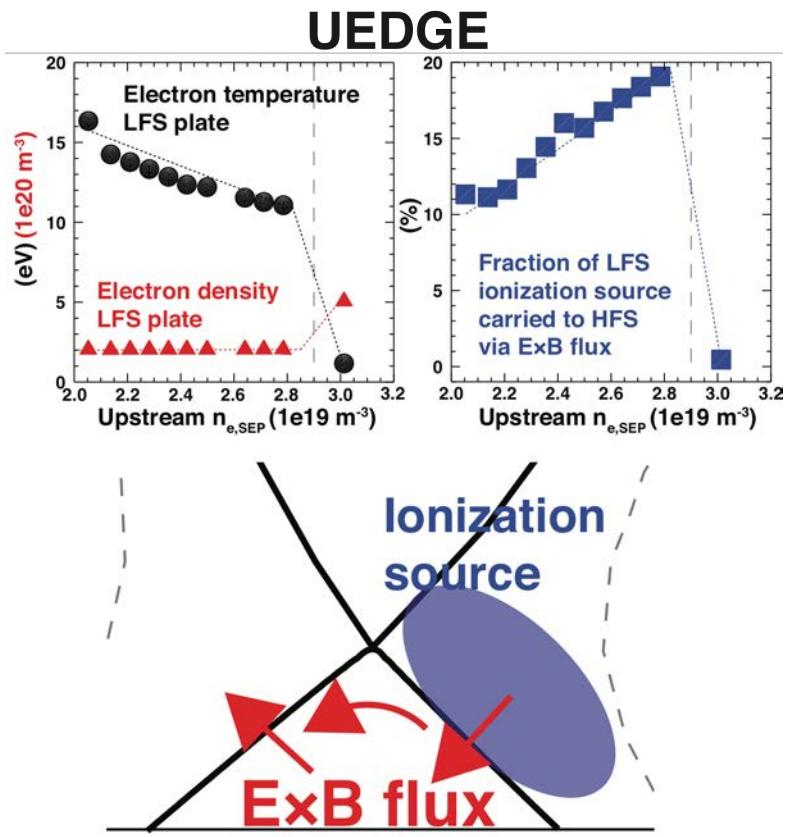

Figure 5. Predicted electron temperature (black), density (red), and fraction of low field side (LFS, outer divertor) ionization source carried to the high field side (HFS, inner divertor) with the ***E****×****B*** *circulation in the divertor. The schematic below illustrates the ionization source and the* ***E****×****B****-drift circulation.*

In the investigated series of forward B_T H-mode plasmas, the detachment front propagated all the way to the X-point as the divertor detached. However, H-mode detachment experiments at higher X-point elevation, 1.3 MA, 2.1 T, and 6 MW showed that the detachment front did not reach X-point elevation at detachment. This indicates that there are yet unresolved dependencies of the detachment stability and ionization front structure on plasma current, toroidal magnetic field strength, heating power, and/or X-point elevation. Dedicated experiments in FY18 are planned to address some of these dependencies.

DIII-D Experiments in 2017

Recall that DIII-D has two research thrusts that are directly related to this JRT. The first is DIII-D Thrust 2: Understand the Impact of Geometry and Fueling on Divertor, Pedestal, and Scrape-off layer (SOL) Dynamics. During the fall 2017 DIII-D maintenance period, the new General Atomics (GA) small angle slot (SAS) divertor design was installed at the top of the main chamber near the upper divertor. The run time for the checkout of this new divertor was included in this thrust (Thrust 2). In addition, a second thrust DIII-D Thrust 3: Detachment physics, focused on the discrepancies in the measured compared with the modeled divertor quantities, particularly the radiation, in both attached and detached divertor operation. A new EUV spectrometer was installed to measure D, C, and D_2 emissions. This thrust would also include other new measurements helpful to characterize a detached divertor plasma, such as impurity ion flow.

It is anticipated that approximately two weeks of DIII-D experiments planned by the NSTX-U team will be executed between FY17 and FY18. Some of these will contribute to the JRT research, as the proposal for the joint experiment discussed above has an additional ½ day dealing with variations in divertor shape.

DIII-D exceeded its run time target of 17 weeks for FY17, and several experiments in Thrust 2 and Thrust 3 were completed.

DIII-D Thrust 2: Understand Impact of Geometry and Fueling on Divertor, Pedestal, and SOL Dynamics. 5 run days.

- During the first quarter, the installation of the GA SAS divertor at the top was completed and the DIII-D vessel was pumped down at the beginning of January 2017. This was the major installation task during the maintenance period (Fig. 6).
- Optimize SAS operation to achieve detachment at lower upstream density, validate code predictions, and do deuterium puffing into the SAS divertor. (3.5 days) – two days of this plan were completed in the second quarter, and preliminary analysis was completed.
- Effects of divertor closure on detachment and pedestal (1.5 days) – these experiments were completed during the third quarter, and detailed analysis is in progress.

Figure 6. Installation of the GA SAS-1 divertor was completed in the first quarter, and experiments were performed in both the second and the third quarters. Detailed analysis is in progress.

Diagnostic Development for Closed and Slot Divertors

The measurement of total divertor power dissipation to compare with SOL models is provided by bolometry (for total radiation) and target heat flux profiles (for the total power to the solid target). A PVR led by Auna Moser (GA) in June 2017 had the goal to substantially increase bolometer coverage to the upper divertor and the SAS divertor. The top priority was to measure total radiated power in each divertor, while the secondary priority was to measure the spatial distribution of radiated power. For this reason, two arrays of tangential viewing chords were chosen (Fig. 7) for adequate coverage of both the upper divertor (red) and SAS divertor (green).

Two test radiation distributions were simulated in both divertors. A calculated spatial response matrix, written by Bill Meyer (LLNL), was used for the new bolometer chords in forward projection mode to create a virtual bolometer diagnostic. From this virtual diagnostic, the line-averaged intensity was calculated for each viewing chord. As seen in Figure 8, both chord arrays correctly registered each radiation distribution, and the chord arrays were in good agreement on the location of the peak radiation.

Surface-eroding thermocouples (SETCs) are also in the process of being tested in DIII-D as an alternative to IR imaging of heat flux profiles, especially in closed divertors with limited viewing angles. A Physics Validation Review was conducted by Jun Ren (UT-Knoxville) to explore this potential. Initial results from profile sweeping showed that the SETC temperatures rise and fall with changes in the incident heat flux, but the original signal-to-noise ratio was too low. Additional shielding of the electronics greatly helped improve the ratio. The SETCs also exhibited changes in readings with the onset of ELMs, demonstrating the potential of their fast response time to resolve transient heat fluxes.

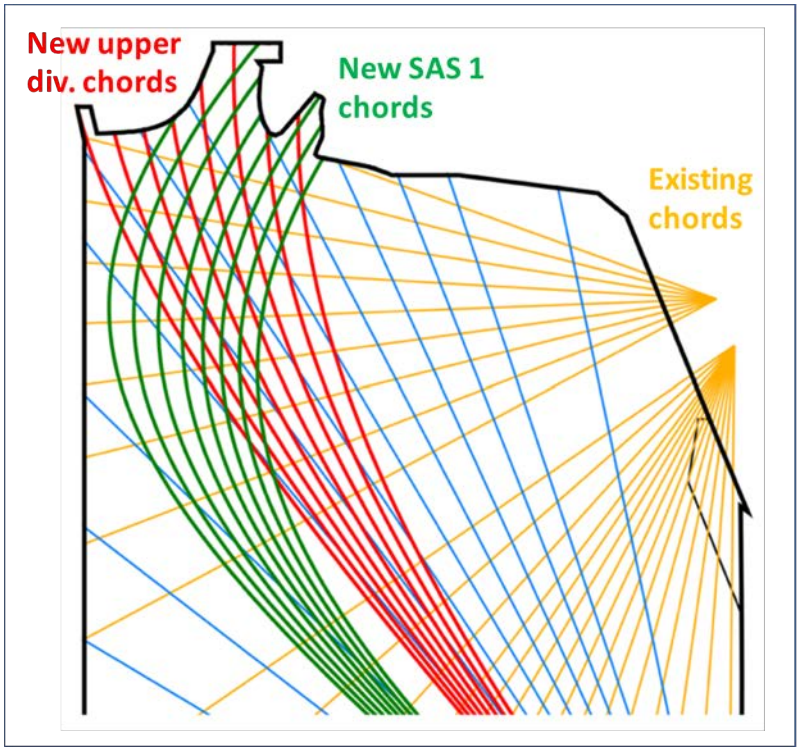

Figure 7. New tangential viewing chords in the upper divertor (red) and SAS divertor (green) will enable bolometer measurements of total radiated power in these closed configurations.

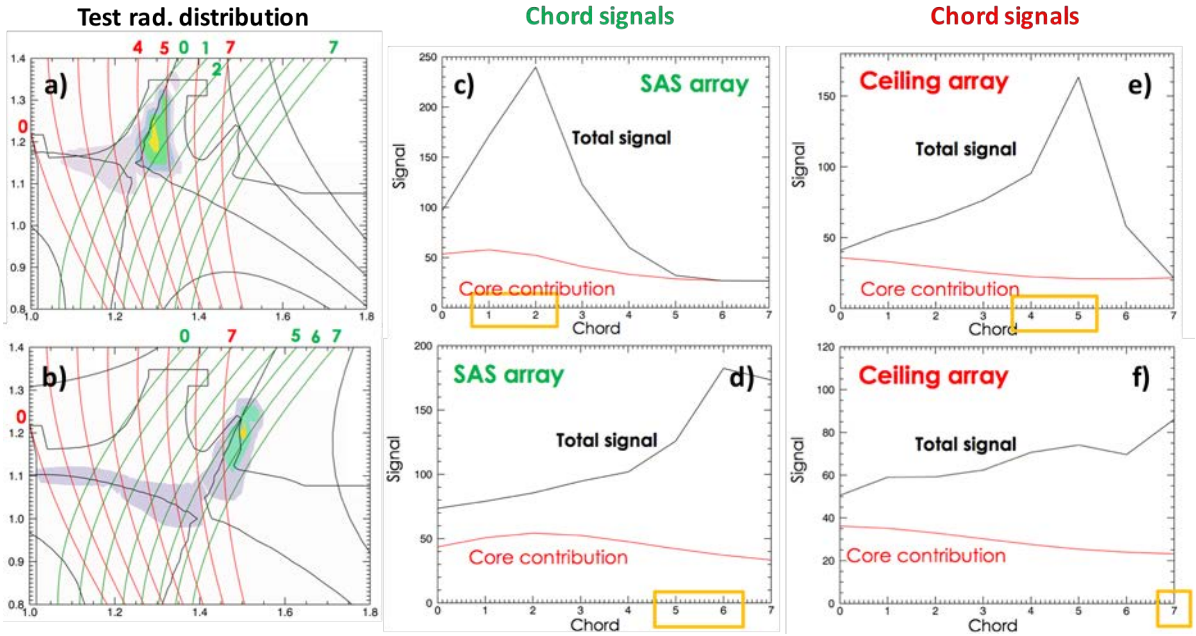

Figure 8. Two radiation distributions (a-b) were simulated to test the sensitivity of the new tangential viewing chord arrays in the upper divertors. Both arrays correctly registered each distribution, and the SAS array (c-d) agreed with the ceiling array (e-f) in identifying the region of peak radiation (at the respective chords boxed in yellow).

<u>DIII-D Measurement of Divertor Detachment in Closed Divertors</u>

Due to the geometric constraints of a closed divertor, it is in general difficult to use the normal signatures of detachment: drop in T_e measured by DTS, movement of the CIII radiation zone (~ 7 eV) from the divertor plate, with subsequent reduction in the divertor heat flux. Therefore, it is useful to develop other signatures of divertor detachment than can be used in a closed divertor. As DIII-D has the only DTS system, other machines often use the ion saturation current from Langmuir Probes installed in the target plates as a detachment signature; historically the reduction compared to the prediction of a simple two-point SOL physics model was used as a "degree of detachment". A divertor closure experiment conducted on DIII-D (Auna Moser (GA) and Morgan Shafer (ORNL) in June), showed that pressure changes measured by ASDEX gauges in the upper divertor were correlated with detachment onset, showing a marked increase in measured neutral pressures as the CII radiation front began to migrate away from the target (Fig. 9). This correlation could serve as a useful signal for detachment in closed divertors with limited spectroscopic views. Additional evidence of the capability of the ASDEX gauges to indicate detachment was found when examining the trend of

Langmuir Probe ion saturation current with increasing core plasma density. Coincident with the rollover of the ion flux (i.e., a loss of ion flux to the target), the ASDEX gauge again registered an distinct increase in the measured neutral pressure (Fig. 10).

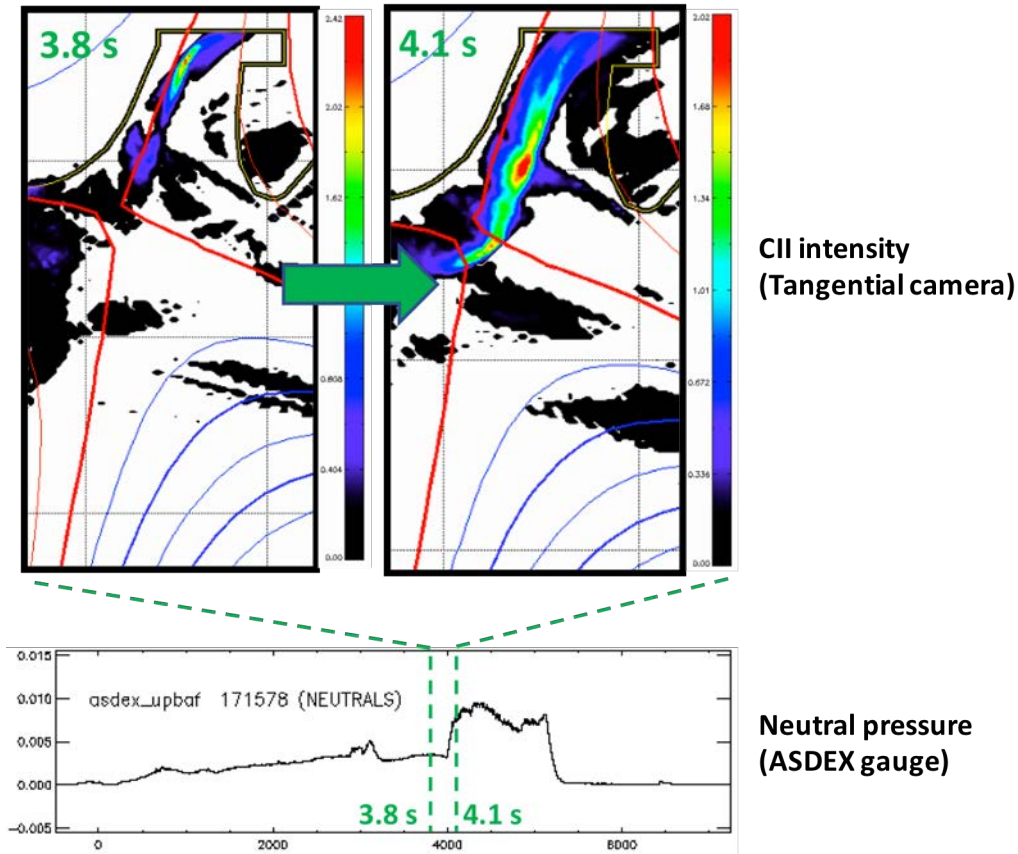

Figure 9. In Shot 171578, the divertor radiation front, as visualized by a tangential camera filtered for CII emissions (top), moves away from the upper ceiling, signaling detachment onset. This event coincides with a sharp increase in divertor neutral pressures as measured by the ASDEX gauge (bottom). This correlation points to ASDEX gauges as a promising diagnostic for registering detachment in closed divertors with limited spectroscopic views.

Anticipating the value of neutral measurements to determining detachment in a closed divertor, a PVR was held by Morgan Shafer (ORNL) in April for ASDEX gauges to make neutral pressure measurements in the SAS divertor. SOLPS modeling by Brent Covele (GA) had shown that the SAS slot restricted atomic and molecular deuterium to highly localized pockets. This modeling result was used to guide the choice of locations for neutral pressure measurements in the SAS slot (Fig. 11).

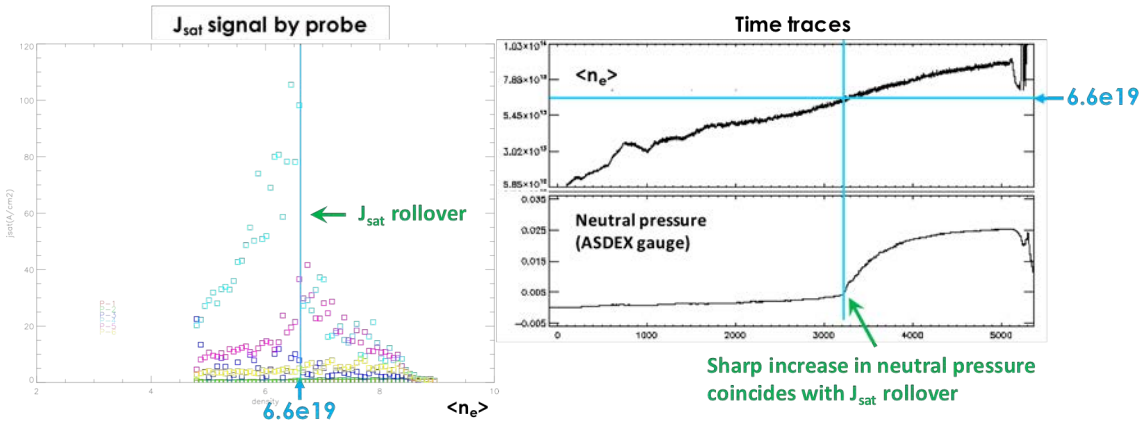

Figure 10. In Shot 171581, ion saturation current rolls over at a line-averaged density of 6.6e19 m^{-3} (left), signaling detachment onset. At the same time in the density ramp, the ASDEX gauge registers a sharp increase in divertor neutral pressure. This is further confirmation that higher neutral pressures are indicative of detachment, and that ASDEX gauges can be used to register detachment in closed divertors.

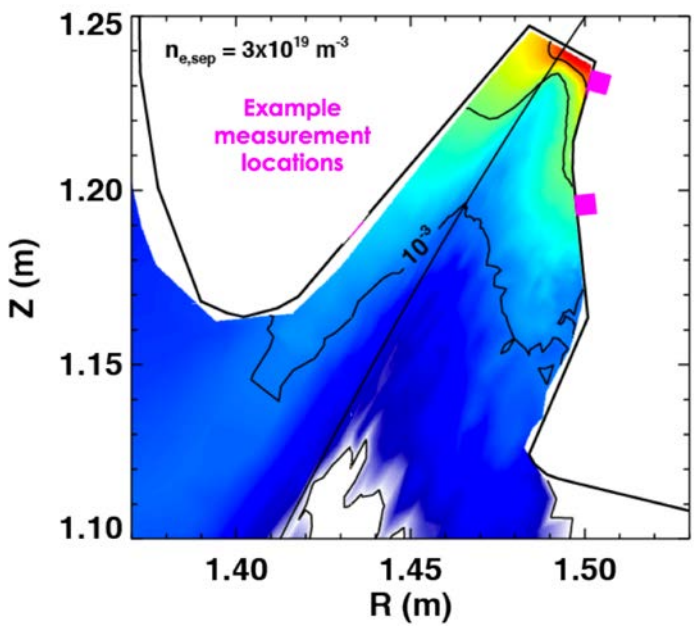

Figure 11. Eirene calculations from the SOLPS code indicate that the SAS divertor creates highly localized pockets of high neutral pressure in the slot. Consequently, ASDEX gauge measurements will be taken in locations (magenta) likely to be associated with partial detachment and full detachment from these concentrated neutrals

While ASDEX gauges can resolve changes in neutral pressures on fast timescales appropriate for measuring changes to the plasma-neutral interaction, other types of gauges enable different types of measurements. Penning gauges were refurbished and reactivated in the upper outer and

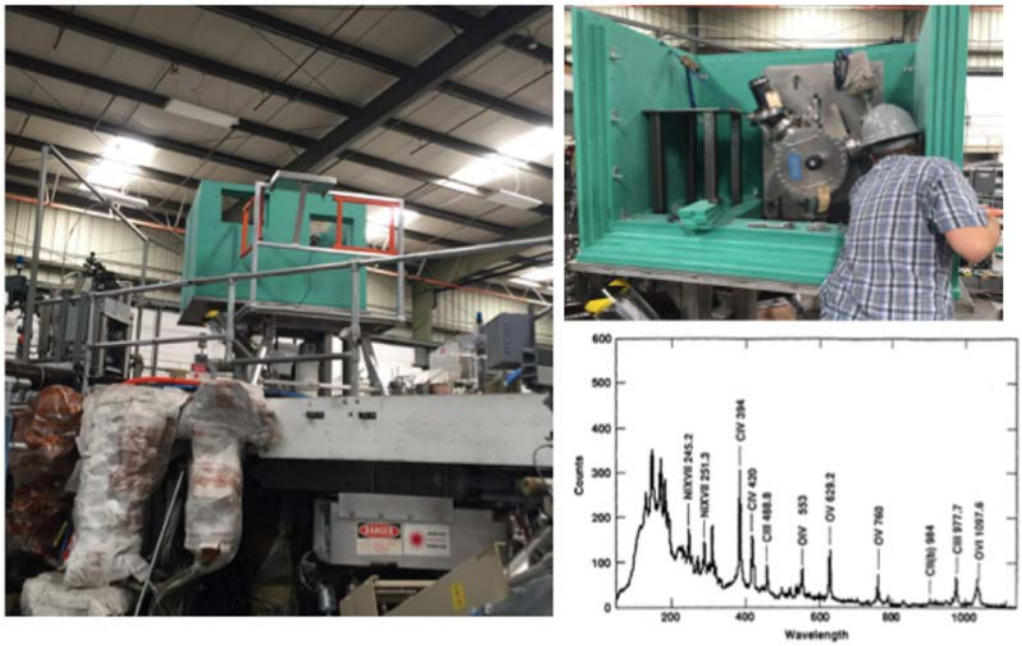

Figure 12. During the third quarter, most of the Divertor SPRED assembly was installed on DIII-D, including the neutron shielding. Commissioning was nearly completed in the fourth quarter, just as the FY17 DIII-D run time target was achieved. The system will be ready for operations in November, 2017. Expected spectra shown at lower right.

lower pump ducts in DIII-D in the spring of 2017 by Edward Hinson (UW-Madison). These allow measurement of impurity partial pressures in the pumping plenum. The gauges have been used to measure N_2, Ar, Ne, and He pressures in a number of experiments in the FY17 campaign, and are scheduled for use in FY18 experiments as well.

<u>DIII-D Thrust 3: Address Critical Detachment Physics Models. - 4 run days.</u>

An important new measurement of the divertor deuterium and impurity emissions will be provided by an extreme ultraviolet (EUV) spectrometer viewing the lower divertor (Fig. 12). The instrument was installed at DIII-D during the third quarter, and commissioning started in the fourth quarter. This SPRED commissioning was nearly completed in FY17 just as the DIII-D run time target was achieved. To allow more time for diagnostic checkout, the experiments involving the SPRED were deferred to the FY18 run campaign. As the time period between the end of FY17 and the beginning of the FY 18 experiments is very short (the vent lasted two weeks), these experiments will only be delayed by about two months, and will be in first part of the FY18 run campaign in October, 2017. These experiments include:

- Impact of deuterium emission on the radiation shortfall (1 day).
- Detachment physics at maximum SOL heat flux (0.5 Day)
- Impurity assisted detachment in forward and reverse toroidal field (1.5 days)
- SOL flow imaging (new calibration laser for flow diagnostic) (1 day)
- The calibration laser for the flow diagnostic was completed and used during the second quarter of FY17.

Another important diagnostic required for divertor detachment experiments including detachment with particle drifts is the Coherence Imaging System (CIS) used to measure carbon flow in both the divertor and the main SOL. During the previous quarters, a new laser calibration system has been developed and installed. During the third quarter, this system was used for routine calibrations between shots. This calibration technique (tuneable laser and high precision

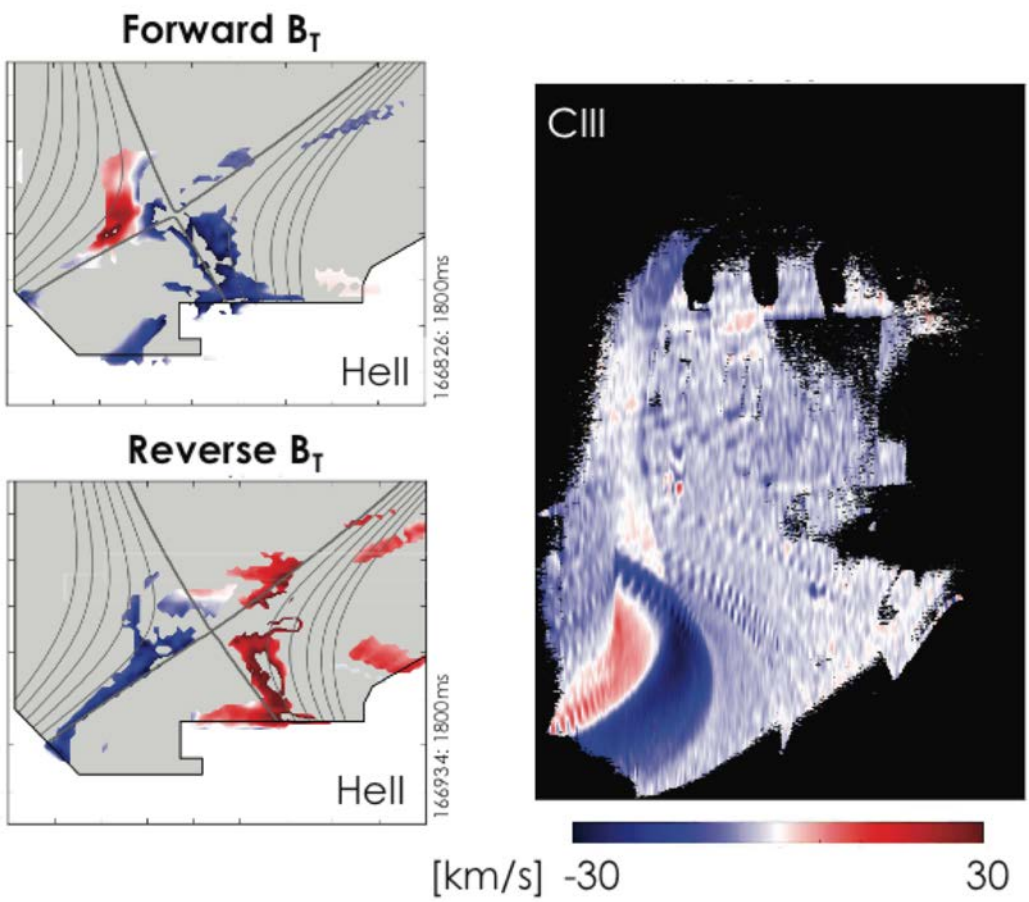

Figure 13. 2D reconstruction of HeII based flow image in the lower divertor in forward and reversed toroidal field configurations as well as periscope view of CIII flow image in a helium plasma.

wavemeter 465.90000 nm) reduces the uncertainty in the carbon ion flow velocity by over an order of magnitude, to approximately 0.1 km/s in plasmas with a mean velocity of 10's of km/s. In addition to measuring the C 2+ ion flow, this system can measure the Helium (main ion) flow in helium plasmas. A run day in helium is scheduled so that both ion species can be measured on alternate shots with similar conditions. This will address the entrainment of the carbon impurity in the Helium divertor plasma.

Precise measurements of divertor electron density and temperature via Thomson scattering (TS) have been critical to characterizing changes in transport in the SOL and are the "gold standard" for divertor detachment on DIII-D. The TS laser has a new vertical measurement location at R = 1.33 m, in addition to its other major radii, 1.49 m and 1.94 m (Fig. 14). This new capability allows for electron density and temperature measurements in divertors with longer legs, greater flux expansion, and greater closure on the lower divertor floor. For this purpose, a spatial calibration of 8 new viewing chords was completed. The same calibration was also completed for 8 new viewing chords in the Small-Angle Slot (SAS) divertor [7] at R = 1.49 m.

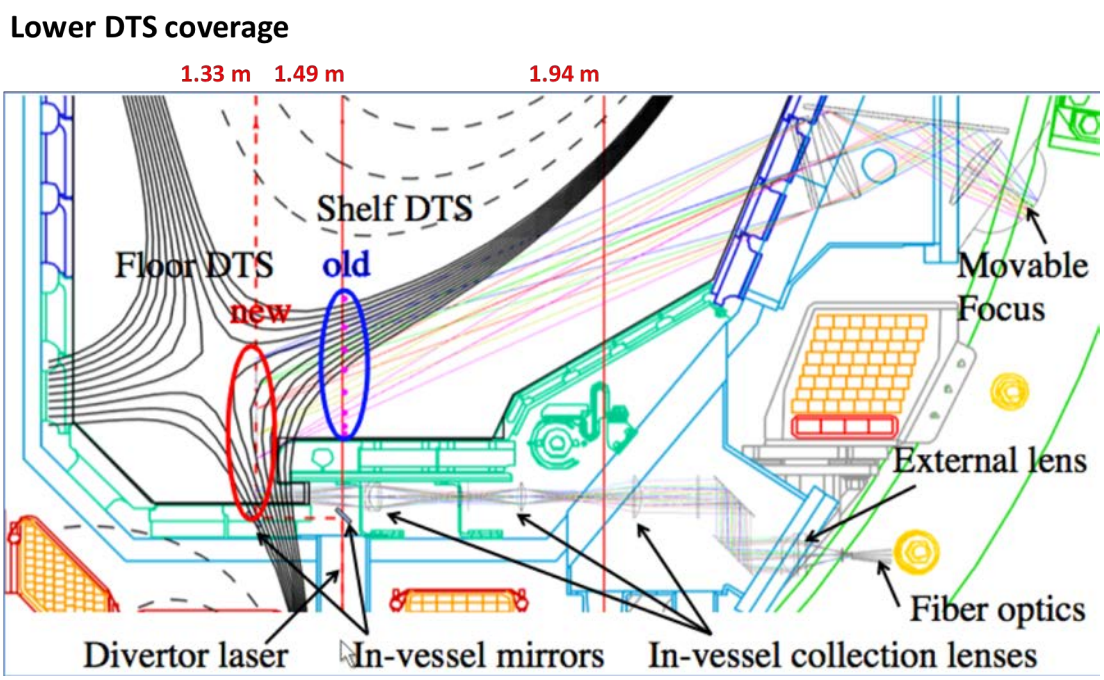

Figure 14. In-vessel mirrors permit use of the DTS laser at R = 1.33 m on the lower floor (circled in red). This new capability enables high-fidelity electron density and temperature measurements for a much wider range of divertor geometries.

National Spherical Torus Experiment Upgrade Data Analysis

NSTX-U Summary

A successful high-performance plasma operation with a radiative divertor has been demonstrated on many tokamak devices, however, significant uncertainty remains in accurately modeling detachment thresholds, and in how detachment depends on divertor geometry. Whereas it was originally planned to perform dedicated divertor experiments on the National Spherical Tokamak Upgrade to address critical detachment and divertor geometry questions for this milestone, the experiments were deferred due to technical difficulties. Instead, existing NSTX divertor data was summarized and re-analyzed where applicable, and additional simulations were performed.

Divertor studies in the *geometrically open* standard divertor configuration in NSTX can be summarized as follows:

- Core density ramps up to the Greenwald density did not produce outer strike point detachment;
- Stable outer strike point partial detachment was obtained only with additional divertor gas injection;
- Midplane gas injection at the same rate (cf. divertor gas injection) resulted in transient partial detachment during the gas flow, and re-attachment without the gas flow;
- Access to stable partial outer strike point detachment was facilitated in the strongly shaped plasmas.

These finding suggest a way to optimize the open divertor for partial outer strike point detachment, by placing the neutral gas source in the vicinity of the strike point, directing the recycling neutrals toward the separatrix (by adjusting the poloidal separatrix angle), and entrapping the neutrals in the high poloidal flux expansion configuration (via plasma plugging).

Significant attention has been given to trying to understand the power scrape-off layer (SOL) width, λ_q, and how it scales to larger more powerful tokamaks. Due to their compact nature, spherical tokamaks (STs) may need to operate in a double-null (DN) configuration to reduce heat fluxes on plasma facing components (PFCs). However, tokamaks with a larger aspect ratio have been primarily focused on lower single null (LSN) discharges which is the baseline operating

scenario for ITER. Consequently, few experiments have focused on λ_q behavior in DN scenarios. Results presented here show distinct differences between LSN and DN plasmas. The S parameter, which describes how much incident heat flux diffuses into the private flux region, is found to be systemically higher in LSN than in DN NSTX plasmas. While λ_q itself remains unchanged between LSN and DN plasmas. A minimum in power deposited onto the lower, outer strike point of 10 – 25% P_{SOL} is found when $-2 \leq \delta_r^{sep}/\lambda_{q||,\,OMP} \leq 2$, i.e., very near DN. Full power accounting in NSTX-U is planned for increased IR coverage of all divertor strike points.

NSTX-U Perspectives on Divertors and SOL

Based on nearly five decades of magnetically confined nuclear fusion plasma physics research, an axisymmetric poloidal magnetic X-point divertor has emerged as the most promising vision for a tokamak plasma-material interface (PMI). The poloidal divertor enables energy and particles lost from the confined core plasma due to radial transport and magnetohydrodynamic (MHD) instabilities (e.g., edge localized modes (ELMs)) to flow to the divertor chamber, which acts as a separate plasma-material interface. Cross-field transport in the edge and scrape-off layer (SOL) is generally anomalous (higher than collisional (Bohm) transport enhanced by neoclassical effects). Recent work highlights the intermittent nature of SOL transport: filamentary structures carry particles at high rates in the SOL. The divertor SOL parallel heat transport is dominated by electron conduction and convection and strongly depends on plasma collisionality. At higher plasma collisionality, a low-temperature highly radiative divertor plasma regime sets in: the plasma flowing to divertor plates loses energy through radiation and dissipative processes, and momentum through charge exchange, inelastic collisions and recombination. This leads to significant plasma neutralization before contacting the divertor plate surface (i.e., detachment), and, as a result, significantly reduced heat load and material erosion. This radiative regime is commonly called radiative plasma detachment, or divertor detachment. It is characterized by a parallel SOL electron (plasma) pressure drop, high neutral divertor pressure (density), low plasma electron temperature ($T_e \leq$ 1-2 eV) and high electron density at the plate, leading to high impurity radiation. Divertor detachment is viewed as the primary potential solution to tokamak power and particle exhaust given our present understanding of the operating limits of plasma-facing component cooling technology and target materials. The proposed ITER divertor is based on standard X-point divertor geometry designs

tested in large tokamak experiments: vertical targets with partial radiative detachment of the strike points are envisioned.

The NSTX Upgrade restarted plasma operations in FY2016. In preparations for the FES Joint Research Target 2017, several experiments had been proposed at the Research Forum that took place in February 2015. However, because of technical difficulties encountered with plasma operations in FY2016, the divertor experiments were not executed. The main contribution from the NSTX Team toward the FES Joint Research Target was therefore based on analysis of NSTX divertor experiments as well as modeling of the NSTX results.

In addition to the NSTX divertor analysis, an experiment was executed on DIII-D by NSTX-U staff within the NSTX-U experimental campaign in June 2017. The experiment "Divertor detachment studies in highly-shaped NSTX/NSTX-U-like plasmas" was aimed at comparison of divertor detachment onset and characteristics between NSTX and DIII-D. Results from this experiment are also included in the report.

<u>NSTX Lower Single Null Divertor Data Analysis</u>

Experiments were executed in NSTX in 2004-2010 to apply the radiative divertor technique to the spherical torus for the first time, and study radiative detachment operating space and its characteristics. NSTX had an open divertor geometry with a horizontal and slightly tilted (15 degrees to horizontal) outer target with graphite PFCs. Divertor experiments in NSTX spanned a range of plasma shaping parameters which can be grouped into weakly-shaped and highly-shaped plasmas. The weakly-shaped plasmas were generally more prone to MHD instabilities and were characteristic of earlier years of NSTX operations. The highly-shaped H-mode plasma scenarios were developed in later years and became a basis for high-performance long pulse H-mode. The relevant experiments are summarized below:

- XP 605, Divertor heat flux reduction and detachment in NBI-heated plasmas
  - Low triangularity $\delta \leq 0.40$ H-mode plasmas with higher strike point major radius R_{OSP} ~ 0.75-0.8 m, low outer strike point flux expansion
- XP 708, Divertor heat flux reduction and detachment in highly shaped plasmas
  - High triangularity $\delta \leq 0.72$ H-mode plasmas with lower strike point major radius ROSP ~ 0.4-0.5 m, high outer strike point flux expansion

- XP 814, Divertor heat flux reduction and detachment in highly-shaped high-performance plasmas
  - Extending studies from XP 708 to high-performance plasmas with plasma currents 1.0 - 1.2 MA and NBI input power PNBI ≤ 6 MW.
- XP 816, Edge characterization in highly shaped plasmas
  - Studies of divertor conditions as a function of X-point height in 4 MW NBI-heated H-mode plasmas
- XP 826, X-point limiter
  - Studies of divertor conditions in a standard divertor configuration with marginal X-point height, nearly limited by the lower X-point
- XP 1045, "Snowflake" divertor configuration in NSTX
  - Studies of a very high flux expansion snowflake-minus divertor configuration
- XP 1050, Radiative divertor with impurity seeding and lithium coatings in NSTX
  - Studies of divertor detachment in a high flux expansion standard and snowflake-minus configurations with lithium coatings and additional deuterated methane CD4 seeding

Data from the above experiments have been analyzed and presented in conferences and peer-review publications. In this report, we summarize several points from NSTX divertor studies to address the Joint Research Target 2017 goals:

- The operating space and characteristics of a partially detached divertor in NSTX
- Dependence of partial detachment characteristics in NSTX on the divertor configuration from experiments and modeling
- Dependence of the radial extent of the partially detached region on divertor SOL width and gas seeding

<u>Detachment Operating Space</u>

Divertor heat flux reduction and detachment in NSTX were studied in the lower single null (LSN) H-mode plasma configurations with weaker shaping (elongation κ=1.8–2.0 and triangularity δ=0.4–0.5), and with stronger shaping (elongation $\kappa \leq 2.3$ and triangularity $\delta \leq 0.7$), as shown in Figure 1 [1-3].

Additional quantities of room-temperature deuterium (D_2) were injected using gas injectors situated at various poloidal locations: at the outboard midplane, inner divertor (ID), and private flux region (PFR) locations for the low-triangularity configurations, and PFR and outer strike

point region (outer SOL) for the high-triangularity configurations, as shown in Figure 15. Both the PFR and the ID injectors were operated at steady-state rates ~10^{22} s^{-1}. Using a different gas delivery hardware setup, the ID injector was also operated in a pulsed mode injecting deuterium from four small plenums through four toroidally symmetric ports in the divertor floor. Each pulse duration was 15-20 ms at an average rate of (0.85 - 3.0) x 10^{22} s^{-1}. For comparison, a typical reference plasma particle inventory was in the range (7-10) x 10^{20}. In dedicated experiments, D_2 was injected to investigate the effectiveness of the radiative and dissipative techniques for divertor heat load reduction, and the impact of additional gas puffing on confinement and plasma performance. A general result of adding deuterium injection was a reduction of the peak outer strike point heat flux by 30-80 %. As the deuterium puffing rate was increased, the outer SOL thermal electron collisionality increased from ν^*_e ~ 5-20, estimated from the Thomson scattering data at the separatrix in reference plasmas, to ν^*_e ~ 30-80. The radiative and dissipative divertor losses increased, and the outer SOL transitioned from a radiative high-recycling divertor regime to a partially detached divertor regime. An operational path to these conditions was different with each gas injector, highlighting the challenge of divertor heat flux reduction in a spherical tokamak open divertor geometry without active pumping. In the configurations with weak shaping, puffing deuterium at the midplane in 3 - 4 MW NBI heated plasmas was the least successful as an H-L back transition and large MHD modes occurred within one τ_E, with simultaneous confinement degradation to 0.6-1.0 of the ITER89P scaling, as shown in Figure 16. However, the radiative and detached divertor operating modes, obtained with the *divertor* gas puffing at moderate and high rates produced good results,

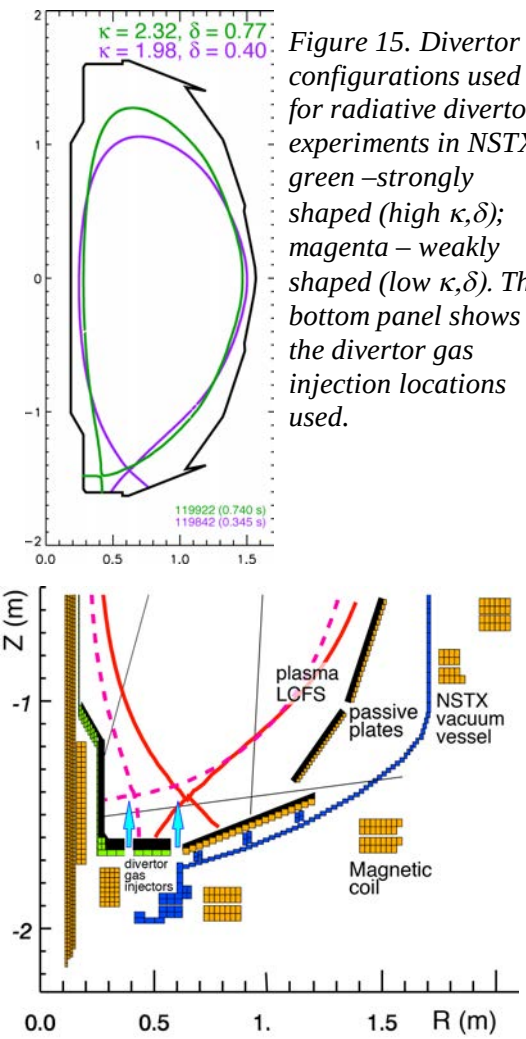

Figure 15. Divertor configurations used for radiative divertor experiments in NSTX: green –strongly shaped (high κ,δ); magenta – weakly shaped (low κ,δ). The bottom panel shows the divertor gas injection locations used.

i.e., divertor heat flux mitigation with insignificant, if any, confinement degradation. In the configurations with strong shaping, similar results were obtained: the best MHD-stable H-mode discharges with a partially detached strike point were obtained only with divertor gas puffing.

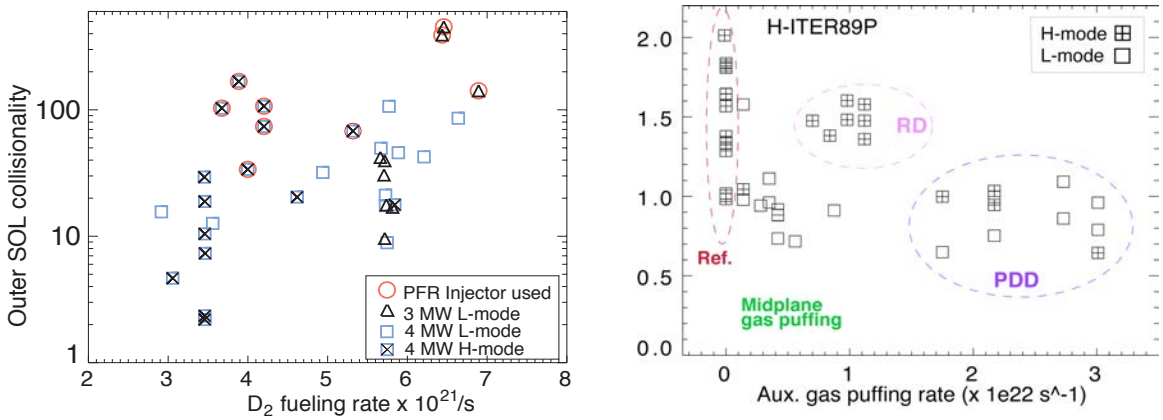

Figure 16. Normalized outer SOL collisionality (left) and the confinement H-ITER89P factor as a function of additional gas puffing in L- and H-mode plasmas in radiative divertor experiments on NSTX.

In the discharges with weak shaping, the inner divertor leg detachment occurred naturally at n_e = 2–3 x 10^{19} m^{-3} and input power $0.8 \leq P_{NBI} \leq 6$ MW. The inner divertor leg region remained in a detached state with $q_{in} \leq 1$ MW/m^2 and T_e~1-2 eV, n_e=(0.7–4) x 10^{20} m^{-3} throughout the operating space (similar to conventional tokamaks). Inner strike point detachment was attributed to a combination of factors: the proximity of the vertical inner wall acting as a source of deuterium neutrals and carbon, a broad heat flux profile with reduced $q_{||}$, and a long connection length [4,5].

The density threshold for the outer strike point partial detachment was found to be high, as the detachment was not observed even at the plasma densities approaching the Greenwald density n_G. In NBI-heated H-mode plasmas the outer strike point peak heat flux q_{pk} demonstrated a linear scaling

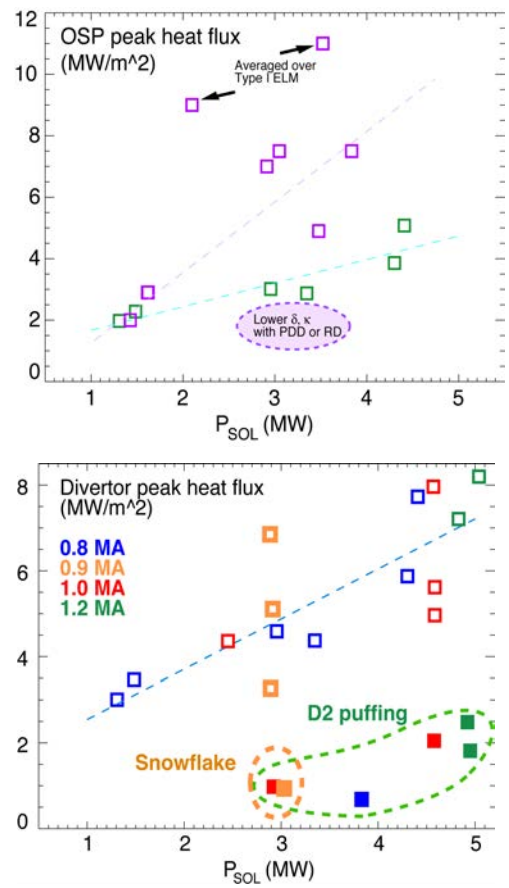

Figure 17. Peak heat flux in NSTX outer strike point as a function of scrape-off layer power for the strongly shaped and weakly shaped configurations (top), and for divertor detachment experiments (bottom).

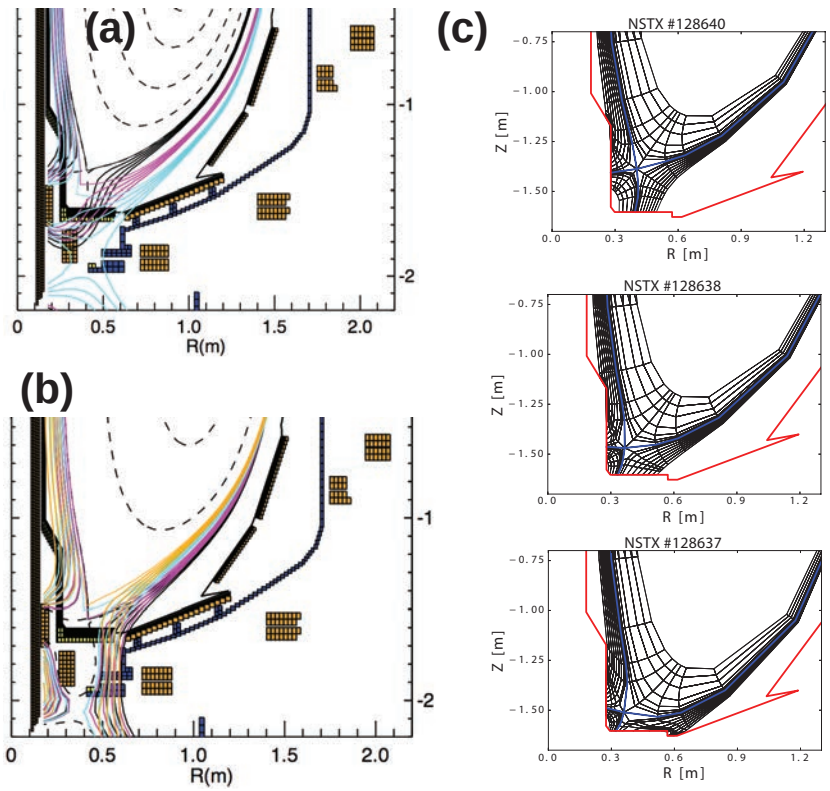

Figure 18. X-point scan experimental equilibria used to study impact of flux expansion and poloidal angle on detachment onset (a) with the same strike point radius (b) with variable strike point radius. In (c), UEDGE grids for modeling experimental results of (a) are shown (top – high X-point, medium – medium X-point height, bottom – low X-point height.

with the SOL power, being in the 2–12 MW/m^2 range for 1–6 MW NBI power, and monotonically increasing with the plasma current I_p commensurate with the change in q_{95} (connection length) and SOL power width λ_q [6, 7].

Radiative divertor experiments were conducted in 4-6 MW NBI-heated H-mode discharges using D_2 injection at rates 5−29 x 10^{21} s^{-1}. In a weakly shaped configuration, a partially detached divertor regime was obtained only at high gas seeding rates 15−29 x 10^{21} s^{-1} that led to an X-point MARFE formation and confinement degradation. The limited access to detachment was found to be qualitatively consistent with predictions of zero-dimensional two point models and two-dimensional multi-fluid modeling using the UEDGE code: sufficiently high steady-state volumetric power and momentum losses required for detachment at high parallel heat flux q≤30–50 MW/m^2 in the open NSTX geometry carbon divertor with a short parallel length and poor gas entrapment was difficult to obtain. In contrast, experiments conducted in 0.8-1.2 MA, 4-6 MW NBI-heated H-mode discharges in a highly-shaped LSN configuration demonstrated reliable access to the partially detached divertor regime. The peak heat flux at the outer strike point (SP) was successfully reduced from 4-10 MW/m^2 to 0.5-2 MW/m^2 using divertor deuterium injection with minimal confinement deterioration, as summarized in Figure 17 [1-3].

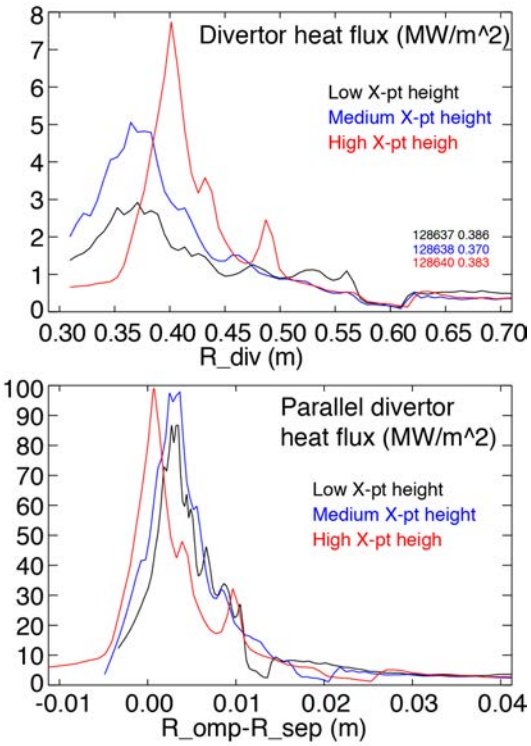

Figure 19. Divertor deposited (top) and parallel (bottom) heat fluxes in the three X-point height highly shaped configurations.

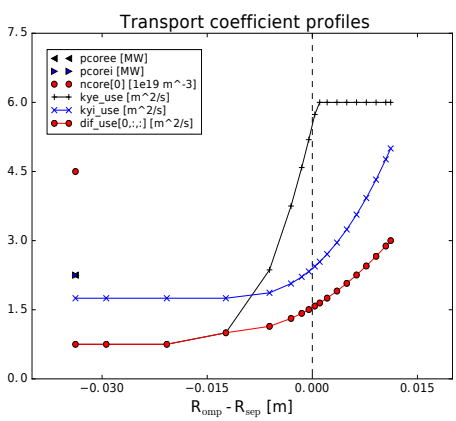

Figure 20. Radial transport coefficient profiles used in the UEDGE model. The boundary conditions for the core-boundary interface are shown: power (pcoree – for electrons, pcorei – for ions) and density (ncore). The transport coefficients are: kye – electron conductivity, kyi – ion conductivity, dif_use – effective particle diffusion.

Role of Divertor Geometry in Detachment Onset

Motivated by the above observations, the role of high flux expansion in detachment threshold was investigated in more detail. A hypothesis was put forward that a higher isothermal divertor volume and higher plasma "plugging efficiency" in the high flux expansion divertor can potentially lead to higher power P_{rad} and momentum p_m losses, thereby facilitating detachment onset. Tokamak studies conducted in open geometry unpumped graphite-tiled divertors most relevant for comparison with NSTX also support these notions. Re-ionization of recycling neutrals in the divertor chamber termed "flux amplification" is an essential feature of the high-recycling divertor regime. As the recycling is increased, the divertor density increases, the divertor temperature further decreases, leading to an increase in the P_{rad} and p_m loss factors, loss of parallel pressure balance, and a transition to detachment. The plasma "plugging efficiency" is defined as a fraction of recycling neutrals re-ionized in the divertor region. In the high flux expansion divertor it is higher because of a larger divertor plasma size in physical space with respect to ionization, charge exchange and elastic collision mean free path lengths, and higher low-temperature plasma volume. Also in this configuration, another critical factor may be the poloidal angle at which magnetic field lines hit the divertor plate. If the angle is less than 90 degrees, recycling neutrals are directed toward the separatrix, and may lead to enhanced recycling and eventually to enhanced volumetric losses ("the vertical target plate"

effect). If the angle is greater than 90 degrees, the neutrals are recycled toward the outer SOL and may contribute less to ionization within the divertor. An experiment was carried out on NSTX whereby the divertor magnetic configuration geometry was systematically changed by either (i) changing the distance between the lower divertor X-point and the divertor plate (X-point height), or by (ii) keeping the X-point height constant and increasing the outer SP radius. Shown in Figure 4 are the experimental equilibria and numerical grids used for modeling divertor transport and radiation in these configurations. The experiment was carried out in a LSN configuration, in 1 MA, 6 MW NBI-heated H-mode plasma discharges, fueled by deuterium from a high field side gas injector. For the divertor plasma analysis, infrared thermography, spectrally filtered cameras, divertor bolometers, a multi-channel UV-visible spectrometer, and Penning and micro-ion neutral pressure gauges were used. Experimental divertor data analysis was previously presented [8] and is summarized below. Additional analysis included modeling of divertor transport and radiation with the multi-fluid code UEDGE and is also summarized below.

Divertor heat flux profiles measured in the three X-point height configurations are shown in Figure 19. The parallel divertor heat flux was slightly lower in the highest flux expansion configuration. While the divertor poloidal magnetic flux expansion factor appeared to play the dominant role in peak divertor heat flux reduction from 7-8 MW/m^2 to 1-2 MW/m^2, the higher flux expansion configurations also showed higher impurity emission and a higher deuterium high-*n* line emissions indicative of higher recombination rates [8]. These experimental observations suggested that the lower X-point height configuration facilitated detachment of the outer strike point region.

In order to understand the experimental results, UEDGE code modeling of each configuration was performed. The goal of the simulations was to evaluate how each configuration approaches detachment with increasing upstream density. The model included the core-boundary power of 4.6 MW equally divided between electrons and ions. It was assumed that radial heat and particle transport (including impurities) was not modified by the divertor configurations: the same radially varying transport coefficients were used for all three configurations. The radial transport coefficient profiles are shown in Figure 20. The divertor plate recycling was 0.999, the wall recycling coefficient was 0.90, both the physical and chemical sputtering was used on all boundary surfaces. The carbon impurity (Z=6) was included,

with cross-field particle diffusivity for all charge states set at 0.5 m^2/s. First, the medium X-point height configuration (128638) was simulated in order to find the boundary conditions and radial transport coefficients that would produce a model with upstream and divertor conditions similar to the experimental ones. These conditions included upstream radial n_e, T_e and T_i profiles, outer midplane separatrix n_e, T_e values, divertor heat flux profiles $q_{perp}(R)$, parallel divertor heat flux profiles remapped to the outer midplane, and the SOL power width. The transport and boundary model was then applied with minimal modifications to the other two divertor geometry configurations.

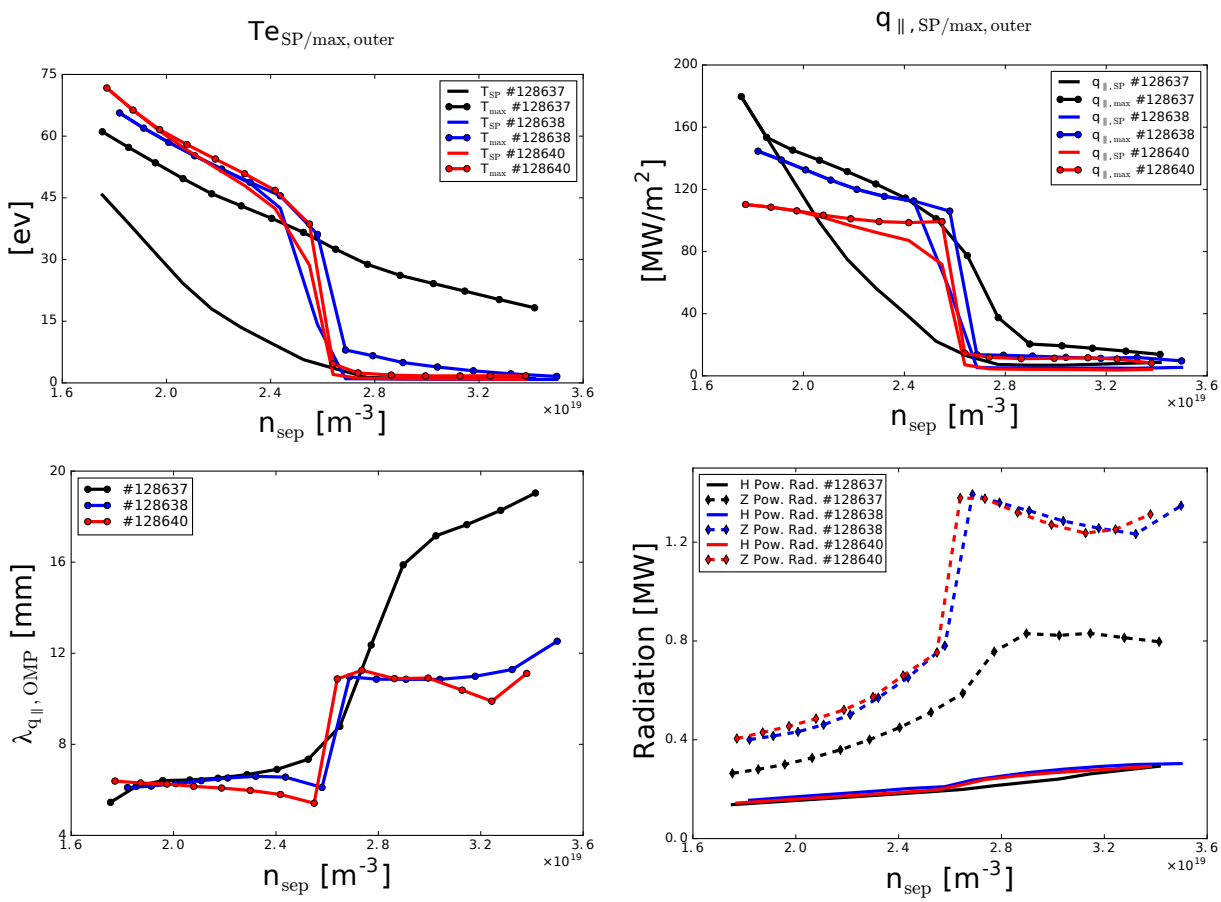

Figure 21. Density scans of divertor T_e, divertor parallel heat flux, divertor power width, and divertor radiation as functions of n_{sep} in UEDGE models.

The modeling results can be summarized as follows (Fig. 21): using an upstream density scan that started at a low density n_{sep}=1.7 x 10^{19} m^{-3} and ended at a high density n_{sep}=3.5 x 10^{19} m^{-3}, it was demonstrated that all three configurations transition from the sheath-limited high divertor temperature regime to the high-recycling regime and then to the partial outer strike point detachment. However, the dynamics of the approach to detachment was different. In the medium and the high X-point height configurations as the upstream density increased, divertor temperature and heat flux decreased and radiated power slowly increased. At some threshold n_{sep} value a transition to an outer strike point detachment occurred: divertor plasma parameters changed abruptly and significantly (this colloquially referred to as a "cliff"-like behavior). The low X-point height configuration, on the contrary, demonstrated a slow approach to the low divertor T_e, q_{perp} values. This is quite consistent with the experiment where this configuration showed lower parallel heat flux and increased impurity and Balmer emissions.

<u>The SOL Power Width and the Radial Extent of the Partially Detached (Dissipative) Region</u>

As demonstrated by the DOE Joint Research Target 2010 activities and related experiments and modeling, the SOL power width in NSTX and other tokamaks inversely scales with plasma current (or more specifically, the outer midplane poloidal field). On-going experiments, modeling and theory attempt to connect this scaling to (neo)classical drifts, turbulent transport, or edge MHD activity. In NSTX, divertor detachment experiments were conducted in 0.8-1.2 MA discharges in the same high flux expansion divertor configuration in 4-6 MW H-mode discharges with varying divertor gas puffing. Our recent analysis attempted to connect divertor detachment characteristics to the SOL width and transport using the NSTX

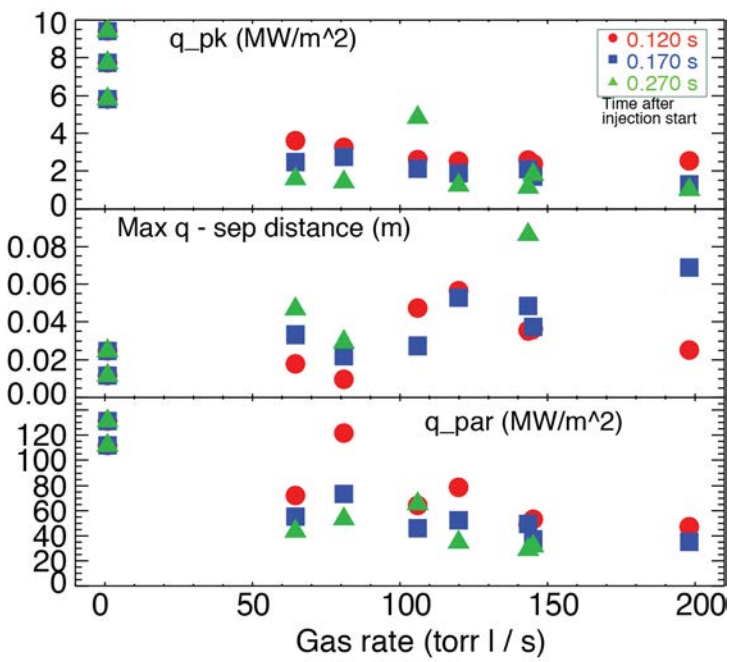

Figure 22. Divertor peak heat flux, distance between separatrix and peak heat flux (approximating the radial extent of dissipative losses), and parallel peak heat flux, as a function of deuterium injection rate for a 1.0 MA H-mode NSTX discharge

experimental database with I_p=0.8, 0.9, 1.0, and 1.2 MA.

A partial detachment of the outer trike point has been obtained at several deuterium injection rates for 0.8, 1.0 and 1.2 MA H-mode discharges. The divertor deuterium injector was used. An example of data analysis for 1.0 MA discharges is shown in Figure 22, peak divertor heat fluxes,

I_p (MA)	λ_q (mm)	$L_{\parallel}$ (m)	q_{peak} (MW/m^2)	$q_{\parallel}$ (MW/m^2)	Δ_{diss} (mm)
0.8	13	4.0	4-6	100	20-80
1.0	9	4.0-4.5	5-7	100-150	20-80
1.2	7	2.3-4.0	7-10	100-200	20-80

Table 1. Summary of NSTX LSN high-triangularity divertor parameters.

distance of peak divertor heat flux from separatrix, and peak parallel heat fluxes as functions of gas injection rate are shown for three times since the start of the gas injection. General trends can be seen with increasing gas injection: with higher rates, both parallel and deposited peak heat fluxes are reduced, and the partial detachment (dissipative loss) radial extent (approximated by the distance between the divertor heat flux peak and the separatrix) increased. The same trend is generally observed for each gas injection rate with continuing injection, as shown by three time points of different color, as the injected gas remained in the divertor due to the lack of cryo-pumping. Some discharges were disrupted by continuing gas injection which explains some missing points (e.g., the green points corresponding to later times). A similar trend is observed for 0.8, 1.0, and 1.2 MA, for which SOL power widths vary in the range λ_q= 4-8 mm [6,7]. With 6 MW NBI heating, 4-5 MW of power flows into the SOL. The λ_q scales inversely with plasma current: $\lambda_q = 0.91\ I_p^{-1.6}$ [7] and the parallel length is proportional to I_p. The relevant NSTX data is summarized in Table 1. The hypothesis was that the radial extent of the partially detached (or dissipative loss) region can be connected to the SOL power width λ_q using the characteristic dissipative connection length predicted by a one-dimensional radiative detachment model [3]. However, the scatter in the NSTX database precluded any clear trends in the data. A dedicated experiment with well-controlled divertor configuration parameters, such as steady-state strike and X-point positions, must be carried out in NSTX-U to test the hypothesis.

Results from the DIII-D Experiment MP2017-08-02 "Divertor Detachment Studies in Highly-Shaped NSTX/NSTX-U-like Plasmas

To compare divertor detachment operating space in NSTX and DIII-D, a dedicated experiment was developed and run at DIII-D in June 2017. An NSTX-like high-triangularity double null shape with strong bias toward the lower divertor (and ion grad B drift toward the lower divertor), and with high divertor poloidal flux expansion, was developed as shown in Figure 23. An H-mode 1 MA plasma scenario with 5 MW NBI was used to study how divertor detachment characteristics depend on the poloidal gas injection location. Three gas injectors were used, as shown in the Figure 23, one midplane injector, one far-SOL injector, and one divertor injector in the visinity of the outer strike point.

Denisty control in the discharges with gas puffing proved to be difficult as the lower cryo-pump was not used in this experiment. The experiment aimed at using the H-mode with basic lower density and additional gas injection rate ramps from 0 to 150 Tor l/s. It was expected that at

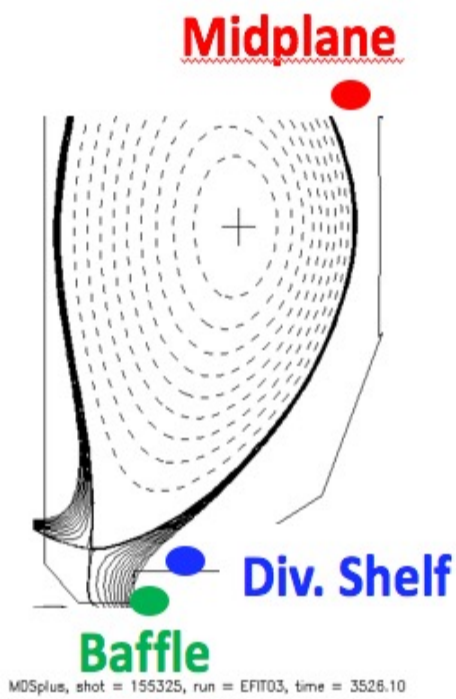

Figure 23. A schematic of the NSTX-like shape and gas injector locations that were used to study detachment similarities.

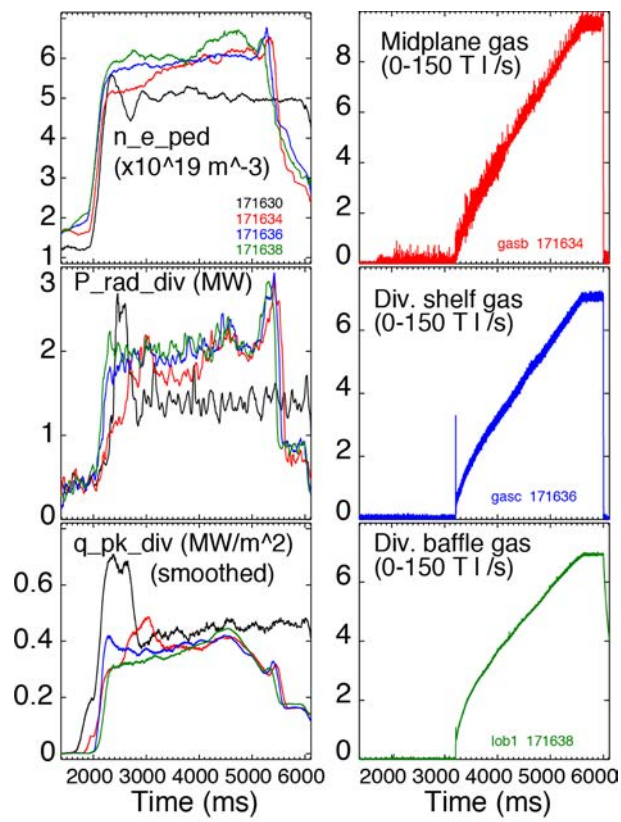

Figure 24. Time traces of pedestal density, lower divertor radiated power, divertor peak heat flux, and the three gas valves used.

some point in the ramp, the increasing density would reach the detachment onset threshold. The results showed that, generally, access to the lower outer strike point detachment had little dependence on the poloidal gas seeding location. This is summarized in Figure 24, where time traces of four discharges are compared: one reference lower density H-mode without additional gas puffing, and three H-modes with gas puffing rate ramps from different locations. There are slightly different sensitivities of pedestal densities with additional gas puffing, however, generally, the outer strike point detachment onset occurs at about the same time (4500 ms). The heat flux profiles from IRTV, divertor Balmer emission, divertor C III and D_α profiles and Langmuir probes inicated that a partial detachment was induced with each of the three injectors at about the same time. These results suggest that access to partial detachment at DIII-D is qualitatively closer to the two-point divertor model description than in NSTX: gas injection at any location increases the SOL density and which leads to a faster divertor density rise and a transition to the detachment. In NSTX, H-mode plasmas are much more sensitive to the gas puffing location, and there is a weaker dependence of n_{sep} on the core/pedestal density and gas puffing.

NSTX Double-Null Divertor Analysis

NSTX-U is expected to produce significant unmitigated divertor heat fluxes with a narrow SOL power width, λ_q at its designed operating parameters [11] of I_p = 2 MA and P_{NBI} = 10 MW with discharges lasting up to 5 seconds. Because of this, double-null discharge scenarios in combination with other heat flux mitigation techniques (X-Divertor, Snowflake Divertor and divertor impurity injection) will be needed to maintain divertor heat fluxes below the thermal and mechanical design limits of the plasma facing components (PFCs).

Many studies of double-null discharges were carried out on NSTX. In one such study [12] it was found that the ELM regime of the discharge changed with δ_r^{sep}, which is defined as the distance at the outer midplane between the separatrix flux surfaces passing through the upper and lower X-points, with the convention that a negative δ_r^{sep} favors the lower divertor. Because of the changing ELM regimes, measurements of the divertor heat flux must be > 1 kHz to differentiate the inter-ELM from the ELM heat fluxes. The work presented in this report is focused on a set of discharges obtained during the 2010 run campaign of NSTX with the use of a fast [13], dual-band [14] infrared camera to be able to resolve the ELM and inter-ELM divertor heat fluxes,

while δ_r^{sep} was systematically varied.

The discharges had I_p = 0.9 MA, δ_{bot} ~ 0.8 with P_{NBI} = 4 MW and utilized ~ 100 mg of lithium evaporation prior to each discharge. However, close to double-null, there was significant variation in both of δ_r^{sep} and δ_{bot}. Figure 25a shows the peak heat flux on the lower divertor at the outer strike point measured using the dual-band IR camera system to account for emissivity changes due to the use of evaporative lithium coatings. The power passing through the last closed flux surface into the SOL, P_{SOL} which is defined as $P_{SOL} = P_{NBI} + P_{oh} - \frac{dW}{dt} - P_{rad}^{core}$ is shown in Figure 11b. P_{NBI} is the injected neutral beam power. P_{oh} is the ohmic power. dW/dt is the time rate of change of the plasma energy and P_{rad}^{core} is the power radiated from the core plasma. Figure 11c and 11d show the value of δ_r^{sep} derived from an EFIT02 magnetic equilibrium reconstruction and the lower divertor D_α respectively. Infrared coverage in NSTX was only available for the lower, outer strike point (LOSP) preventing a full accounting of the heat fluxes at each strike point. From Figure 11a, it is clear that the inter-ELM divertor heat flux at the LOSP is reduced as δ_r^{sep} approaches double-null.

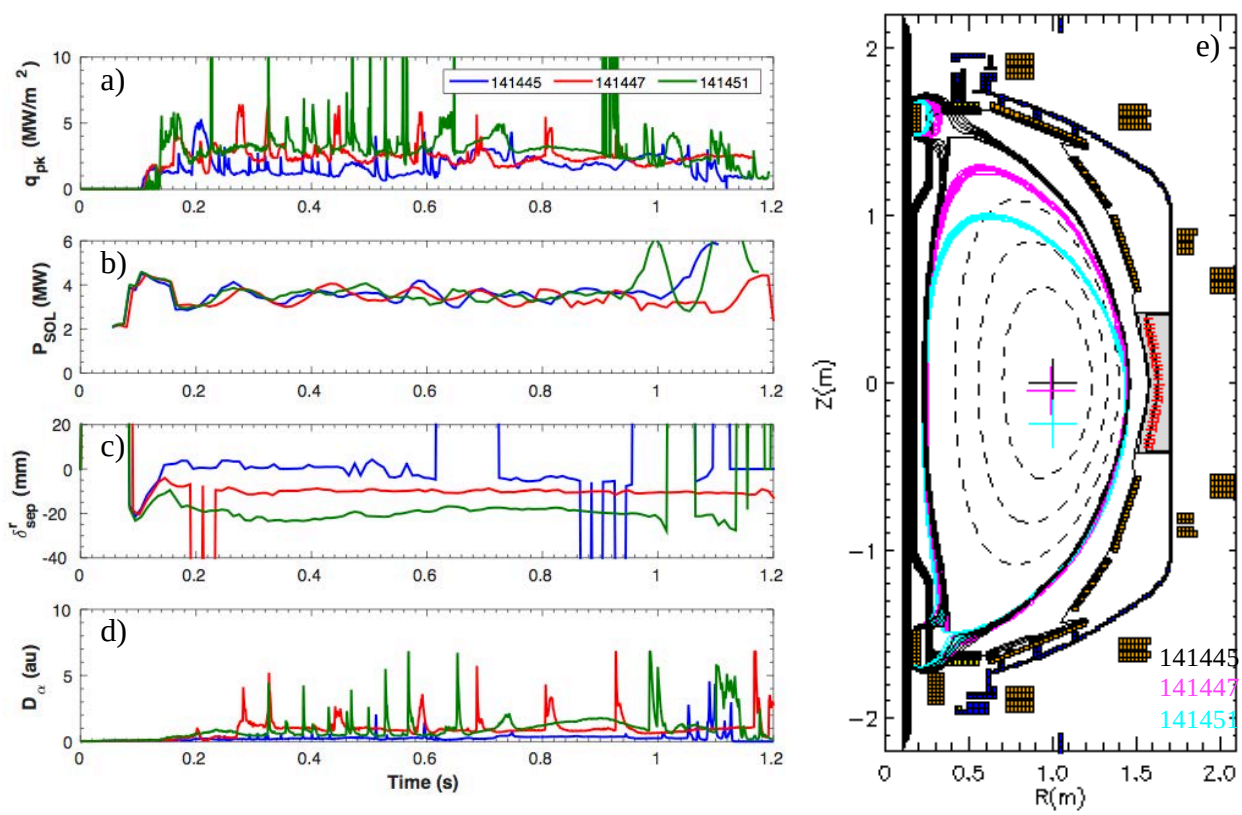

Figure 25. NSTX data showing the variation in a) peak heat flux on the lower divertor at the outer strike point; b) P_{SOL}; c) δ_r^{sep}, d) D_a in the lower divertor and e) Poloidal cross-section (t = 0.355 sec) for shots 141451 (δ_r^{sep} = -20 mm), 141447 (δ_r^{sep} = -10 mm), and 141445 (δ_r^{sep} ~ 0 mm).

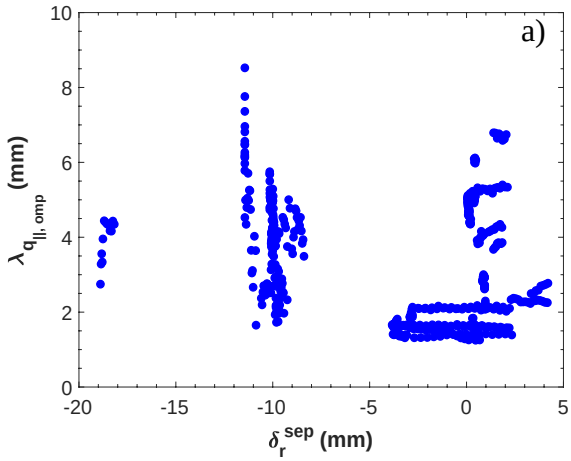

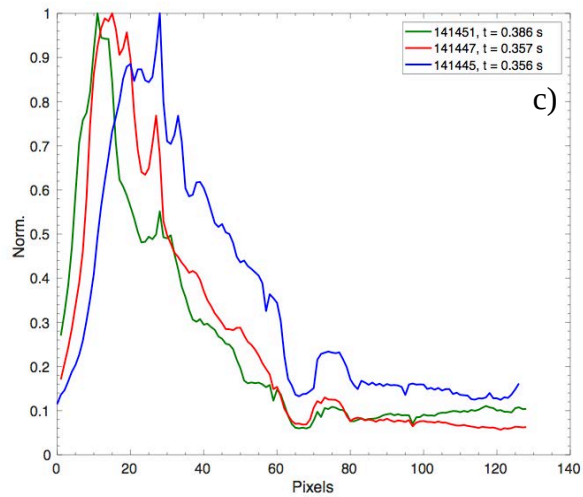

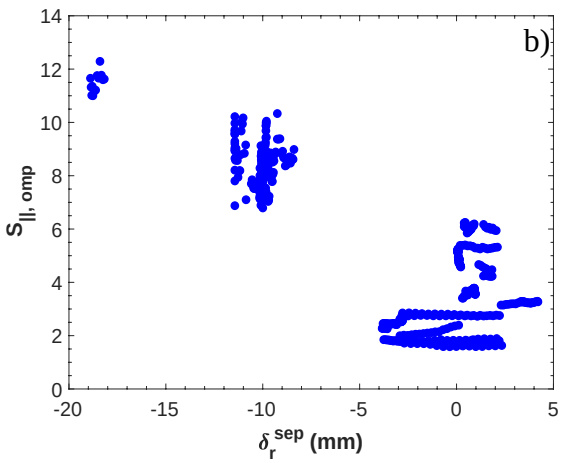

Figure 26. a) λ_q and b) S obtained from fitting the radial parallel, heat flux profiles mapped to the outer midplane (omp) to the Eich formulation as a function of δ_r^{sep}; c) Radial Deposited heat flux profiles (normalized) for δ_r^{sep} = -20 mm (141451), for δ_r^{sep} = -10 mm (141447) and for δ_r^{sep} = 0 mm (141445).

The δ_r^{sep} scan also resulted in changes to the discharge shape, namely elongation κ. These variations are shown in cross-section of the poloidal magnetic field contours in Figure 25e. The changes in κ do result in a change to the poloidal magnetic field at the outer midplane seperatrix, $B_{pol,\ omp}$ which also affects λ_q. However, the data presented here is limited to t ≤ 0.6 sec and $B_{pol,\ omp}$ is found to vary ~ 5% between the shots analyzed over that time period and will be neglected for the remainder of this analysis.

Preliminary analysis shows that the deposited heat flux profiles, shown in Figure 16c, broaden as δ_r^{sep} approaches 0 mm. However, it's unclear if this is due only to the change in δ_r^{sep} or to other parameters changing such as triangularity or flux expansion in the SOL. This is resolved by calculating the parallel heat flux and mapping it to the outer midplane (OMP). Shown in Figure 12a and b are the "Eich" Diffusive-Gaussian fits [15] of parallel heat flux data measured at the LOSP and mapped to the OMP of a) λ_q and b) S. The diffusive-gaussian fits were performed only on measurements from the LWIR band (6.5 – 10 μm). Because of the

reduced divertor heat flux at DN, the signal in the individual IR bands is also reduced making the image registration process difficult and distorting the radial profile. The same procedure was used for the discharges in LSN for consistency in fitting all the IR profiles. However, the magnitude of the divertor heat fluxes are taken from the dual-band measurements.

From Figure 16a, little change in $\lambda_{q||, OMP}$ is observed as a function of δ_r^{sep}. Meanwhile, $S_{||, OMP}$ is found to be systemically higher in LSN compared to DN discharges shown in Figure 26b. This is qualitatively consistent with measurements made for MAST inter-ELM H-mode discharges of λ_q and S [16]. Future work on both MAST-U and NSTX-U will focus on understanding the differences in SOL transport between LSN and DN discharges and projecting to larger more powerful STs.

Total power accounting in DN discharges in NSTX is complicated since there was no IR coverage of the inner strike points and the upper divertor in general. Figure 27 shows the power deposited at the LOSP, as measured by the dual-band IR camera, normalized to P_{SOL} versus the ratio of $\delta_r^{sep}/\lambda_{q||, OMP}$. While P_{SOL} is shown to be constant between the discharges in Figure 25b, this normalization is done to account for changes in P_{rad}^{core} during the shot, which has been shown to vary as discharge time progresses due to accumulation of carbon impurities in ELM-free NSTX discharges [17]. The ratio of $\delta_r^{sep}/\lambda_{q||, OMP}$ is used as a dimensionless ordering parameter. From Figure 27, power to the LOSP is minimized for $\delta_r^{sep}/\lambda_{q||, OMP} \pm 2$. In this range, only 10 – 25% of P_{SOL} reaches the LOSP.

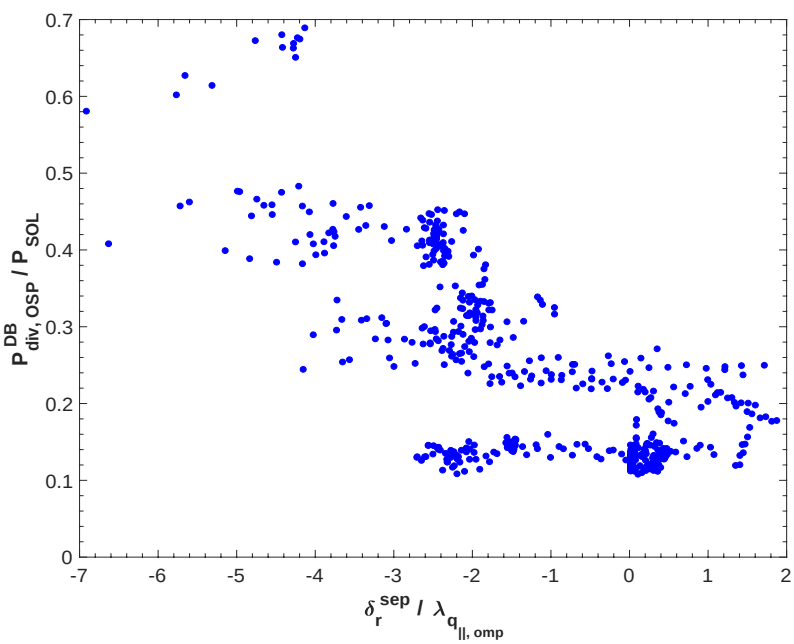

Figure 27. Ratio of deposited power at the lower, outer strike point to P_{SOL} as a function of $\delta_r^{sep} / \lambda q_{||, omp}$.

FES Joint Facilities Milestone 2017

Alcator C-Mod Archived-Data Analysis

Research Topics

During FY15 and FY16 run campaigns, Alcator C-Mod performed dedicated experiments to directly address 2017 JRT goals: "… *assess the impact of edge magnetic configurations and divertor geometries on dissipative regimes, as well as their effect on the width of the power exhaust channel, thus providing essential data to test and validate leading boundary plasma models.*"

This research was organized primarily under four mini-proposals:

- MP#744 – "SOL heat-flux widths in I-mode plasmas"
  http://www-internal.psfc.mit.edu/research/alcator/miniproposals/744.pdf
- MP#751 – "Investigating the physics of the heat flux channel width in L and H-modes"
  http://www-internal.psfc.mit.edu/research/alcator/miniproposals/751.pdf
- MP#789 – "Feedback control of radiative divertor experiments: feedback on divertor heat flux"
  http://www-internal.psfc.mit.edu/research/alcator/miniproposals/789.pdf
- MP#806 – "Assessment of divertor conditions in double-null"
  http://www-internal.psfc.mit.edu/research/alcator/miniproposals/806.pdf

The experiments took advantage of significant diagnostic improvements including: a refurbished surface thermocouple array in the outer divertor, a new 'rail-probe' Langmuir probe array in the outer divertor, a servomotor-driven fast-scanning Mirror Langmuir Probe, IR camera views of the inner divertor strike point region and a real-time feedback system to control via nitrogen seeding the level of divertor dissipation and heat fluxes arriving at the divertor target. Prior to the FY16 campaign, improvements were made to the poloidal field coil power supplies, allowing more precise control of the upper and lower x-point locations with reduced jitter. During the FY16 campaign, Alcator C-Mod operated at high toroidal magnetic fields (5.4 - 8T) and with poloidal magnetic fields exceeding 1 tesla, allowing explorations of divertor heat flux widths in this unprecedented parameter range for EDA H-mode and I-mode plasmas.

Alcator C-Mod devoted considerable resources in the FY15 and FY16 campaigns to studying I-modes, both from core confinement and boundary plasma perspectives. I-mode plasmas have many attractive features worth pursuing as a vehicle to achieve a burning plasma – particularly at high magnetic fields – and the Alcator Team has led the world effort to investigate them. The exhaust power handling of an I-mode plasma may be challenging however. Detached divertor operation with an I-mode plasma was attempted, but not achieved. Furthermore, initial results indicated that the sharing of power exhaust on the inner versus outer divertor in single null configurations may not be so favorable as it is in H-modes.

Based on the excellent quality of these new data and the potential for high impact in a number of areas, it was decided that the *Alcator C-Mod archived-data analysis* should target four topics in support of the 2017 JRT:

(1) Document divertor heat flux profiles and widths at the outer strike point in EDA H-mode and I-mode plasmas at high poloidal magnetic field

Goal: Extend the international database on heat flux widths into this extended parameter range, providing essential guidance and validation for first-principles models (e.g., XGC1, BOUT++).

(2) Investigate inner divertor strike point in I-mode plasmas

Goal: Examine and document heat flux profiles and width scaling for I-modes plasmas, which typically have enhanced heat fluxes at the inner strike location – an important consideration for application in ITER or a reactor.

(3) Explore divertor conditions in near-double null configurations

Goal: Document heat flux widths and heat flux sharing on all divertor target surfaces (inner/outer and upper/lower) as a function of magnetic flux balance in L-mode, H-mode and I-mode. Fusion reactors will likely operate in double-null to spread heat exhaust on the largest surface area possible and/or minimize heat to the inner divertor strike point locations. The overall distribution of power at high poloidal magnetic field where the heat

(4) Explore influence of divertor heat flux dissipation on SOL profiles

Goal: Examine and document the influence of feedback-controlled divertor nitrogen seeding on SOL profiles – both the near SOL heat flux width and the far SOL shoulder. Theory indicates that divertor target 'boundary conditions' can influence SOL turbulence and transport and thus the profiles – in particular, whether or not the turbulence is 'disconnected' along field lines into the divertor.

Initial Highlights From Ongoing JRT Data Analysis

The research has proven to be quite fruitful, yielding new, high impact results. Although data analysis is presently ongoing, some highlights include:

- The "Eich" empirical scaling of the heat flux channel width has been tested to ITER-level poloidal magnetic fields (1.25 tesla). The *minimum* heat flux channel widths in both EDA H-modes and I-modes continue to follow Eich scaling in this parameter range, but there is significant scatter in the widths. Database analysis suggests that there are "hidden variables" associated with this scatter, likely correlated with the quality of plasma confinement, such as pedestal gradients and core plasma pressures. This finding is consistent with the 2010 JRT work, which noted a correlation between heat flux widths and plasma stored energy of EDA H-modes [18].
- Minimum widths of heat flux footprints at the inner divertor in single-null I-mode discharges are narrow, ~1 to ~1.5 times the minimum outer divertor heat flux target widths when mapped to the outer mid-plane. Thus, I-mode operation with a single-null magnetic configuration could present a challenge to the inner divertor power handling in reactor scenarios.
- In balanced double-null configurations, it is found that power to the inner divertors in L-mode is less than ~10% of the total plasma exhaust. For H-modes, this fraction increases to ~20%. I-modes have been successfully attained in near double-null configurations with substantial reduction in power to the inner divertor, dropping to factions as low as 10% of the total exhaust. An extensive study of L-mode plasmas at three different plasma currents finds that power sharing among inner-outer and upper-lower divertors can be modeled in terms of logistic functions of magnetic flux surface location, mapped to the outer mid-plane (δR_{sep}) and scaled by a characteristic heat flux width (λ) with different heat flux widths for the inner and outer divertors. A Gaussian-like function of $\delta R_{sep}/\lambda$ is found to describe in-out divertor power sharing.
- Outer mid-plane electron temperature profiles near the last-closed flux surface are found to be insensitive to the level of nitrogen seeding in the divertor. The upstream electron temperature e-folding widths are found to remain similar despite an order of magnitude reduction in heat fluxes arriving at the outer divertor strike point and an order of magnitude reduction in net current densities arriving at the outer divertor, which indicates electrical disconnection. Electron temperature and density e-folding widths only show weak trends, if any, with increasing levels of divertor dissipation: decrease slightly (1.1 MA), increase slightly (0.8 MA) or show no trend within the scatter of the data (0.55 MA dataset). These data suggest that the physical mechanisms that determine the electron temperature gradients

near the separatrix – which largely sets the power folding heat flux widths – do not involve plasma conditions at the divertor target plate. Profiles in the far scrape-off layer in 1.1 MA cases are found to be strongly affected by nitrogen seeding, showing reductions in both density and electron temperature. On the other hand, profiles in the far scrape-off layer for 0.8 and 0.55 MA datasets are unaffected by nitrogen seeding. At this time, there is no direct indication as to why the profiles in the far SOL respond differently to nitrogen seeding in these datasets.

(1) Document divertor heat flux profiles and widths near the outer strike point in EDA H-mode and I-mode plasmas at high poloidal magnetic field

Goal: Extend the international database on heat flux widths into this extended parameter range, providing essential guidance and validation for first-principles models (e.g., XGC1, BOUT++).

The international multi-machine divertor heat flux width database [19] was assembled to empirically assess the heat flux width scaling towards reactor class tokamaks. The primary conclusion of this study was: "*the result is that practically only the poloidal magnetic field is identified to be statistically important*". The heat flux width for attached H-mode plasmas was found to scale inversely with poloidal magnetic field (B_p) and to be independent of machine size. Yet the original database only extended to B_p=0.8 T whereas the ITER 15 MA scenario will have B_p=1.2 T. Among divertor tokamaks, only Alcator C-Mod could operate with B_p at or above ITER (JET running at 4.5 MA would have B_p=0.9 T).

Comparison With Previous Measurements

A focus of the C-Mod FY16 experimental campaign was to measure heat flux widths over a wide range of plasma conditions, especially at ITER-level B_p, taking advantage of C-Mod's outer divertor surface thermocouple array. Here we examine measurements at B_p > 0.9 T. Figure 28 shows the previous heat flux width data with the horizontal axis extended to include the new C-Mod data. The new high-field data is consistent with the inverse poloidal field scaling, extending along the trend line. Although there is a moderate amount of scatter in the data (up to ~+/-50 %), the relative scatter is consistent in magnitude with the rest of the database. We are presently searching for additional variables in the experiment that might explain the scatter.

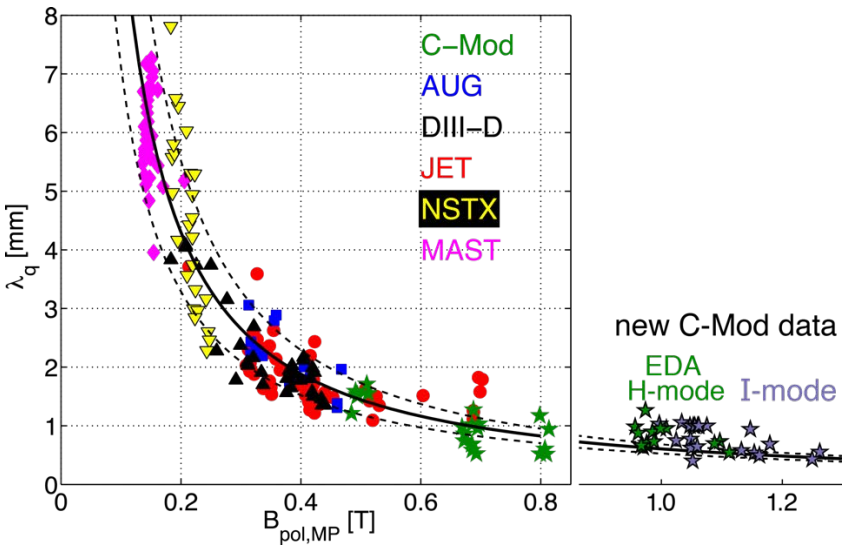

Figure 28. The 'Eich' heat flux width database, showing an inverse scaling of the heat flux width with poloidal magnetic field [19], extended to include the new C-Mod data at high poloidal field. Previous data points were all in H-mode, either EDA H-mode (C-Mod) or between ELMs (all others). New C-Mod data includes both EDA H-mode and I-mode. An ITER 15 MA scenario would operate at 1.2 T.

Both EDA H-mode and I-modes are included in the new high-field data. The multi-machine database only included H-modes, either EDA H-mode (C-Mod) or between ELMs (all others). The I-mode data extends to higher poloidal field than EDA H-modes. This is because C-Mod did not have enough external power to produce H-modes at the highest fields, while it did have sufficient power to attain I-modes. Both the I- and H-modes had essentially the same heat flux width at the same poloidal field.

Comparison With Theoretical Models

The heuristic drift (HD) model [20] does a relatively good job of reproducing the major scaling of the heat flux database, Figure 29. The HD model balances cross-field drifts into the boundary with near-sonic transport parallel to the field. The HD scaling with engineering parameters is: $\lambda_{\mathrm{q}} \propto P_{\mathrm{SOL}}^{0.13} a^{2.1} B^{0.25} I_{\mathrm{P}}^{-1.1} R^{-1.0}$. The new high field C-Mod heat flux widths follow the same trend as those at low/moderate field: the wider widths overlay the HD prediction whereas the narrower widths continue to be over-predicted by the HD model.

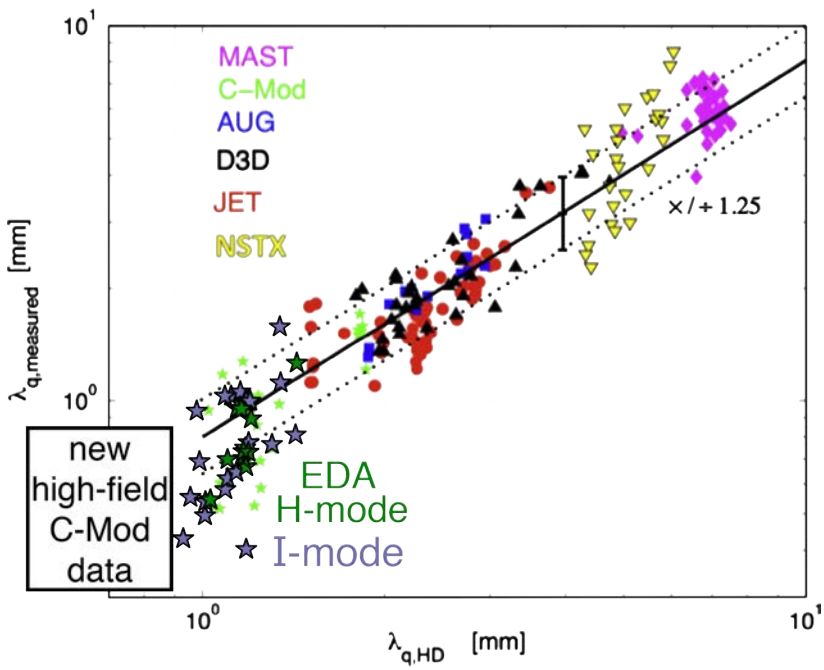

Figure 29. Comparison of the measured heat flux widths from the Eich database and that predicted by the heuristic drift model [20]. The new C-Mod data points at high poloidal field are over plotted on the original figure. They largely follow the trend of previous C-Mod data points: close to the heuristic drift model at the wider widths and lower than the model at narrower widths.

The edge gyrokinetic code XGC1 has been used to simulate discharges in the heat flux width database [21]. It has reproduced the empirical trend of heat flux width scaling inversely with poloidal magnetic field quite well, matching discharges on C-Mod, DIII-D, JET, and NSTX over a wide range of parameters. However, it predicts a heat flux width for ITER ~10 times larger than the database scaling would suggest. Apparently, this is due to a transition (in the code) from ion neoclassical transport dominating the heat flux width to blobby, turbulent transport. It would be helpful if a theoretical model could be developed that would delineate this transition in detail. Existing experiments might be able to access the scrape-off layer parameters needed to test it.

Full Database Trends

This new heat flux database contains nearly 300 shots with approximately equal numbers of L-, I-, and H-modes. Data span nearly the entire operating range of C-Mod: 2.7 T < B_T < 8.0 T, 0.55 MA < I_p < 1.7 MA, 0.4 T < B_p < 1.3 T, 0.08 < n/n_G < 0.7, 0.4x10^{20} m^{-3} < $\bar{n}_e$< 4.8x10^{20} m^{-3}, 0.5 MW < P_{in} < 5.0 MW.

The heat flux width versus poloidal magnetic field is plotted in Figure 30. The H-mode data follows the now-standard Eich inverse poloidal field scaling. The I- and L-mode data are less clear. There are many points well above the H-mode scaling for a given poloidal field. Searching through the database we've found another global parameter that better organizes the data: the volume-average plasma pressure. Using that quantity, all of the L-, I-, and H-mode points overlay, within their relative scatter. This is an important observation, suggesting that the physics that controls the quality of the core plasma confinement also affects the boundary heat flux width.

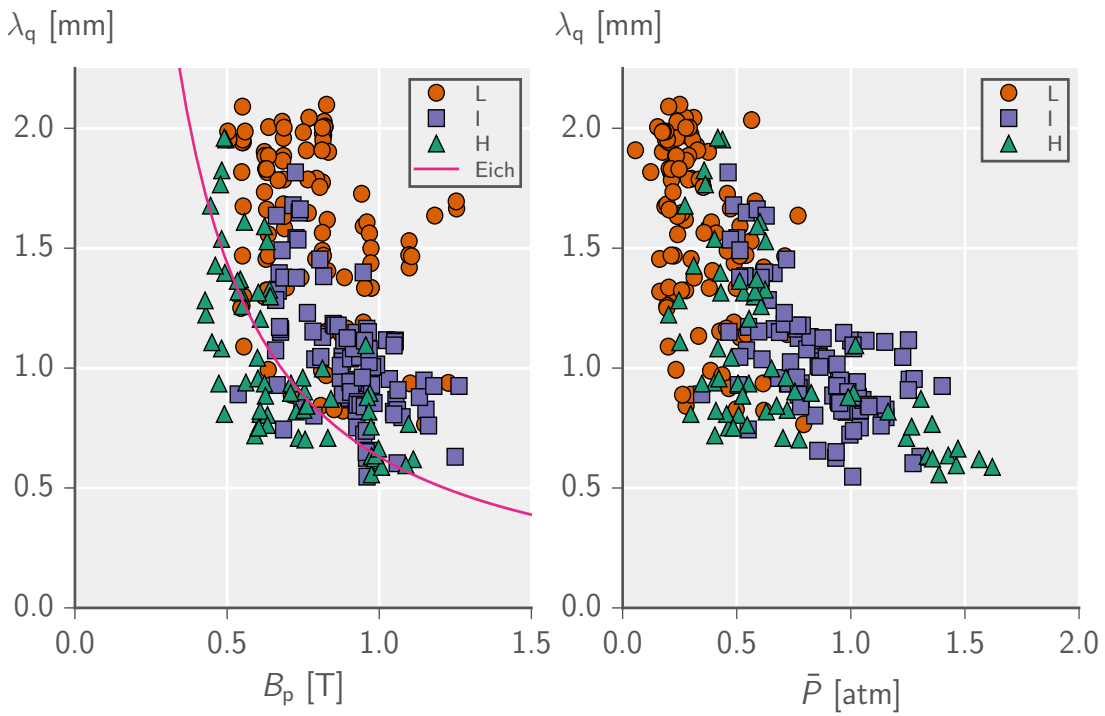

Figure 31. Heat flux width versus poloidal magnetic field (left) and volume-averaged plasma pressure (right) for all three confinement regimes. Eich inverse poloidal field scaling is indicated on the left as a solid red line. Searching for correlations with global parameters across confinement regimes, it is found that the heat flux width organizes better around the volume-averaged pressure than the poloidal magnetic field, possibly indicating a shared dependency on physics determining core confinement and edge heat flux width.

There were also Thomson scattering measurements of edge electron temperature and density profiles available for much of this database. The values of the maximum edge electron temperature, density, and pressure gradients were computed and inserted into the database. Figure 31 shows divertor heat flux width, poloidal magnetic field, and volume-averaged plasma pressure plotted with respect to these quantities. Not surprisingly, both the edge electron temperature and pressure gradients organize the divertor heat flux width data about as well as volume-averaged plasma pressure.

These results continue the sobering story of the divertor heat flux width. Core plasma pressure is intrinsically linked to the purpose of a tokamak: producing power from fusion ($P_{\mathrm{fusion}} \propto p_{\mathrm{plasma}}^2$). Finding that the divertor heat flux width scales inversely with the core plasma pressure across L-, I-, and H-modes indicates that narrow boundary heat flux widths may be an inescapable part of playing the fusion game.

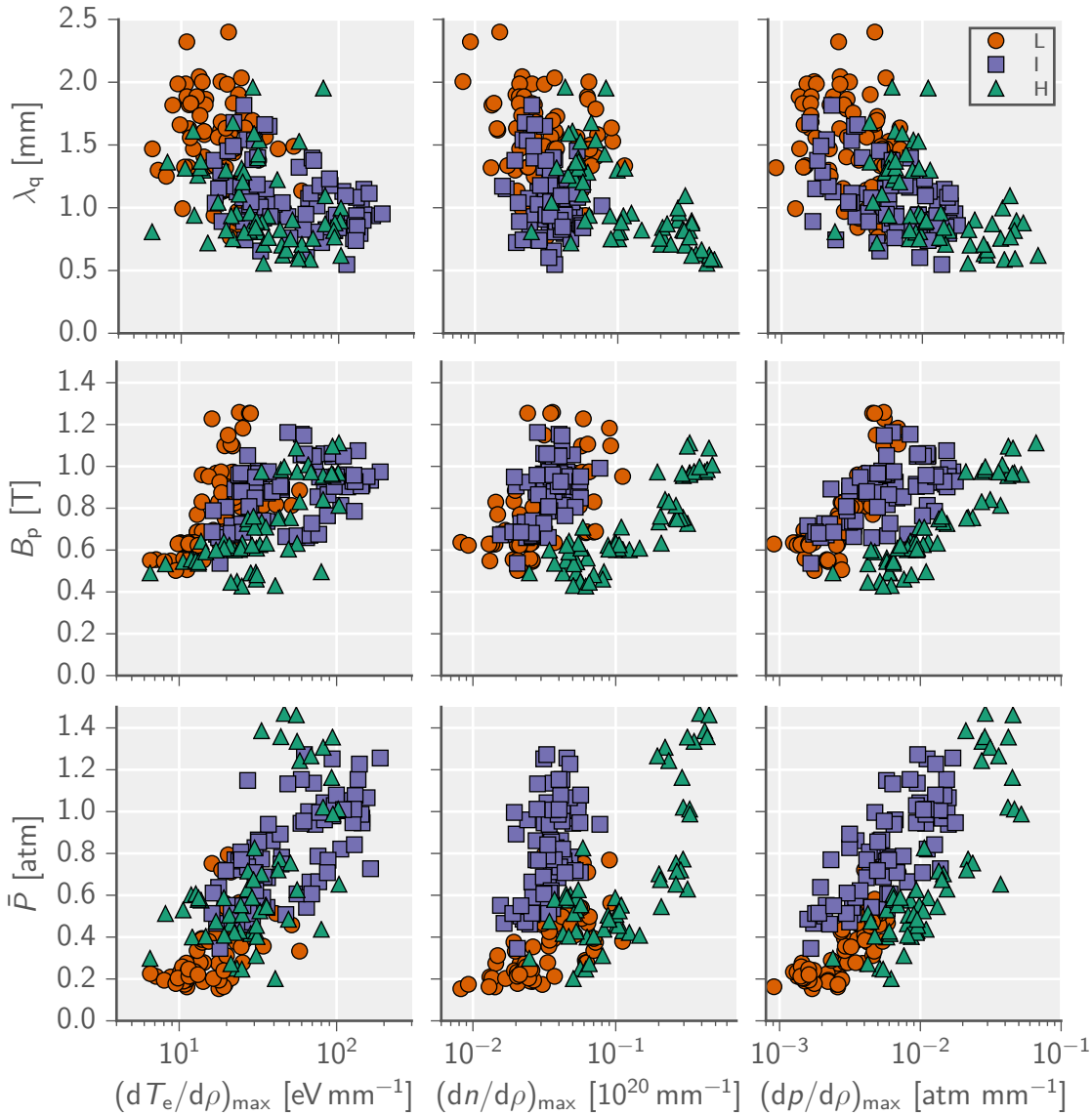

Figure 32. Values of the divertor heat flux width (top row), poloidal magnetic field (middle row), and volume-averaged plasma pressure (bottom row) plotted against the maximum gradients of the electron temperature (left column), density (middle column), and pressure (right column). Edge electron temperature and pressure gradients organize both the divertor heat flux width and the core plasma pressure well across confinement regimes.

Next Steps in Data Analysis

We are continuing to perform detailed analysis of the C-Mod heat flux width dataset. Empirical scaling relationships will be fit to the data to encapsulate the dominant trends. These results will be drafted into a manuscript for publication.

(2) Investigate divertor heat flux profiles and widths near the inner strike point in I-mode plasmas

Goal: Examine and document heat flux profiles at the inner target and its heat flux width scaling for I-modes plasmas, which typically have enhanced heat fluxes at the inner strike location – an important consideration for application in ITER or a reactor.

IR Thermography of the Heat-Flux Footprint on the Inner Divertor Target

An IR camera was installed to view the molybdenum tiles of the inner, high-field side (HFS) divertor target. The region viewed is illustrated (green circle) in Figure 32, along with the cross-section of C-Mod's lower divertor. The inner target is vertical and the tiles are shaped toroidally so that they present ~ 10 mm wide facets that are tilted at a 2.1 degree angle with respect to a purely toroidal field-line.

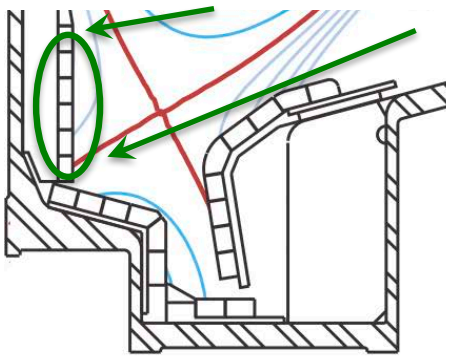

Figure 33. Cross-section of C-Mod's lower closed divertor, showing the vertical inner target. The IR camera views the target within the green circle along sight-lines that angle down from the right (green arrows).

We used the camera to perform thermography of the tile surfaces. Emission in the 3-5 micron band was measured with a time resolution of 380 frames per sec (Δt=2.6 ms) and an integration time that varied between 2 and 10 μsec. The pixel-to-pixel spacing on the image of the target is ~0.3 mm, and ~1 mm features in the target emission are resolved by the analysis, yielding a spatial resolution of ~0.2 mm when the features are mapped magnetically to the LFS midplane.

The detected IR emission is calibrated *in situ*, using thermocouples imbedded in the target tiles, to yield surface temperatures for each discharge. Measurements of temperature and emission are made ~30 s after each discharge when the bulk and surface temperatures for each tile have equilibrated. We assume that the Mo tile emissivity does not change over the temperature range spanned between the post-shot TC calibration and during the discharge. A 1D model of the heat diffusion through the tile is used, along with a constraint that the surface heat

flux be non-negative (which accounts for surface films, e.g., boron), to calculate the surface heat flux, $q_{surf}(d,t)$, from the time-histories of the surface temperatures, where d is the distance along the target.

Heat-Flux Widths for the Inner Divertor Target in I-mode

Using the IR thermography, we have investigated the heat-flux footprints on the inner target for single-null I-mode plasmas. The parallel heat-flux footprint for an axisymmetric inner target (mapped to the LFS midplane), $q_{||}(\rho,t)=q_{surf}(d,t)/sin\theta$, is calculated, as is the total power to the inner target. The profiles are fit to the following function (the so-called Eich-function):

$$q_{\parallel}(\rho) = \frac{q_{||0}}{2}\exp\left(\left(\frac{S}{2\lambda_{\mathrm{q}}}\right)^2 - \frac{\rho}{\lambda_{\mathrm{q}}}\right)\mathrm{erfc}\left(\frac{S}{2\lambda_{\mathrm{q}}} - \frac{\rho}{S}\right) + q_{\mathrm{BG}} \qquad (1)$$

where fitting parameters $q_{||0}$, λ_q, S, and q_{BG}, represent the peak parallel heat-flux entering the divertor ($q_{||0}$), the characteristic length for heat-flux spreading into the SOL (λ_q), the characteristic width for heat-flux spreading along the divertor leg (S), and the spatially-uniform "background" heat-flux (q_{BG}), respectively. ρ is the radial distance beyond the last-closed-flux-surface mapped to the LFS midplane. Examples of measured profiles and the "Eich-function" fit to the profiles are shown in the following three figures. We also characterize the heat-flux footprint profiles with a simple full-width, half-maximum (FWHM) for the profile. The λ_q, S, and FWHM parameters are used for examining the scaling the footprints, both for different conditions on the same device and for multi-device comparisons.

The profiles illustrated in Figures 33-25 show that the inner-target heat-flux widths can be quite small in C-Mod, consistent with the observations of small widths at the *outer* targets as discussed in reference [18] and in Section (1) above. In Figure 36 we show the same data as in Figure 28, but we have added some of the heat-flux widths obtained from analysis of the inner target footprints (the λ_q's), shown as pink 4-cornered stars. It is evident that the inner target widths are similar to those at the outer target. The data points for the inner target widths are the *minimum* widths that are measured for a given discharge. However, we also measure widths that are significantly larger, as illustrated in Figure 34, where two heat-flux profiles *from the same I-mode discharge* are shown, one has a narrow footprint profile, while the other, measured only 0.17 s later, is significantly larger. There was no change in engineering parameters over that time interval. This is an illustration of the scatter in the heat-flux width data. The magnitude of the

scatter for the widths at the inner target for I-mode confinement discharges is indicated by the shaped pink region in Figure 37. While the reason for this scatter within a given discharge or between discharges that are nominally similar is not known, we assume that there are "hidden variables" associated with this scatter, likely correlated with the quality of plasma confinement, such as pedestal gradients and core plasma pressures. This is also the case for the widths at the outer target, as discussed in Section (1) and shown in Figure 30 and Figure 31. The large scatter in the widths observed for the inner divertor remains a topic for further study as well. Note that even these minimum inner target widths appear to be somewhat larger (~1 to 1.5x) than those measured by the surface thermocouples at the outer target, but are within the scatter of all of the C-Mod measurements of outer target widths. (The outer target widths have been measured using both IR thermography [1, 5] and surface thermocouples, and we find that the thermography widths are typically somewhat larger. So, there may be systematic differences that arise from the measurement technique.)

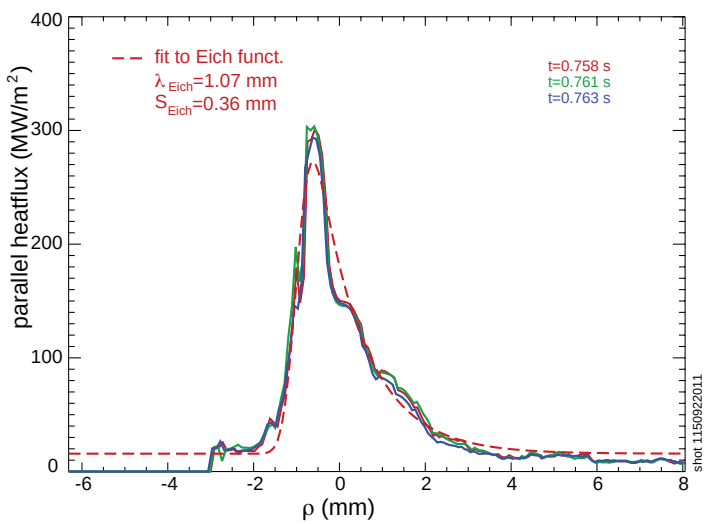

Figure 34. Three consecutive (in time) measured profiles of $q_{||}$ along with a fit to the Eich function (dashed line), exhibiting the expected footprint shape (sharper decay into the PFZ). This is from a I_p=1.0 MA, B_t=5.4 T I-mode discharge. Note the small values for both λ_q (~1 mm) and S (~0.36 mm). The misalignment of the strike-point (ρ=0) and the peak in the profile is within the uncertainty of the EFIT reconstruction of the magnetic configuration.

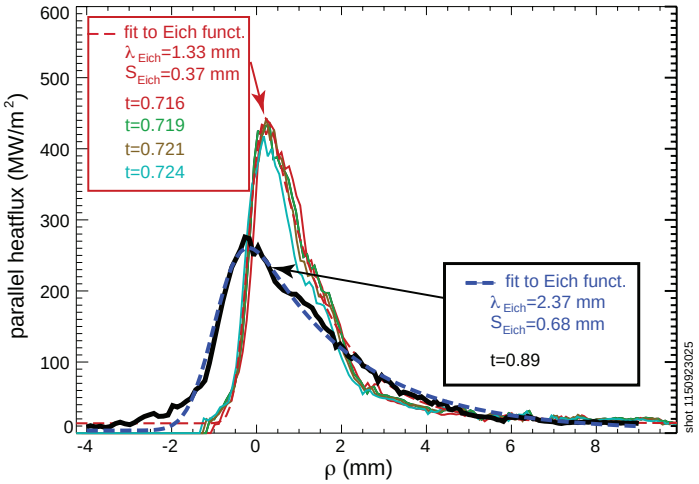

Figure 35. Similar to Figure 33, but with profiles from a I_p=1.1 MA, B_t=5.7 T I-mode discharge. The more peaked set of profiles are from four time slices at t~0.72 s, while the profile in black was measured only 0.17 s later in the same I-mode discharge. Its Eich-fit is shown by the blue dashed line. The fit parameters are given in the boxes on the top-left and right respectively. The engineering parameters did not change over that time interval.

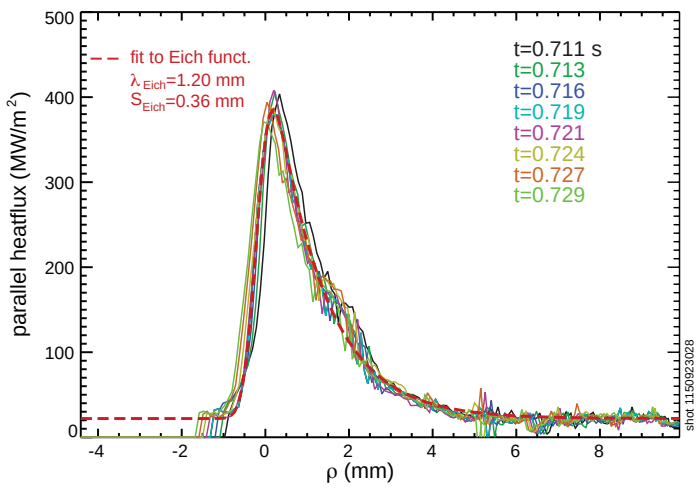

Figure 36. Similar to Figures 33 and 34, but with eight time slices from a I_p=1.1 MA, B_t=5.7 T I-mode discharge.

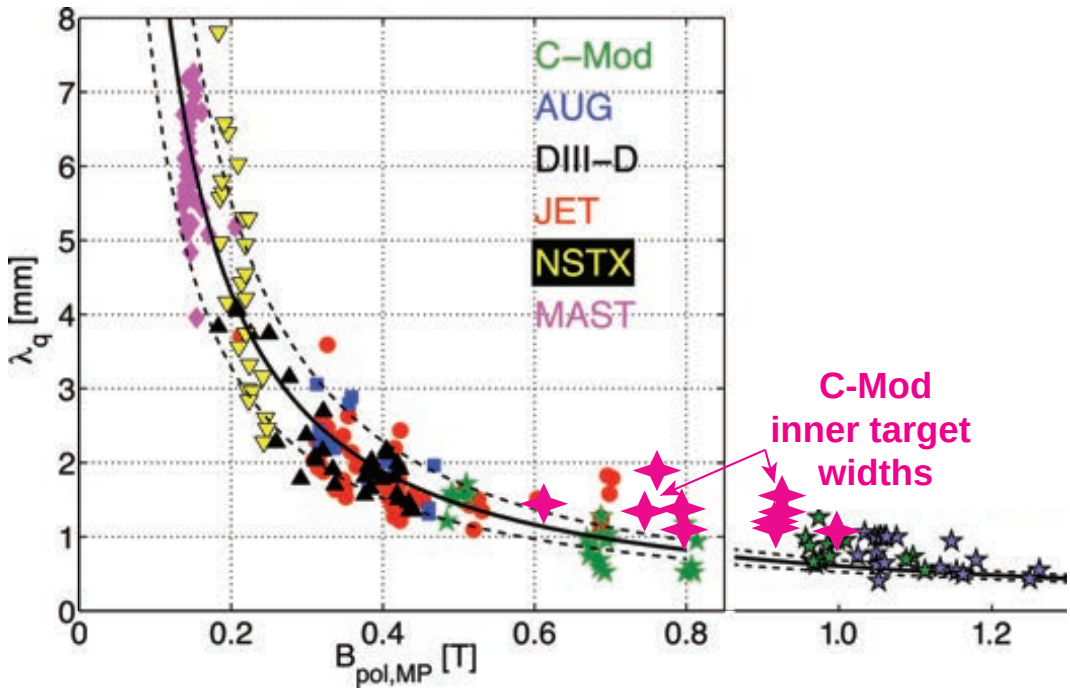

Figure 37. Same data as was shown in Figure 28, i.e., λ_q vs B_{pol}-at-the-outboard-midplane, but with some of the points from the footprint analysis of C-Mod's inner divertor target (pink 4-cornered stars).

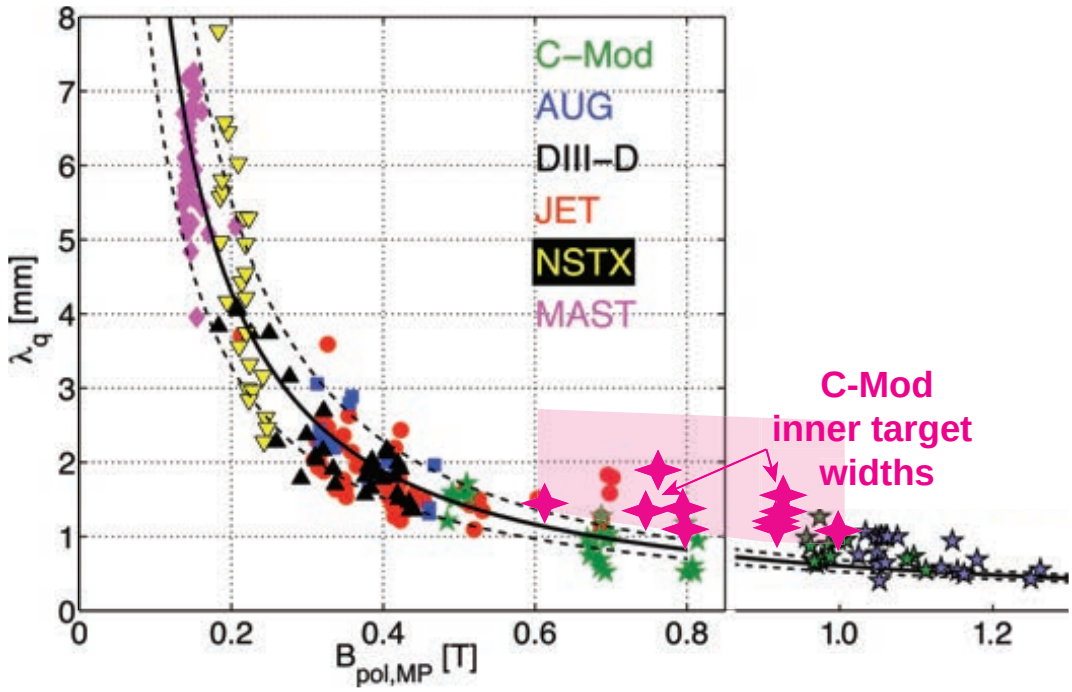

Figure 38. Same data as in Figure 36 with the pink 4-cornered stars corresponding to the minimum heat-flux widths at the inner divertor for a given discharge and the pink shaped region giving the range/scatter of inner leg widths.

Over the range of B_{pol} spanned by C-Mod's inner target data points, we cannot discern a clear inverse scaling of λ_q with B_{pol}. However, when combined with the multi-machine H-mode data from the outer targets that is the experimental basis for the Eich-scaling, we can say that the inner target I-mode λ_q's are consistent with that scaling.

Next Steps in Data Analysis

We will look for any confinement-mode dependences in the inner target widths, i.e., comparing the I-mode widths with those in EDA H-modes, quiescent ("ELM-free") H-modes, and L-modes. We will also examine magnetic-configuration effects (LSN, near-DN, and USN), with particular attention to near-double null configurations. As is the case with the outer target heat-flux widths, we will continue to search of "hidden variables" that result in a scatter of the inner target widths above the observed minimum. This work will be presented at the 2017 APS-DPP meeting.

(3) Explore divertor conditions in near-double null configurations

Goal: Document heat flux widths and heat flux sharing on all divertor target surfaces (inner/outer and upper/lower) as a function of magnetic flux balance in L-mode, H-mode and I-mode. Fusion reactors will likely operate in double-null to spread heat exhaust on the largest surface area possible and/or minimize heat to the inner divertor strikepoint locations. The overall distribution of power at high poloidal magnetic field where the heat flux widths are narrow is of particular interest.

L-Mode Data Set

During the FY16 run campaign, a series of L-mode plasmas were produced at three different plasma currents (0.55, 0.8, 1.1 MA) and varying amounts of upper-lower magnetic flux balance – from lower-single null dominant (negative δR_{sep}), double null ($\delta R_{\mathrm{sep}} \sim 0$) and upper single null (positive δR_{sep}) – where the degree of double-null is indicated by the distances between the two separatrices mapped to the outer mid-plane (δR_{sep}). Plasma densities were set low to ensure that all divertors were in a non-dissipative regime. Complete divertor profiles of density, electron temperature, ground current, and parallel heat flux for all four divertors and three plasma currents are given in Figures 38-40. These plasmas were in 'forward' field where the grad-B drift direction is pointed downwards.

The shapes of the heat flux profiles remain remarkably consistent as the magnetic equilibrium is swept through double null, with both the private flux and the common flux profiles maintaining similar e-foldings. Of course, the ρ value where the two meet changes, based on the relative positions of the two separatrices. The density profiles in the common flux on the outer divertors are rather broad whereas on the inner divertors they are much steeper. The electron temperature profiles in the common flux display two characteristic scale lengths: a very narrow heat conduction channel near the strike point and a much broader profile further into the boundary. These temperature and density profiles together result in a heat flux profile in the common flux on the outer divertors with a narrow 'near-SOL' heat flux width and a wider 'far-SOL' heat flux width.

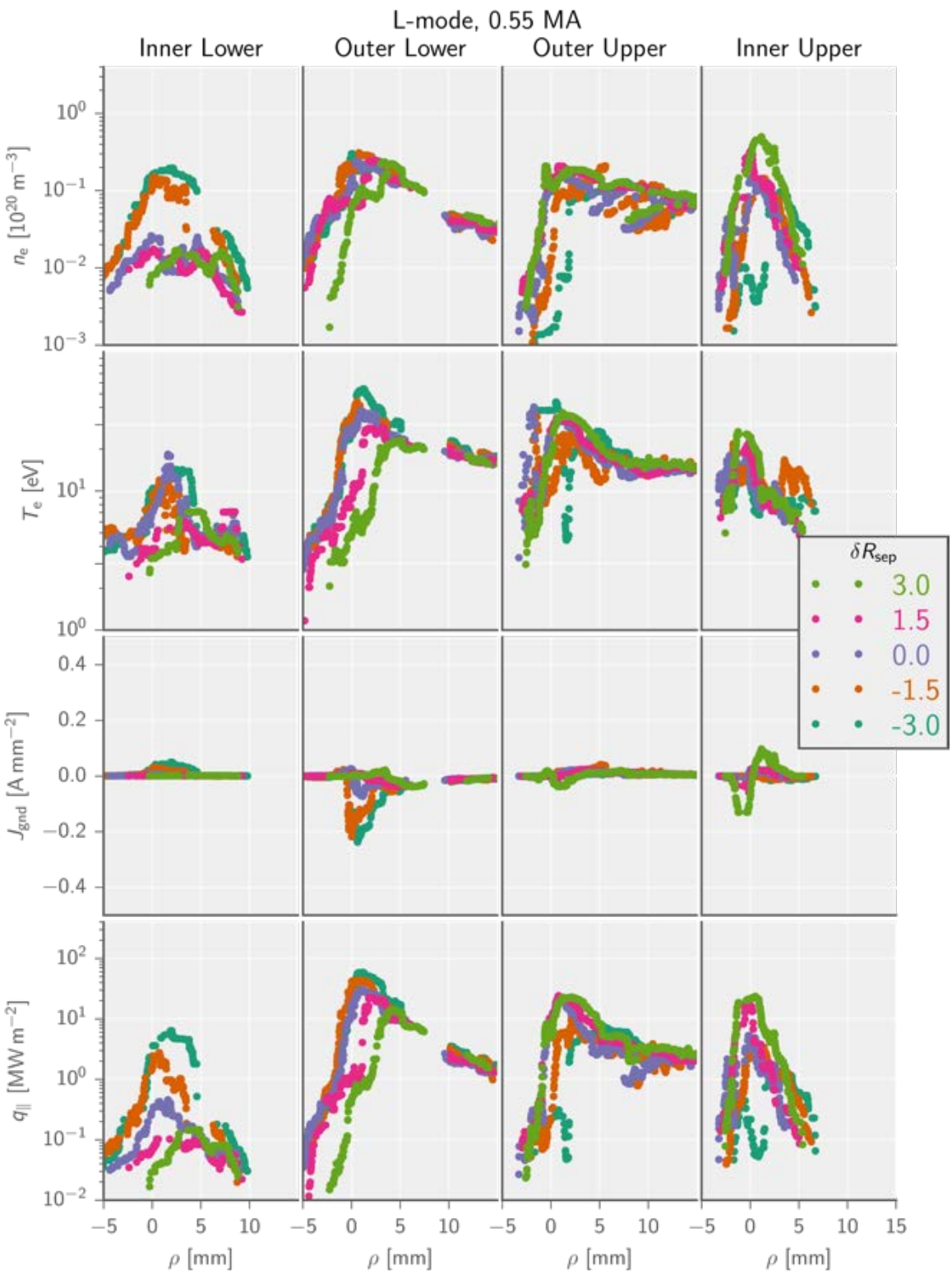

Figure 39. Divertor profiles of density, temperature, ground current, and parallel heat flux for 4 divertors around double null.

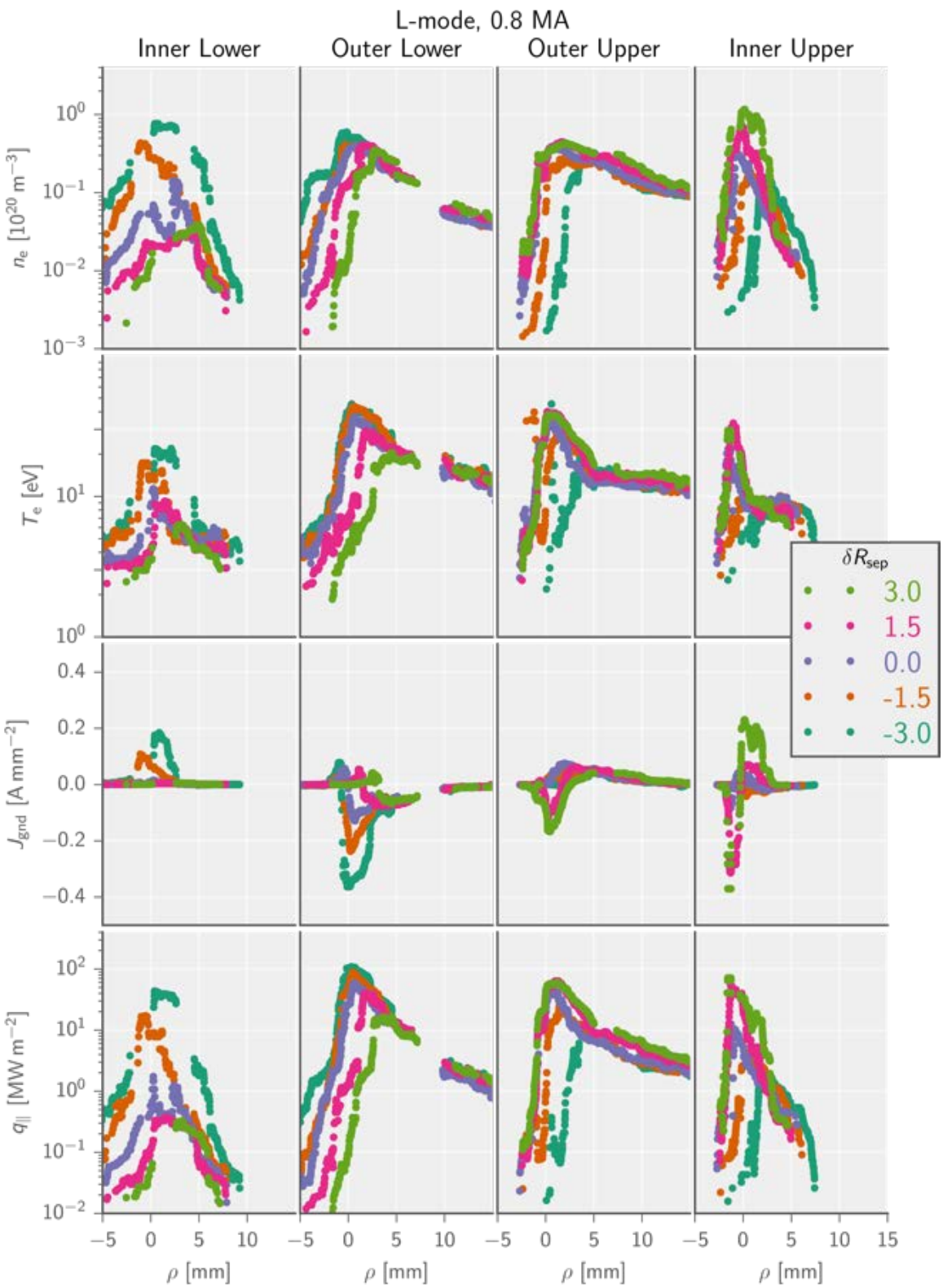

Figure 40. Divertor profiles of density, temperature, ground current, and parallel heat flux for 4 divertors around double null.

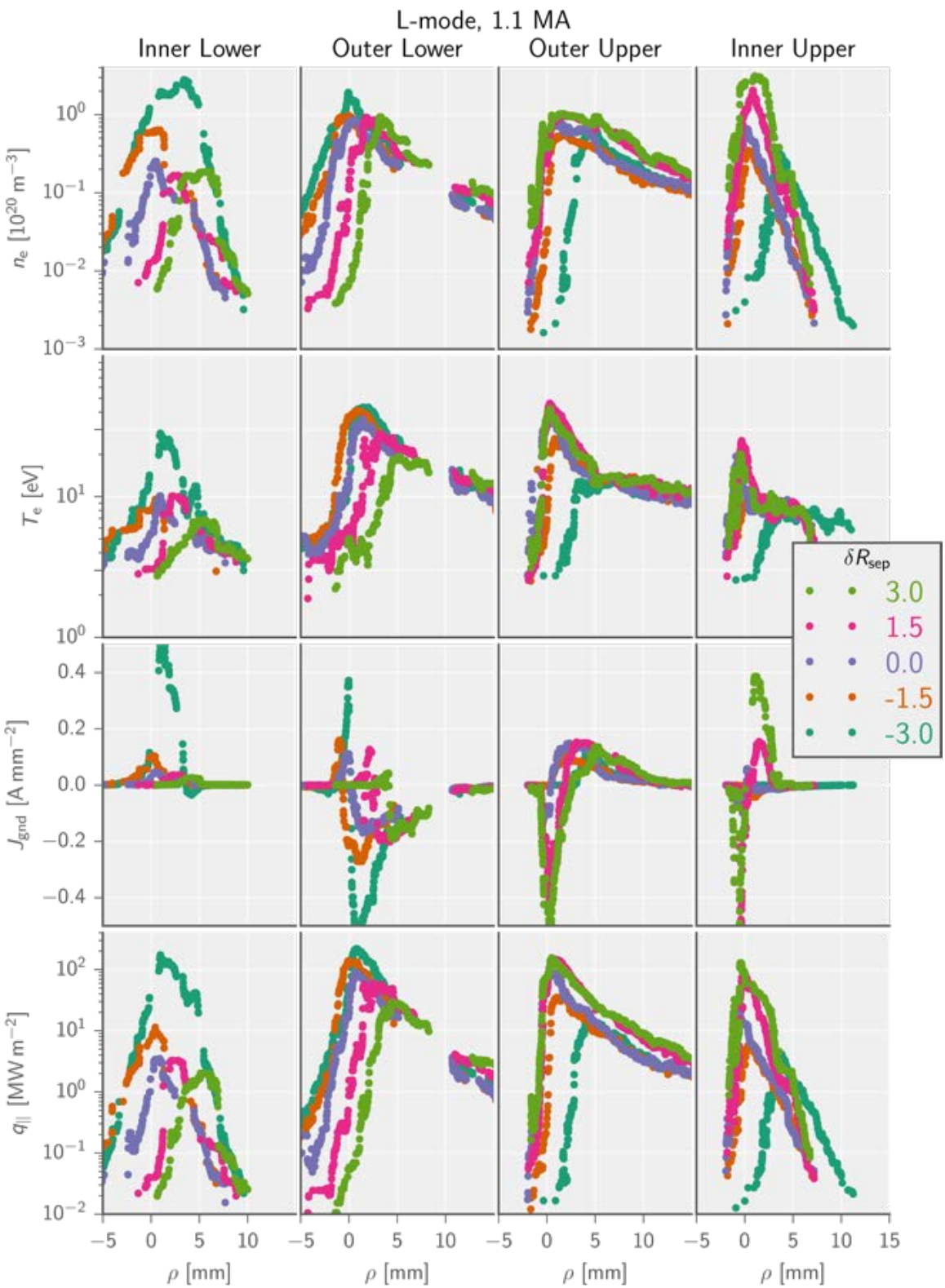

Figure 41. Divertor profiles of density, temperature, ground current, and parallel heat flux for 4 divertors around double null.

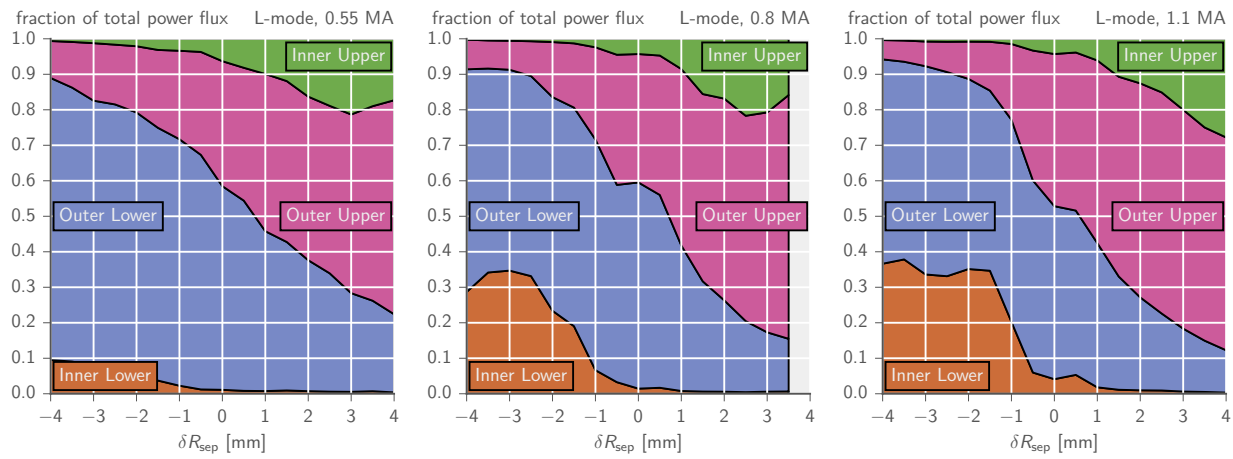

Figure 42. Power flux balance among 4 divertors around double null conditions for 3 plasma currents.

The relative balance of power flowing to the four divertors is important to understand for the controllability requirements of maintaining a plasma near double null. Figure 41 shows the relative power fractions to each divertor for the three different plasma currents. As the plasma current increases and the scrape-off layer narrows, the sensitivity of the power balance to the divertors increases. Within ~1 e-folding of balanced, the power to the inner divertors remains quite low, <10%. Within ~2 e-foldings of balanced, the power to the inner divertors quickly rises, coming to ~25%. The position where the power is balanced between the upper and lower divertors is between ~0.5 and ~0.75 mm towards upper null (grad-B direction away from the primary x-point). It is not straightforward to separate whether this is due to a plasma transport affect or a systematic error in the magnetic equilibrium reconstruction.

We have found that the heat flux sharing amongst the divertors follows a mapping of magnetic flux balance (δR_{sep}), which can be represented as a logistic function for the power flux sharing. The inner and outer divertors are found to have different characteristic upstream heat flux power sharing widths. The ratio of the power to the lower (outer or inner) divertor to the total to the lower and upper (outer or inner) divertors is found to be:

$$\frac{P_{\mathrm{ol}}}{P_{\mathrm{ol}}+P_{\mathrm{ou}}} = \frac{1}{1+e^{\delta R_{\mathrm{sep}}/\lambda_{\mathrm{o}}}}, \tag{2}$$

$$\frac{P_{\mathrm{il}}}{P_{\mathrm{il}}+P_{\mathrm{iu}}} = \frac{1}{1+e^{\delta R_{\mathrm{sep}}/\lambda_{\mathrm{i}}}}. \tag{3}$$

These relationships indicate that the power balance between upper and lower divertors can be expresses as hyperbolic tangent function of $\delta R_{sep}/2\lambda_o$, similar to what was found on DIII-D but deduced here by forming a ratio of the above two expressions:

$$\frac{P_{ol}-P_{ou}}{P_{ol}+P_{ou}} = \frac{1-e^{\delta R_{sep}/\lambda_o}}{1+e^{\delta R_{sep}/\lambda_o}} = \tanh\left(\frac{-\delta R_{sep}}{2\lambda_o}\right). \quad (4)$$

The in-out power sharing does not have a similar simple relationship, but is found the be Gaussian-like:

$$\frac{P_{il}+P_{iu}}{P_{il}+P_{iu}+P_{ol}+P_{ou}} = P_{i,0} + \left(P_{i,0} - P_{i,\infty}\right) * \left(1 - \frac{2}{1+e^{-\left(\delta R_{sep}/\lambda_{io}\right)^2}}\right), \quad (5)$$

where $P_{i,0}$ is the fraction of the power to the inner divertors at $\delta R_{sep} = 0$ and $P_{i,\infty}$ is the fraction of the power to the inner divertors at $\delta R_{sep} = \pm\infty$.

These equations are fit to the experimental profiles in Figure 42. The logistic and Gaussian fits are allowed to be translated linearly in δR_{sep} by a quantity ρ_0. The logistic fits to both the inner and outer up-down ratios match the data quite well. This simple model is clearly adequate to describe this power flux ratio around double null. The e-foldings display the characteristic inverse dependence on plasma current (or equivalently poloidal magnetic field, in C-Mod $B_p \cong 0.77\times I_p$). The inner divertor e-folding appears to have a slightly stronger than inverse scaling and the outer divertor a slightly weaker. However, due to the small amount of data within this scan we will not look too much into these differences. The e-folding for the outer divertor is consistently ~3 times larger than that for the inner divertor. This is consistent with the narrower inner divertor heat flux profiles shown in Figures 38-40 as well as upstream measurements. The inner up-down ratio is shifted to negative δR_{sep} whereas the outer up-down ratio is shifted to positive δR_{sep}. This is consistent with poloidal $E_r\times B$ heat convection pushing heat from the inner lower divertor to the inner upper divertor and from the outer upper divertor to the outer lower divertor. The shifts have very similar values between the inner and outer divertors. And they decay to lower values at higher poloidal magnetic fields.

The story for the Gaussian-like fit to the in-out ratio is not as satisfying. The examination would benefit from a wider scan in δR_{sep}, especially at low poloidal field where the e-foldings are long. At the minimum near-double-null the fraction of the total power flux to the inner divertors is consistently ~5% across the poloidal field scan. Far away from double null the fraction of the total power flux to the inner divertors is ~20% to 25% with perhaps a slight increase with poloidal magnetic field. The offset in δR_{sep} is essentially zero for the larger poloidal magnetic field cases, indicating perhaps very accurate magnetic reconstructions of the plasma equilibrium. The offset at the lowest field is much larger. However, the very small amount of data from the inner divertor and the limited scan of δR_{sep} with respect to the SOL width lends low confidence to the precise value of this data point. The e-foldings for the Gaussian-like fit are much closer to those for the outer divertor up-down ratio than that for the inner divertor. This suggests that heat transported from the low field side SOL to the high field side in the low field heat flux channel and then narrows at the high field side.

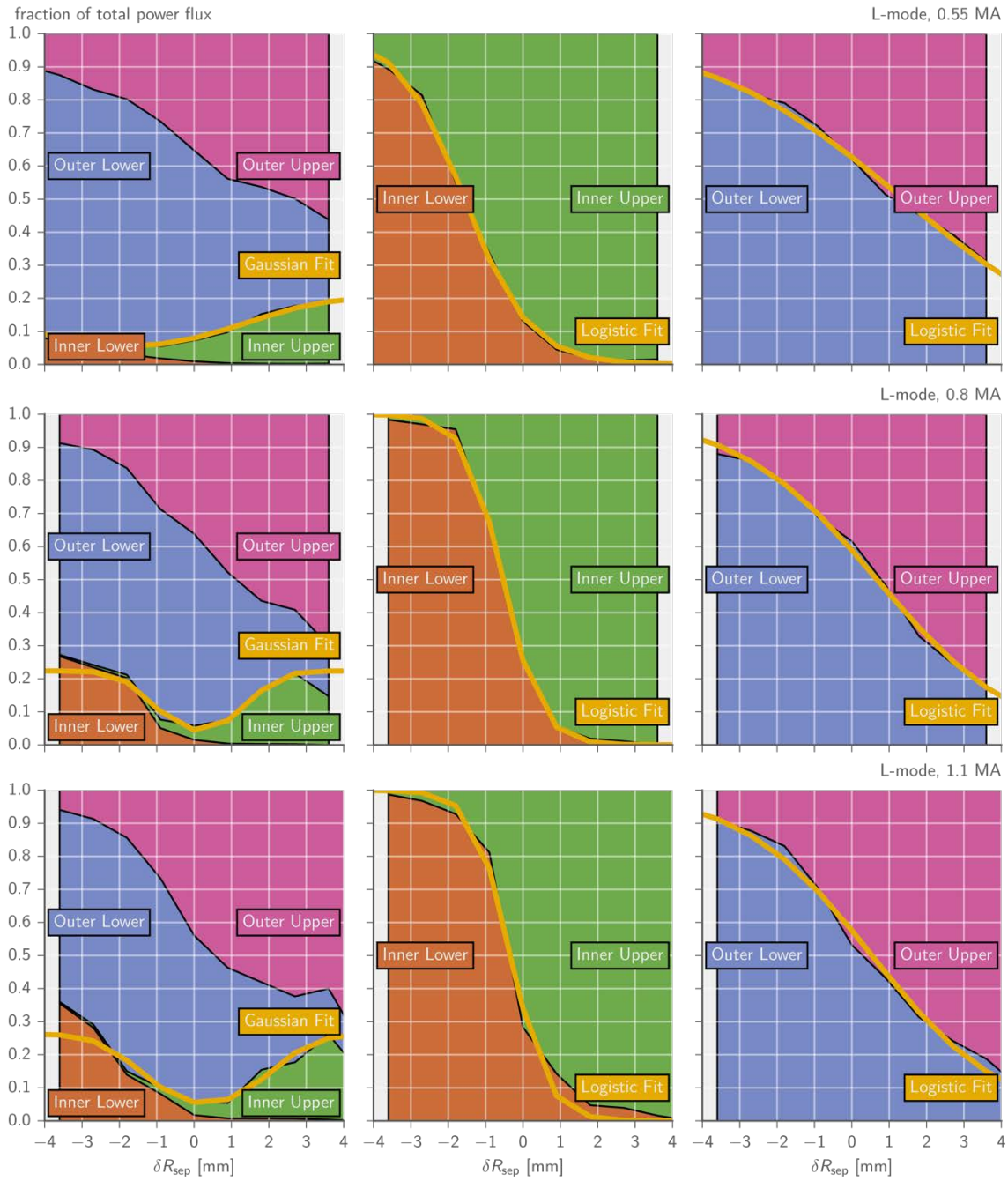

Figure 43. Comparison of analytic fits and measurements of power sharing. The rows of panels correspond to different plasma currents (0.55, 0.8, 1.1 MA top to bottom). The left column shows the in-out ratio (orange+green region compared to blue+pink region), middle column is the up-down ratio for the inner divertors, and right column is the up-down ratio for the outer divertors. The yellow line is the boundary from the fit.

An additional way of quantifying the power balance among the divertors is to fit the divertor heat flux profiles with an analytic function and observe how the fitting parameters vary with δR_{sep}. The 'Eich' equation is a common one used to parameterize boundary profiles [6]. It is the result of convolving an exponential profile (truncated at $\rho = 0$ and e-folding λ_q) and a Gaussian (width S):

$$q_{\parallel}(\rho) = \frac{q_0}{2} \exp\left(\left(\frac{S}{2\lambda_q}\right)^2 - \frac{\rho}{\lambda_q}\right) \operatorname{erfc}\left(\frac{S}{2\lambda_q} - \frac{\rho}{S}\right). \tag{6}$$

As with the functions fitted to the power ratios, we allow this to be shifted linearly be the free parameter ρ_0. Here we omit the background heat flux term since the measurements are not with thermal sensors (e.g., IR or surface thermocouples) but plasma flux. Thus they do not see a 'background' heat flux, which if real is typically from radiation.

The results of fitting the 'Eich' profiles are shown in Figure 43. The fitted peak power flux (q_0) behaves as expected, highest when a divertor is primary and decaying away as the divertor becomes secondary. The fitted spreading factor (S) has error bars up to the same order as the parameter. It neither has a clear trend with δR_{sep} nor has systematic differences between divertors. The spreading parameter is often considered representative of cross-field dissipation processes that is dependent on divertor geometry. However, we observe no clear differences amongst the divertors despite three very different divertor geometries. Although these measurements were under low dissipation conditions.

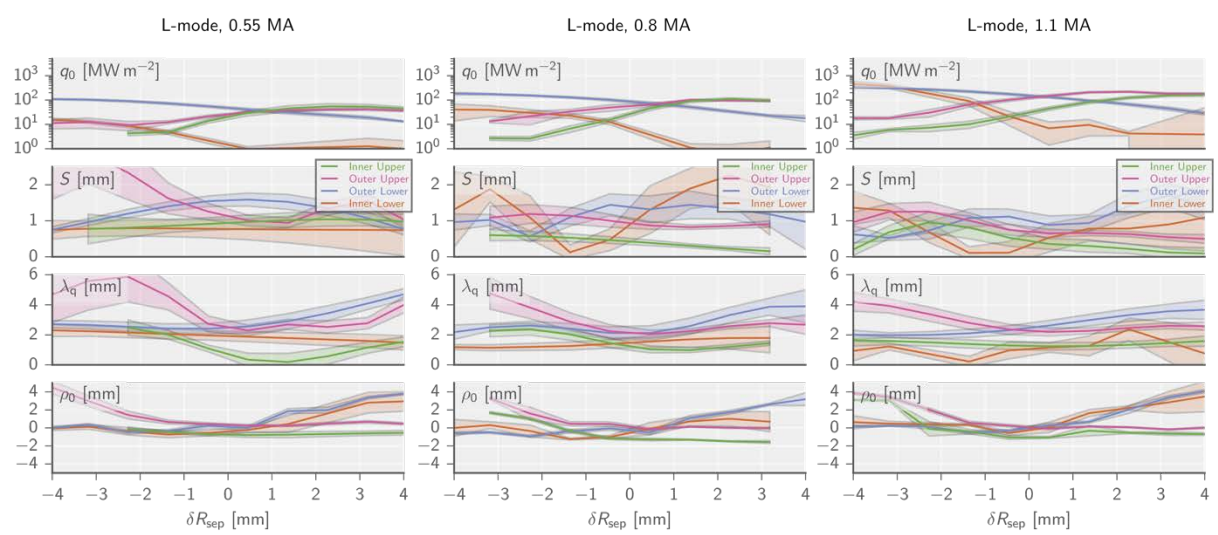

Figure 44. Fits of 'Eich' heat flux profile to divertor measurements. Columns left to right are of plasma current (0.55, 0.8, and 1.1 MA respectively). Top row is the peak heat flux, in absence of any cross-field 'spreading'. Second row is the 'spreading' factor. Third row is the heat flux width. Fourth row is the shift of the profile. Lines are color coded by divertor. Colored bands indicate 1 standard deviation error bars.

The fitted e-folding lengths (λ_q) exhibit differences among divertors and their trends with respect to δR_{sep} and plasma current. Consistent with the logistic fits, the inner divertors have systematically smaller λ_q than the outer divertors. The inner divertors have no clear trend with δR_{sep} across the plasma current scan. However, as the magnitude of δR_{sep} gets larger, the fitted λ_q for the secondary divertor gets larger. Examining Figures 38-40, we see that this trend is not due to an actual increase in the e-folding, but is instead due to the secondary far-SOL e-folding dominating the fit. A similar trend was seen in MAST.

Finally, the shift parameter (ρ_0) is relatively constant around $\delta R_{sep} = 0$ for the primary divertors and increases approximately linearly with δR_{sep} for the secondary divertors. These trends are as expected. For the primary divertors, the location of the peak heat flux in absence of spreading is at the strike point ($\rho_0 = 0$). For the primary divertors, this location follows the location of the secondary strike point ($\rho_0 = |\delta R_{sep}|$).

<u>H-Mode and I-Mode Data Sets</u>

The detailed studies were done in L-mode because it is much simpler to 'dial-up' consistent, repeatable shots and perform a systematic scan in δR_{sep}. However, any present credible reactor design relies on operating in a regime with higher confinement than L-mode. So, we performed power flux sharing scans of δR_{sep} for two stationary, high-confinement regimes: EDA H-mode and I-mode.

For the H-mode experiments, a nearly full scan of $\delta R_{sep} \pm 4$ mm was possible. For each shot, H-mode was initiated with $\delta R_{sep} < 4$ mm and then δR_{sep} was adjusted to the desired position for that shot. For the H-modes ~3 mm or greater into the 'unfavorable' drift direction the core confinement started to degrade and the H-mode would back transition to an L-mode.

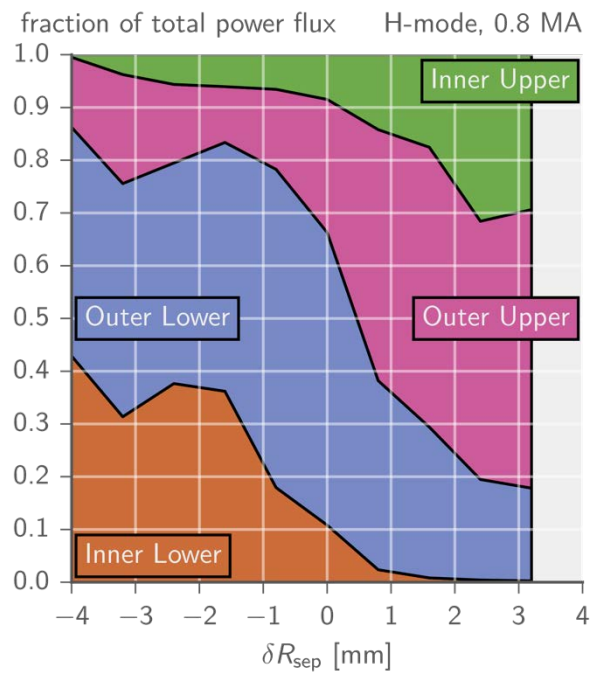

Figure 45. Power flux sharing for an H-mode case.

The power flux sharing with in H-mode, Figure 44, was similar to that for the L-mode but with a few key differences. The minimum power going to the inner divertor near double-null was ~2 times higher in H-mode than L-mode (~15-20% compared to ~7-10%). Also, the outer divertor up-down power ratio saturated at ~3:1 away from double null. In these H-mode discharges the outer divertor second e-folding contributes a much larger fraction of the total power flux to each divertor and the secondary e-folding length is much longer than the primary. When this is the case, the equilibrium must be very strongly away from double null to significantly reduce the power flux to the secondary divertor.

The I-mode experiments were operated in the opposite field direction as the L- and H-mode, with the B×∇B direction pointed away from the lower x-point. This is the configuration where the easiest and most robust access to I-modes is found. The I-mode experiments, like the H-mode, were initiated with $\delta R_{sep} < 4$ mm and then δR_{sep} was adjusted to the position for that shot. However, only a partial scan of δR_{sep} from -4 to -1 mm was possible. For larger values of δR_{sep} it would transition out of I-mode.

The I-mode δR_{sep} scan is not large enough to fit the analytic profiles. However, three important conclusions can be made from these data: (1) I-mode can be operated very near to double null. (2) The in-out ratio of power flux between the primary divertors is reduced relative to what is typically seen in strongly single null I-modes (δR_{sep}=-10 to -20 mm) from between 67% and 75% to between 5% and 25%, depending on δR_{sep}. This is a great reduction for the inner divertor power handling challenge. (3) It is close enough to double null that the secondary outer target helps in the power sharing, taking up to ~30% of the power flux.

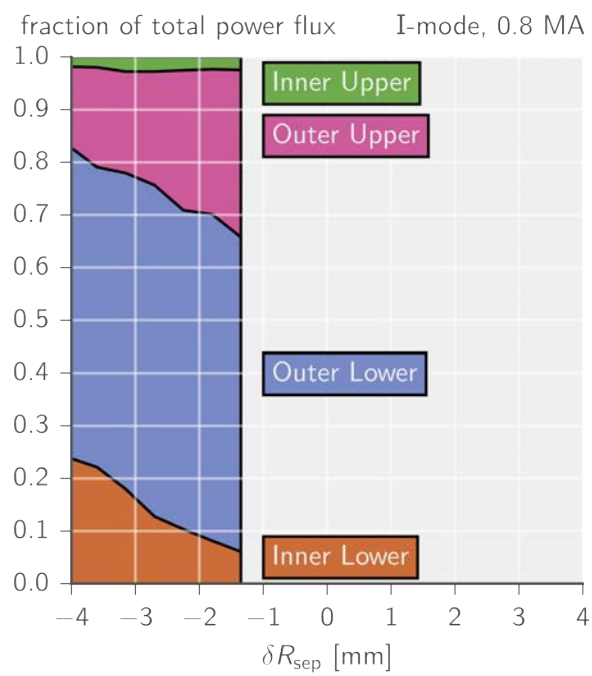

Figure 46. Power flux sharing for an I-mode.

<u>Next Steps in Data Analyses</u>

These results are being drafted in a paper to be submitted to Nuclear Fusion.

(4) Explore influence of divertor heat flux dissipation on SOL profiles

Goal: Examine and document the influence of feedback-controlled divertor nitrogen seeding on SOL profiles – both the near SOL heat flux width and the far SOL shoulder. Theory indicates that divertor target 'boundary conditions' can influence SOL turbulence and transport and thus the profiles – in particular, whether or not the turbulence is 'disconnected' along field lines into the divertor.

Feedback-Controlled Divertor Nitrogen Seeding – C-Mod Data Archive

During FY15 and FY16 run campaigns, dedicated experiments were performed to explore the effect of varying the level of divertor dissipation on 'upstream' electron temperature and density profiles. These experiments took advantage of a newly developed technique of real-time feedback control of nitrogen seeding via surface thermocouples [24]. Signals from a surface thermocouple array embedded into C-Mod's outer divertor (Fig. 46) were sent to analog circuitry that computes divertor surface heat fluxes in real time at each of the sensor locations. Signals from four or five sensors near the strike point position were used to feedback control divertor nitrogen seeding, which was introduced into the private flux zone via a fast-acting piezo valve. With this system, divertor heat fluxes could be reproducibly programmed to successively lower levels on a shot-by-shot basis while maintaining core plasma conditions essentially constant. At the same time, a scanning Mirror Langmuir Probe [25-27] was used to record midplane plasma profiles, exploring the influence that divertor conditions might have in affecting 'upstream' conditions, such as the power channel e-folding width.

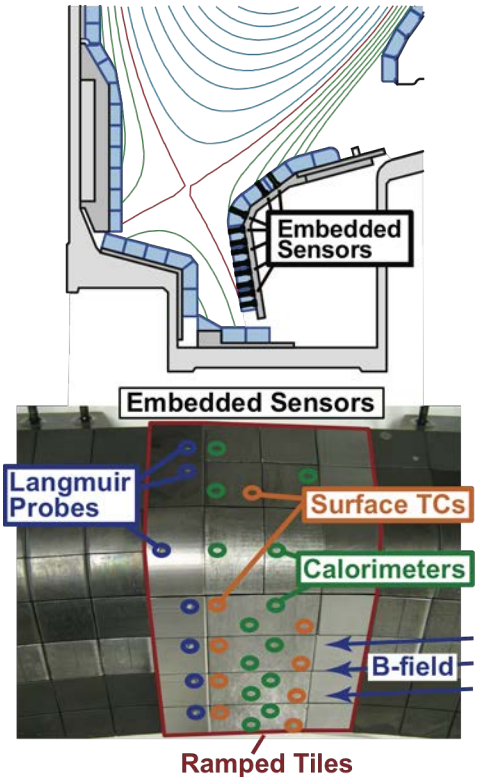

Figure 47. Location of surface therm-couple sensor array (Surface TCs) in a 'ramped tile' outer divertor module.

The experimental investigation focused on ohmic L-mode plasmas at three different plasma currents (1.1, 0.8, and 0.55 MA), fixed toroidal magnetic field (5.4 tesla) and line-averaged plasma densities (1.8, 1.3 and 0.9x1020 m-3), chosen to place the outer divertor in a low-recycling regime for the case of no nitrogen injection. This resulted in highly reproducible, relatively low power-density plasmas that were ideal for scrape-off layer profile measurements with the scanning MLP.

Figure 47 shows representative time traces from one such plasma (1.1 MA case). Real-time divertor surface heat flux signals deduced from five surface thermocouples are averaged together and used as an 'observer' to control nitrogen seeding (SURFTC 3+4+5+6+7). In response to

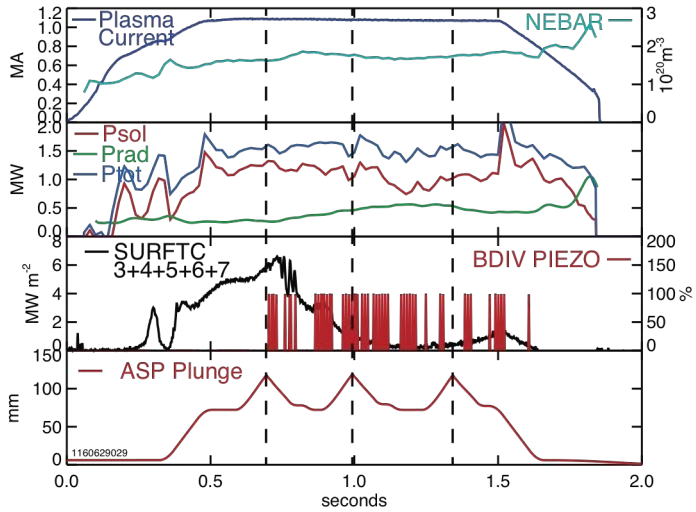

Figure 48. Representative plasma (1.1 MA, 5.4 tesla, ohmic heated) in which feedback controlled divertor nitrogen seeding was applied to reduce divertor surface heat fluxes to preprogrammed levels. Top panel: Plasma current, line-averaged density (NEBAR); Second panel: power input (Ptot), power radiated from core (Prad) and power into the scrape-off layer (Psol); Third panel: average divertor surface heat flux deduced from outer divertor target surface thermocouples (SURFTC 3+4+5+6+7) and divertor piezo duty cycle signal (BDIV PIEZO); Bottom panel: plunge depth of horizontal scanning probe.

feedback control, nitrogen is puffed into the divertor (BDIV PIEZO), reducing the average surface heat flux from ~6 to less than 0.2 MW/m2, while core plasma conditions are maintained constant. “Ptot” is the total power into the discharge and “Psol” is the power into the scrape-off layer. In this case, the horizontal scanning probe was plunged three times (ASP Plunge), recording scrape-off layer conditions for different levels of nitrogen seeding and divertor heat flux mitigation.

An analysis of the 1.1 MA dataset identified 21 high-quality SOL profile measurements with varying levels of divertor dissipation. Similarly, 16 and 32 high-quality SOL profile measurements were identified from the 0.8 MA and 0.55 MA datasets, respectively. In addition, good data were obtained from the outer divertor surface thermocouple array and the “rail” Langmuir probe diagnostic array for most cases. This recently installed, 21 probe array diagnostic (Fig. 48) [28] was found to be particularly valuable, recording profiles of divertor target conditions with high spatial resolution across the ‘vertical target’, ‘nose’ and ‘horizontal shelf’ regions the outer divertor. However, it should be noted that the rail probe diagnostic was implemented as an experiment in itself, with issues such as probe signal interpretation being an important part of the investigation. Consequently, some derived plasma quantities, such

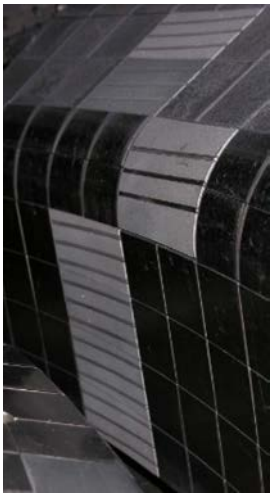

Figure 21. Outer divertor ‘Rail probe’ array consists of 21 flush-mounted probes, toroidally extended and aligned with the pitch of the local maanetic field.

as electron temperature and density, must be treated with caution while other quantities, such as net current density arriving on the divertor target, are expected to be very reliable. In addition, changes were made to probe electronics between FY15 and FY16 campaigns, which are known to affected some of these derived quantities, most notably electron temperature. Here we report 'raw' probe results in order to indicate overall trends. But please note that some of these values will likely be revised in the future.

Data Analysis Results – 1.1 MA Plasmas

Figure 49 shows magnetic equilibria that were used to perform these studies, which were slightly different in the FY15 and FY16 campaigns. During the FY15 campaign, an "ITER-like" configuration was used in which a secondary x-point in the upper divertor was located just outside the primary lower divertor x-point flux surface in the range of 3 to 8 mm when mapped to the outer mid-plane (see right panel of Fig. 49). For the FY16 campaign, this quantity (defined as 'SSEP') was in the range of 11 to 15 mm (left panel of Fig. 49), corresponding to a lower single-null dominant configuration. It is important to distinguish between these two configurations because the SOL and divertor profiles obtained during FY15 and FY16 campaigns were found to be slightly different under otherwise identical discharge conditions.

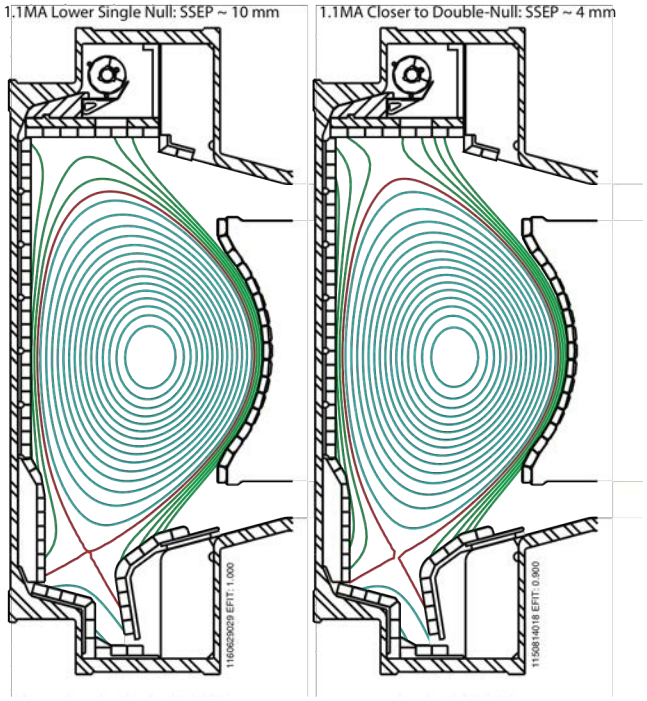

Figure 49. Representative magnetic equilibria for 1.1 MA plasmas. Experiments performed during 2016 campaign used equilibria with SSEP > 10 mm (left panel) while experiments performed during 2015 had SSEP < 10 mm (right panel).

Figure 50 shows core plasma line-averaged density, power into the SOL and divertor target electron temperature for the 21 time slices as a function of average parallel heat flux arriving outer divertor target -- here computed from the average of

a set of surface thermocouples near the strike point (typically 4 or 5). Nitrogen seeding reduces the divertor heat flux by an order of magnitude while the power into the SOL is only slightly affected. Eleven of these time slices were taken in the FY15 campaign with |SSEP| values less than 10 mm (right panel in Fig. 49). The other 10 samples where taken in the FY16 campaign with |SSEP| values greater than 10 mm. For each of these datasets, the level of divertor nitrogen seeding was the only external parameter varied.

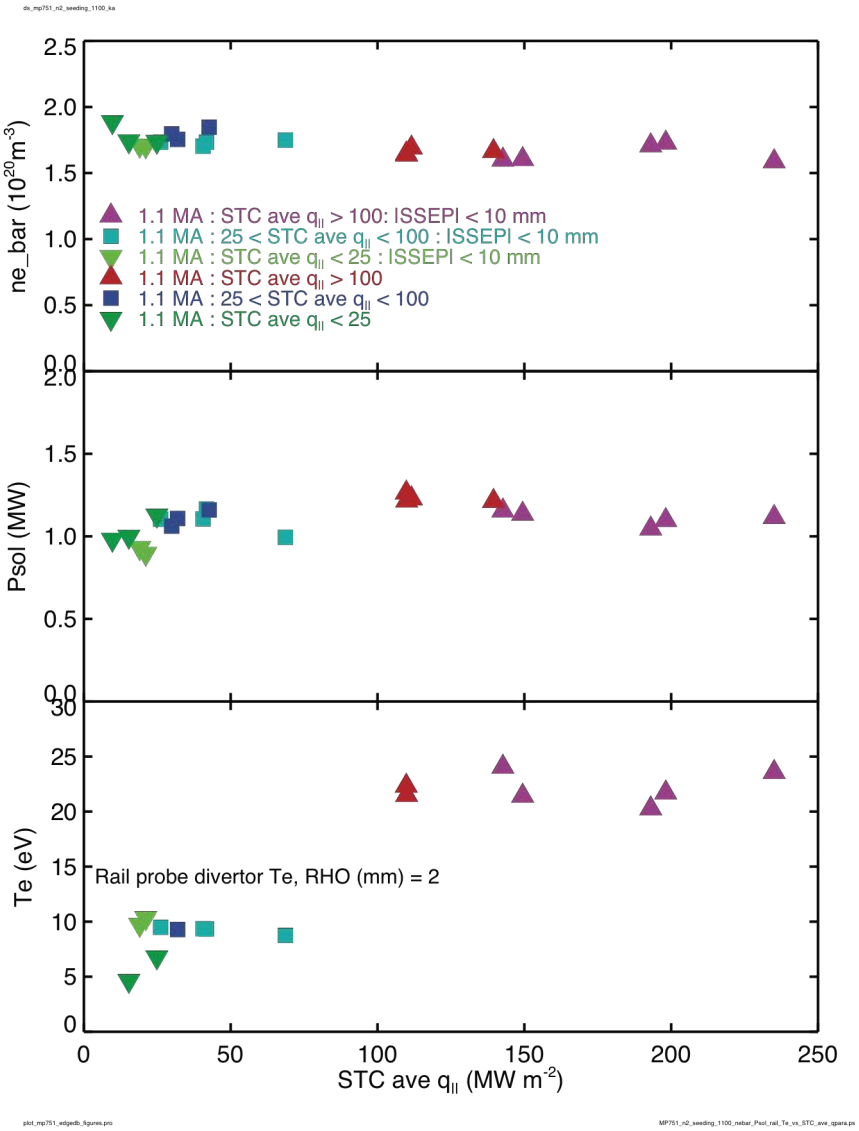

Figure 50. Line-averaged density (ne_bar), power entering into the scrape-off layer (P_{sol}) and divertor target electron temperatures versus parallel heat flux averaged over five surface thermocouples on the outer divertor (STC ave $q_{//}$). These 21 samples are taken at the time that the scanning MLP records SOL profiles in near-identical 1.1 MA, 5.4 tesla ohmic heated plasmas. Eleven time slices were taken in the FY15 campaign and ten from the FY16 campaign. The SSEP values where different between campaigns, so these data are analyzed as two separate groups. For each of these datasets, the level of divertor nitrogen seeding was the only external parameter that was varied. It caused divertor surface heat fluxes to drop by an order of magnitude while power into the SOL remained approximately constant; a minor reduction in P_{sol} is evident at the highest levels of N_2 seeding. In response, outer divertor target temperatures recorded by Rail probes 2 mm into the SOL mapped to the outer mid-plane (Rho) dropped substantially, indicating a transition from sheath-limited to high-recycling, approaching partially detached conditions. The different symbols and colors are use to mark the relative power level arriving on the outer divertor target here and in subsequent figures.

Divertor Conditions in Response to N_2 Seeding – 1.1 MA Cases

Figure 51 shows divertor target plate profiles (electron temperature, net parallel current density arriving at the target plate and parallel heat fluxes) in response to nitrogen seeding for the FY16 and FY15 datasets. Plasma conditions near the strike point ($0 < \rho < 2$ mm) are strongly affected. Parallel heat fluxes near the strike point drop by an order of magnitude as divertor target conditions near the strike point vary from sheath-limited (25 – 30 eV) to high recycling, or at some locations, near detached (~ 7 eV). Net parallel current density to the plate also drops by an order of magnitude indicating that the target plate becomes 'electrically disconnected' from the main chamber SOL plasma as the divertor approaches partial detachment. (Due to improvements in probe bias electronics, the 'raw' electron temperatures reported by the Rail probe array are lower in the FY16 campaign, which we take to be more accurate.)

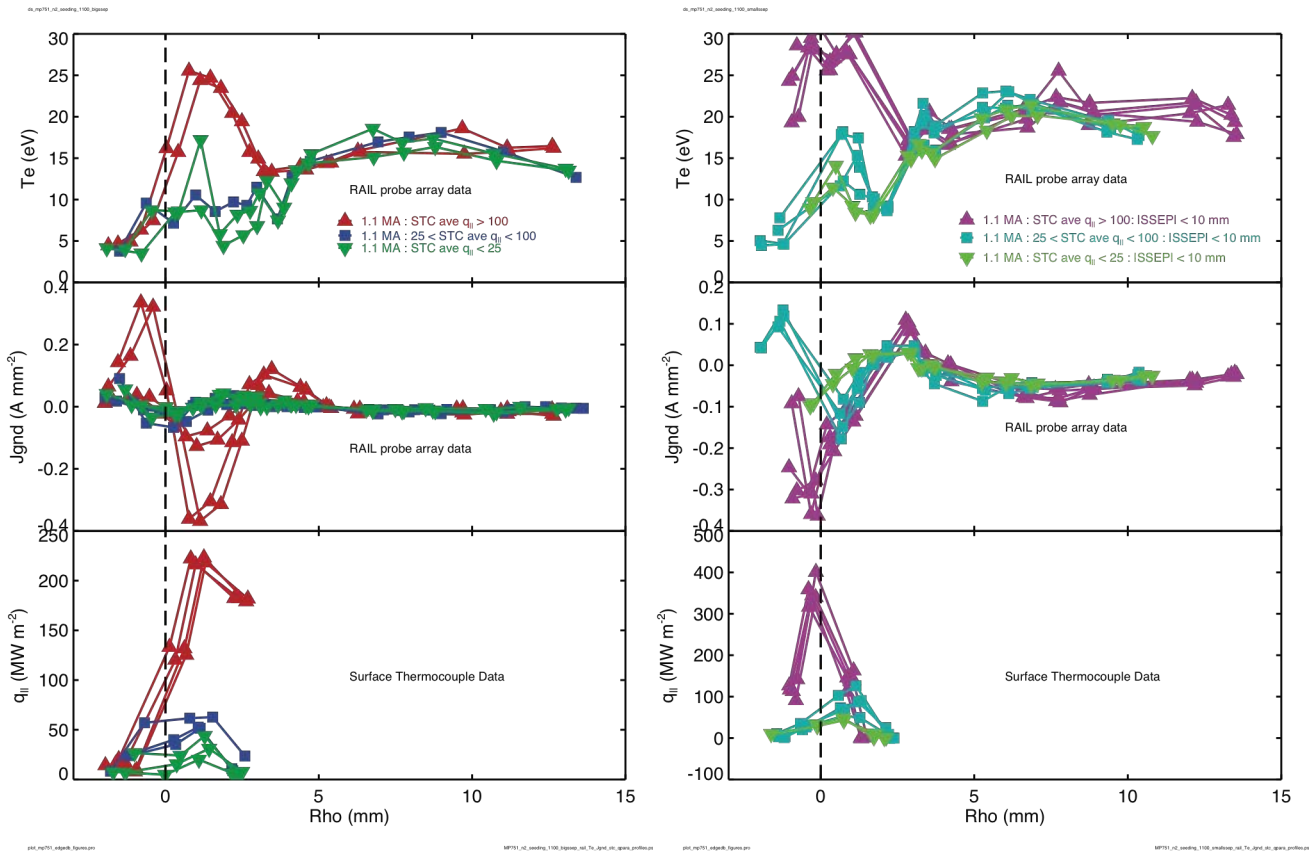

Figure 51. Profiles of outer divertor electron temperature and net parallel current density arriving at the plate as recorded by Rail probe array and parallel heat flux as inferred by surface thermocouple array. Left panels are data take from the FY16 campaign, right panel are from FY15. Rho is the distance into the SOL mapped to the outer midplane. Symbol colors indicate the relative level of heat flux density arriving on the outer divertor.

The peak in electron temperature near ρ ~1 mm is likely a 'death ray' artifact, which has been seen before on standard probes as divertor conditions approach detachment [29]. Under these conditions, it is known that a Langmuir probe will overestimate the electron temperature and record anomalously high ion saturation currents.

Midplane SOL Profiles in Response to Divertor Seeding – 1.1 MA Cases

Midplane electron temperature and density profiles obtained by the scanning MLP and their characteristic gradient scale lengths are shown in Figures 52 and 53 for the FY16 and FY15 campaigns, respectively.

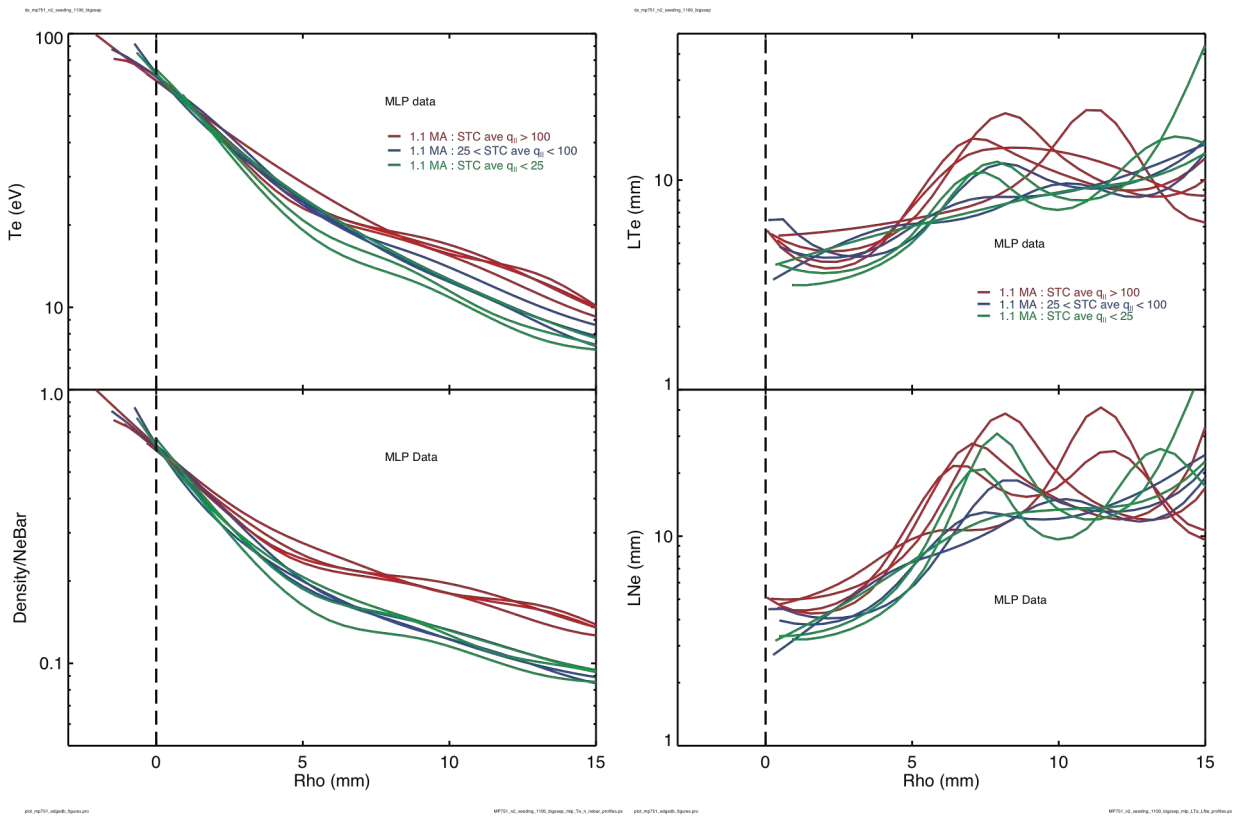

Figure 52. Electron temperature and normalized density profiles recorded by the scanning MLP from the FY16 campaign (left panels) and corresponding gradient scale lengths (right panels). Density profile data are normalized by core plasma line-averaged density (see values in top panel of Fig. 49). Rho is distance from the LCFS mapped to the outer midplane and corrected for EFIT mapping errors based on power balance. The electron temperature and density profiles are seen to steepen slightly near the separatrix as divertor dissipation is increased. The far SOL exhibits a pronounced reduction in electron temperature and density as the level of divertor dissipation is increased.

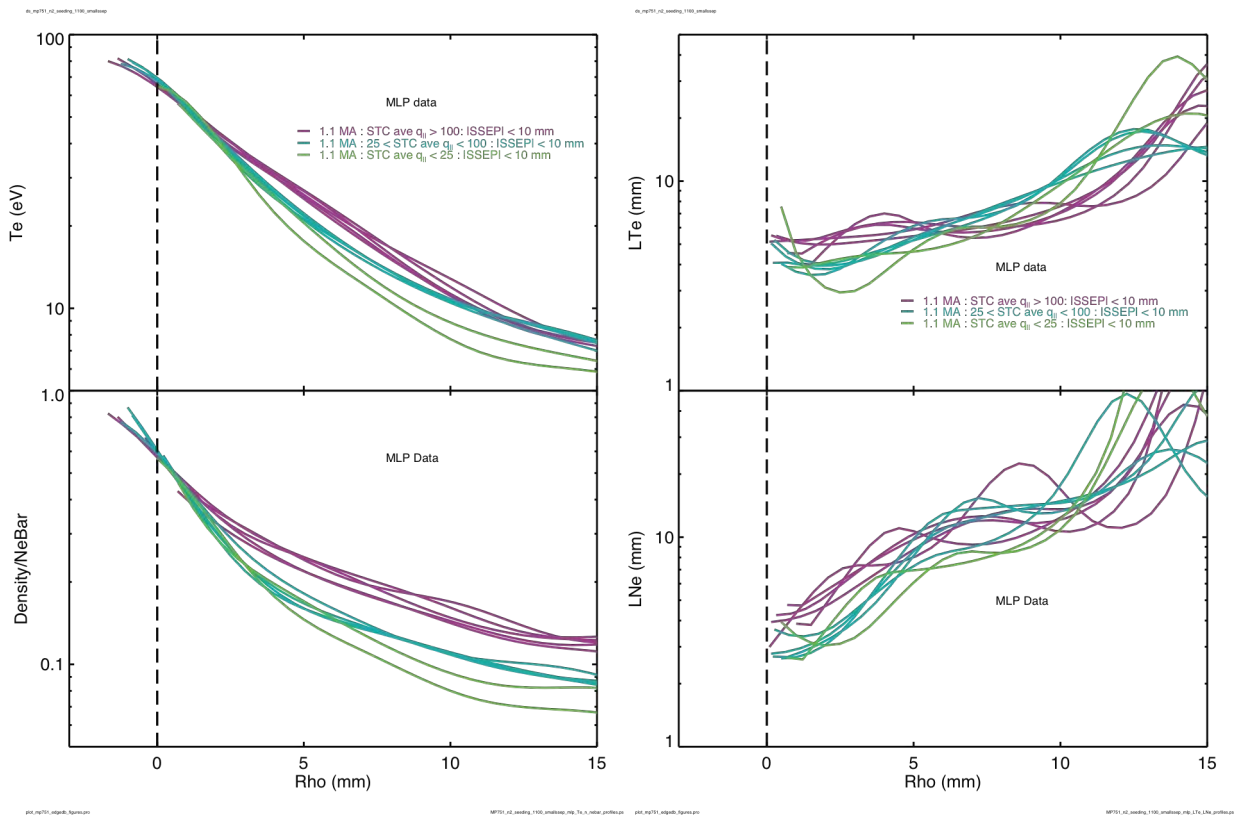

Figure 53. Same parameters as shown in Figure 51 for the FY15 campaign. A similar response to nitrogen seeding is detected: steepening of electron temperature and density profiles in near SOL; reduction of electron temperature and density in the far SOL.

These data are processed as follows. Electron temperature (Te) or density data (ne) from four electrodes on the scanning probe head (sampled at 1.1 MHz) are averaged together, effectively treating the four electrodes as a single electrode. These data are obtained as the probe head is scanned inward and outward across the SOL. The resultant time series is smoothed over a 200 μs window. The ρ coordinate corresponding to these data (i.e., the distance into the SOL mapped to the outer midplane) is determined from EFIT reconstruction, recognizing that there may be an offset in identifying the last closed flux surface (i.e., ρ = 0). The profiles are fitted with smooth spline curves and then sampled onto a regular ρ grid with spacing of 0.5 mm. Finally, the scanning probe profiles are shifted as needed to satisfy a power balance constraint: It is postulated that half of the power entering into the SOL (total input power minus core radiation, Psol) is conducted by electrons to the divertor volume. Since parallel electron heat flux scales as Te7/2, the separatrix electron temperature deduced by this procedure is insensitive to errors in estimating Psol. The resulting corrections in EFIT ρLCFS range from -2 to +6 mm.

Clear trends can be seen in the Te and ne profile data. Electron temperatures at and slightly inside the LCFS (ρ=0) are essentially unchanged with N2 seeding. However, as power flow onto the divertor target is decreased, Te and ne profiles just outside the LCFS tend to become steeper; Te and ne in the far SOL (ρ > 5 mm) are reduced. Results from the 2015 and 2016 campaigns are similar, although the Te and ne profiles are not identical across campaigns, which is likely a consequence of the different levels of upper and lower x-point flux balance (SSEP). The data with reduced |SSEP|, i.e., closer to double null, tend to have lower Te in the far SOL, which may be expected.

The right panels of Figures 52 and 53 show profiles of LTe and Lne corresponding to the data shown in the left panels. These are computed as $L_{Te} \sim T_e/(\partial T_e/\partial\rho)$, $L_{ne} \sim n_e/(\partial n_e/\partial\rho)$. Recognizing that a simple Spitzer heat conduction analysis for electron parallel flow yields $q_{||} \sim \frac{2}{7}\kappa_0 T_e^{7/2}/L_{||}$, LTe can be taken as a relative measure of the heat flux power e-folding width, $\lambda_q \sim 2L_{Te}/7$.

<u>Observations and initial conclusions from 1.1 MA dataset</u>

Despite a factor to 10 reduction in heat flux to the divertor target in response to N_2 seeding and a corresponding clear electrical disconnection of the divertor target from the main chamber SOL (as evidenced by the reduction in net currents to the divertor targets) the upstream density and temperature gradients are found to remain similar or slightly reduced compared to unseeded conditions. Thus, it appears that partial detachment of the divertor target does not significantly affect the SOL profiles and 'mitigate' the narrowness of the heat flux width as one might have hoped. If anything, these data suggest that the heat flux width becomes increasingly narrow as divertor dissipation is increased. However, as we will see, this trend is not reproduced in the 0.8 and 0.55 MA datasets analyzed below.

The reduction in T_e and n_e values in the far scrape-off layer with N_2 seeding is unexpected, although this phenomenon is consistent with the notion that cross-field heat and particle transport is decreased in these plasmas in response to N_2 seeding.

Data Analysis – 0.8 and 0.55 MA Plasmas

Magnetic equilibria for the 0.8 and 0.55 MA datasets were very similar to the 'ITER-like' case shown in the right panel in Figure 49 with |SSEP| values in the range of 4 to 10 mm. Data from these reduced current plasmas were analyzed in the same way as the 1.1 MA plasmas. Figures 54-59 show results in the same format as was shown for the 1.1 MA data.

Results from 0.8 MA Dataset

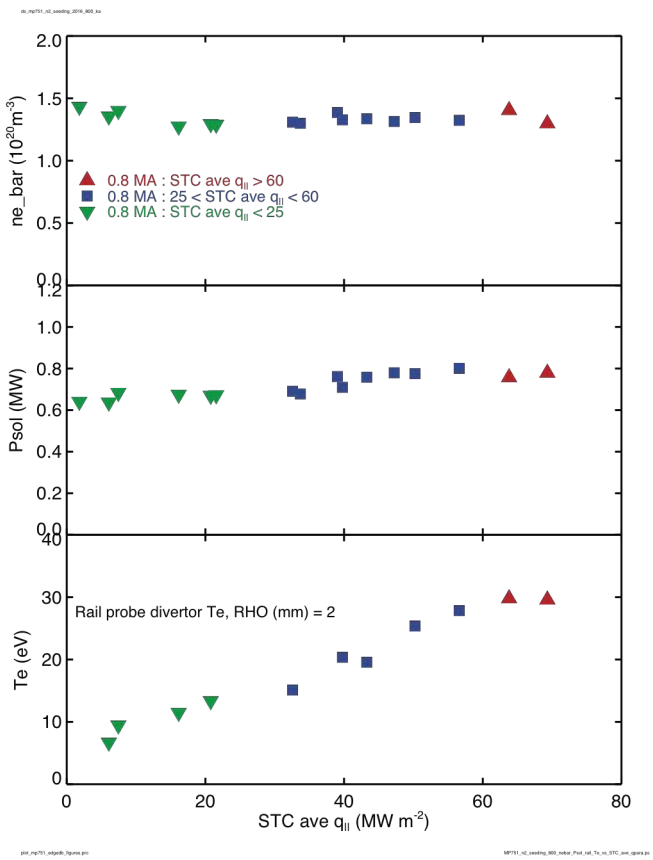

Figure 54. Line-averaged density (ne_bar), power entering into the scrape-off layer (P_{sol}) and divertor target electron temperatures versus parallel heat flux averaged over surface thermocouples on the outer divertor (STC ave $q_{//}$). These 16 samples are taken at the time that the scanning MLP records SOL profiles in near-identical 0.8 MA, 5.4 tesla ohmic heated plasmas. For each of these data sets, the level of divertor nitrogen seeding was the only external parameter that was varied. N_2 injection resulted in up to an order of magnitude reduction in power arriving that the outer divertor target while power into the SOL remained approximately constant; a minor reduction in P_{sol} is evident at the highest levels of N_2 seeding. Outer divertor target temperatures recorded by the Rail probes dropped substantially, indicating a transition from sheath-limited to high-recycling, approaching partially detached conditions. The different symbols and colors delineate relative power levels arriving on the outer divertor target. This color code and symbol scheme is retained in following plots.

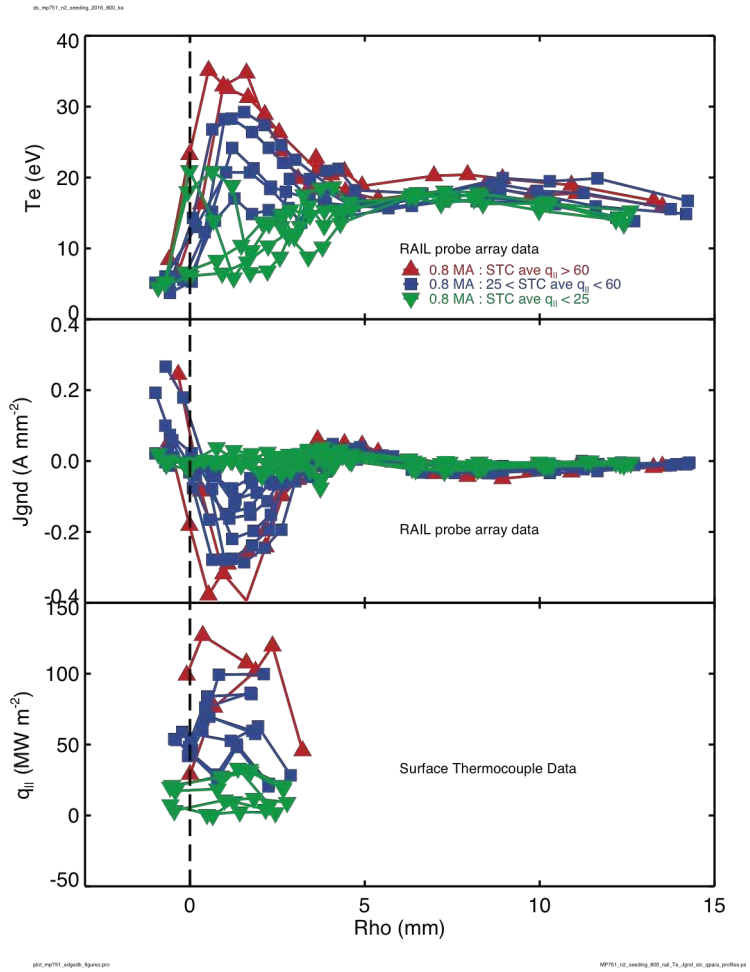

Figure 55. Profiles of outer divertor electron temperature and net parallel current density arriving at the plate as recorded by Rail probe array and parallel heat flux as inferred by surface thermocouple array. These data are from 0.8 MA plasmas. Plasma conditions near the strike point ($0 < \rho < 2$ mm) are strongly affected. Parallel heat fluxes near the strike point drop by an order of magnitude as divertor target conditions near the strike point change from sheath-limited (~30 eV) to high recycling to partially detached (~ 5 eV). Net parallel current density arriving at the plate drops by an order of magnitude indicating that the target plate becomes 'electrically disconnected' from the main chamber SOL plasma as the divertor achieves partial detachment.

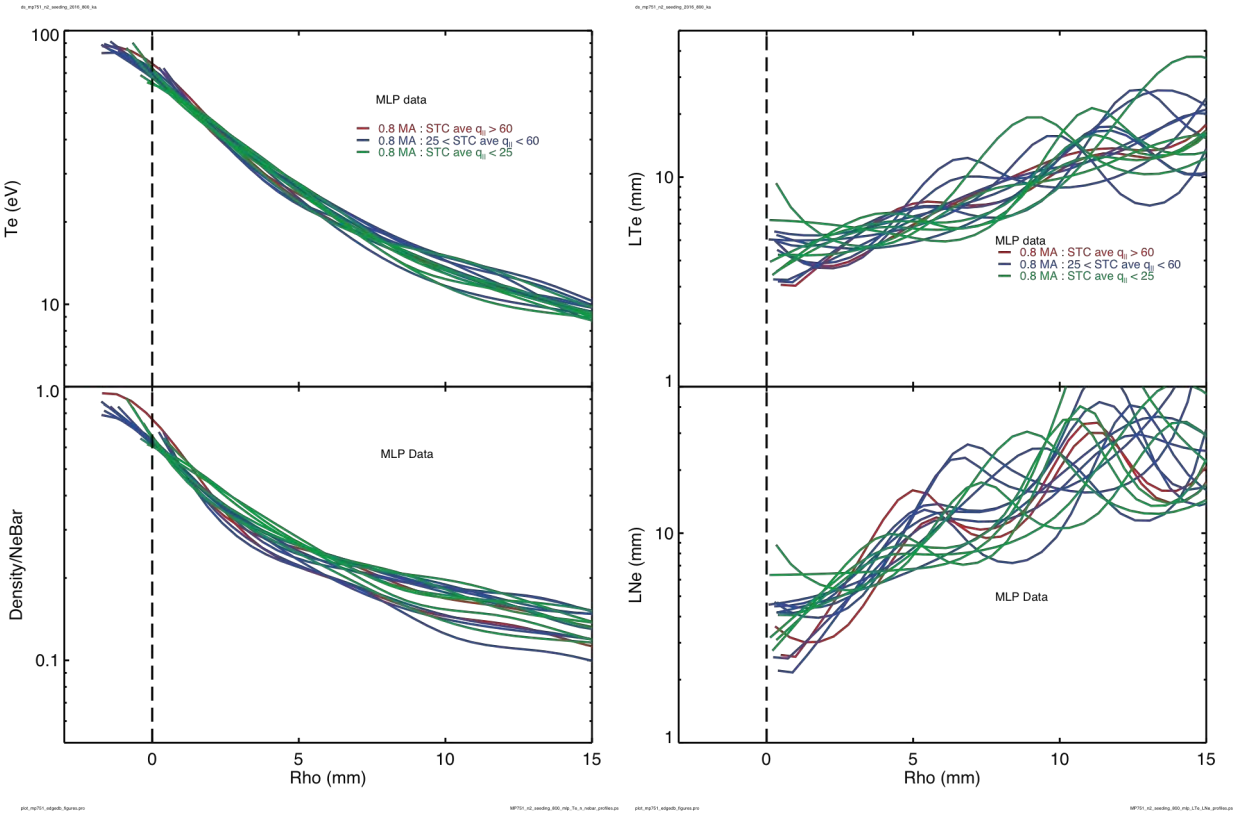

Figure 56. Electron temperature and normalized density profiles recorded by the scanning MLP (left panels) and corresponding gradient scale lengths (right panels). These data are from the 0.8 MA dataset. Density profile data are normalized by core plasma line-averaged density (see values in top panel of Fig. 53). Rho is distance from the LCFS mapped to the outer midplane and corrected for EFIT mapping errors based on power balance. Unlike the 1.1 MA data, electron temperature and density profiles appear to broaden slightly near the separatrix as divertor dissipation is increased. Also unlike the 1.1 MA data, far SOL does not experience a systematic change in density and electron temperature as the level of divertor dissipation is increased.

Results From 0.55 MA Dataset

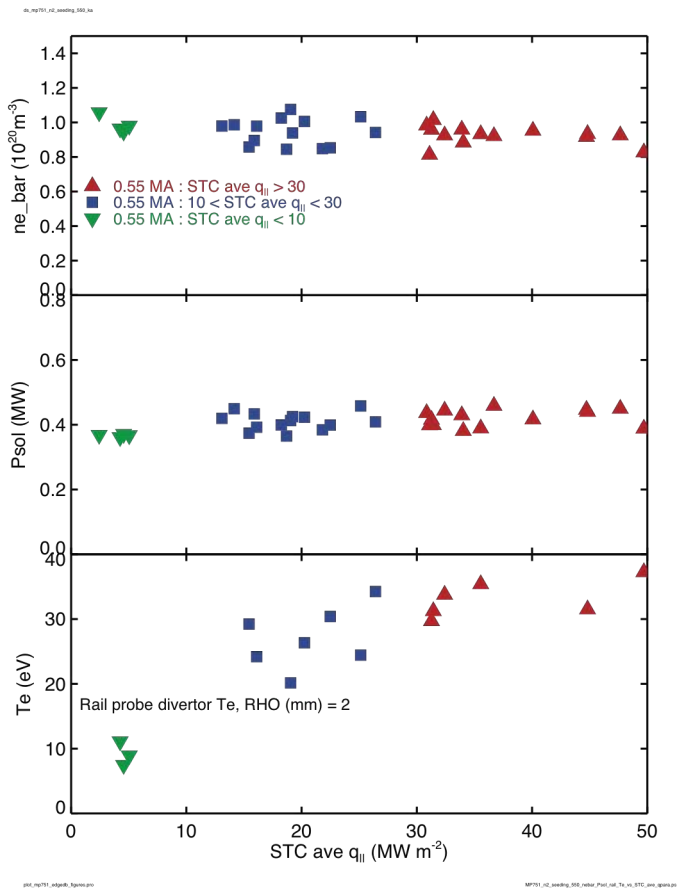

Figure 57. Line-averaged density (ne_bar), power entering into the scrape-off layer (P_{sol}) and divertor target electron temperatures versus parallel heat flux averaged over surface thermocouples on the outer divertor (STC ave $q_{//}$). These 32 samples are taken at the time that the scanning MLP records SOL profiles in near-identical 0.55 MA, 5.4 tesla ohmic heated plasmas. For each of these data sets, the level of divertor nitrogen seeding was the only external parameter that was varied. N_2 injection resulted in an order of magnitude reduction in power arriving at the outer divertor target while power into the SOL remained approximately constant. Outer divertor target temperatures recorded by the Rail probes dropped substantially, indicating a transition from sheath-limited to high-recycling, approaching partially detached conditions. The different symbols and colors delineate relative power levels arriving on the outer divertor target. This color code and symbol scheme is retained in following plots.

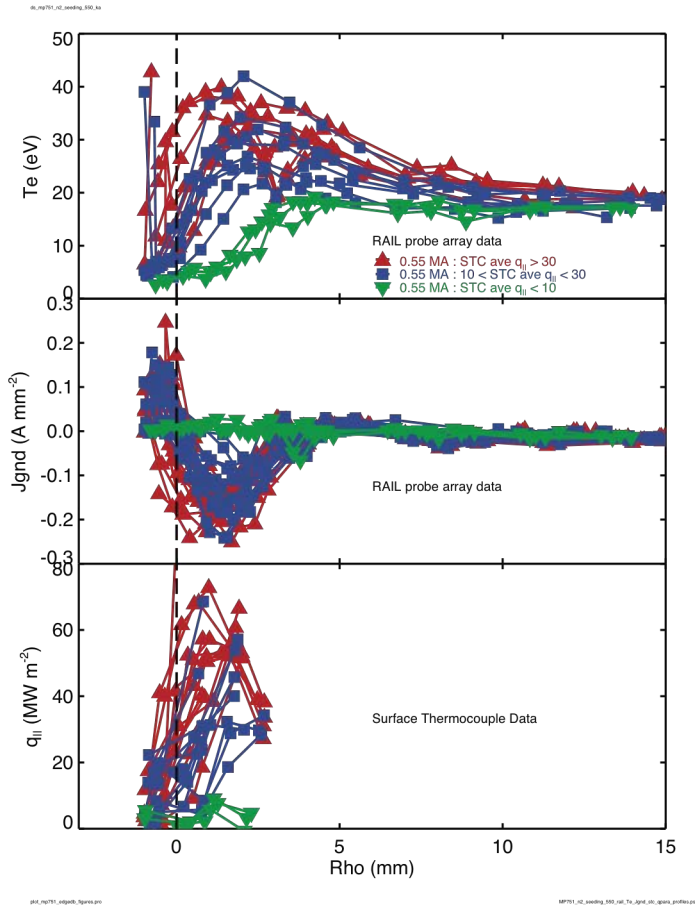

Figure 58. Profiles of outer divertor electron temperature and net parallel current density arriving at the plate as recorded by Rail probe array and parallel heat flux as inferred by surface thermocouple array. These data are from 0.55 MA plasmas. Plasma conditions near the strike point ($0 < \rho < 2$ mm) are strongly affected. Parallel heat fluxes near the strike point drop by an order of magnitude as divertor target conditions near the strike point change from sheath-limited (~40 eV) to high recycling to partially detached (~ 5 eV). Net parallel current density arriving at the plate drops by an order of magnitude indicating that the target plate becomes 'electrically disconnected' from the main chamber SOL plasma as the divertor achieves partial detachment.

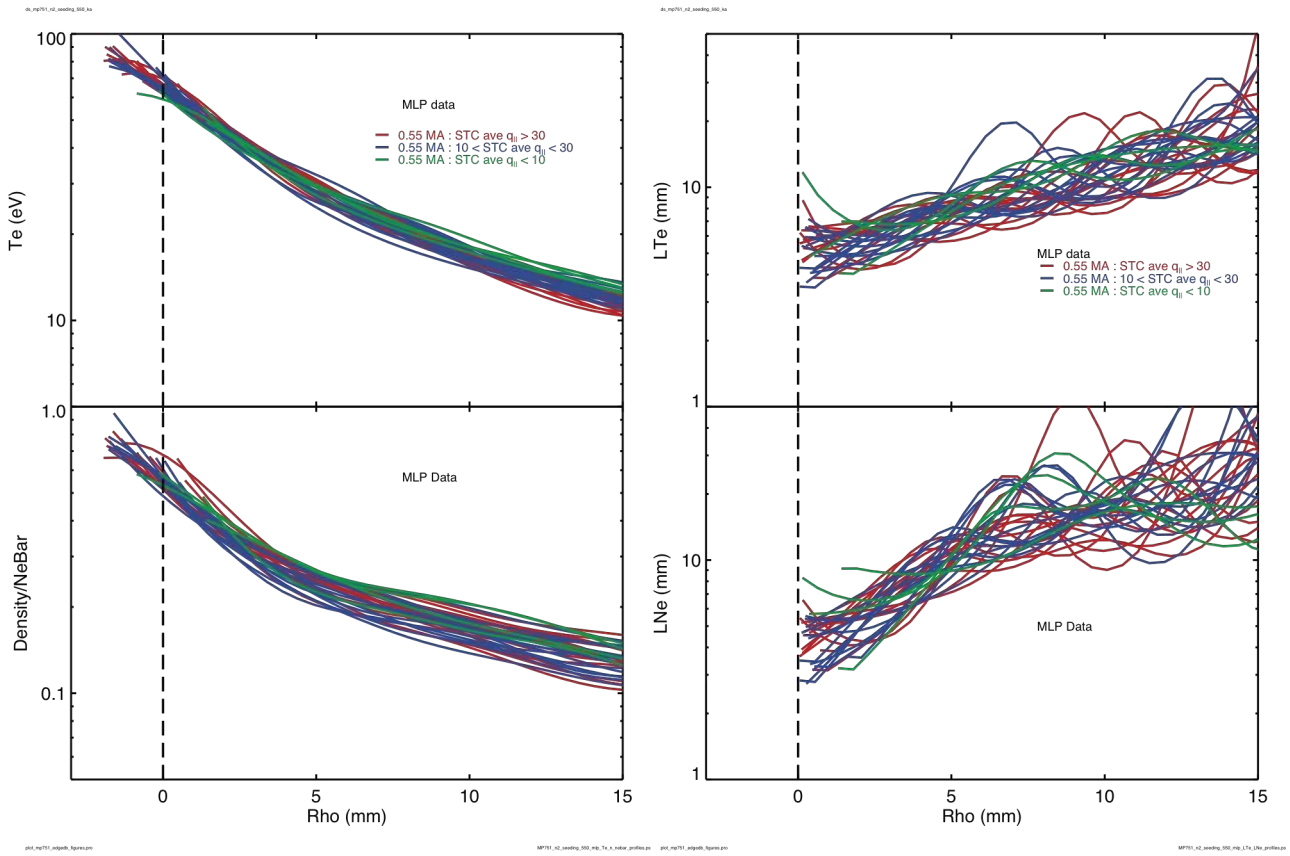

Figure 59. Electron temperature and normalized density profiles recorded by the scanning MLP (left panels) and corresponding gradient scale lengths (right panels). These data are from the 0.55 MA dataset. Density profile data are normalized by core plasma line-averaged density (see values in top panel of Fig. 56). Rho is distance from the LCFS mapped to the outer midplane and corrected for EFIT mapping errors based on power balance. Unlike the 1.1 MA data, electron temperature and density profiles do not appear to show any statistically significant variation with divertor nitrogen seeding. Also unlike the 1.1 MA data, far SOL does not experience a systematic change in density and electron temperature as the level of divertor dissipation is increased.

Summary and Initial Conclusions Based on Combined dataset

Our preliminary conclusions from the combined datasets (1.1 MA, 0.8 MA and 0.55 MA cases) are:

- In all cases studied, feedback controlled N2 seeding resulted in a factor of ~10 reduction in divertor target plate heat fluxes while maintaining core plasma conditions relatively unchanged.
- In response to seeding, divertor target conditions near the strike point changed from sheath-limited to high-recycling, approaching detachment. Electron temperatures near the strike point for the 0.55 MA dataset attained the lowest values, under 5 eV.
- Langmuir probe 'death ray' phenomena are detected in the 1.1 MA datasets – which is taken as evidence of being on the threshold of detachment based on previous studies in C-Mod.
- In all cases, net parallel current densities to the target plate were reduced by over an order of magnitude in response to nitrogen seeding. We interpret this observation in the following way: while the main chamber scrape-off was clearly 'electrically connected' to the divertor target plate without seeding, i.e., passing thermoelectric and Pfirsch-Schulter currents into the target plate, it was clearly 'electrically disconnected' for the highest levels of nitrogen seeding.
- Despite these dramatic changes in divertor conditions, upstream conditions at and slightly inside the LCFS remained largely unchanged for all plasma currents studied. However, some subtle and not-so-subtle differences in the scrape-off layer response are seen, based on the different plasma current cases:

Near SOL Response

- For the 1.1 MA dataset, there is a hint that electron temperature and density profiles steepen in the near SOL in response to N2 seeding, i.e., the upstream λ_q becomes narrower. On the other hand, SOL profiles for the 0.8 and 0.55 MA cases do not show this behavior. The 0.8 MA dataset indicates an increase in λ_q with seeding. These trends are summarized in Figure 60.

Far SOL Response

- For the 1.1 MA datasets (including small and large |SSEP| values), electron densities and temperatures in the far SOL are clearly reduced in response to divertor seeding. The physical mechanism(s) responsible for this behavior have not been identified at this time.

Finally, it is instructive to examine the relationship between λ_q and plasma currents in these discharges (Fig. 61). A trend of λ_q decreasing with increasing plasma current is clearly detected. But most importantly, within the scatter of these data, the influence of divertor nitrogen seeding is seen to be statistically insignificant.

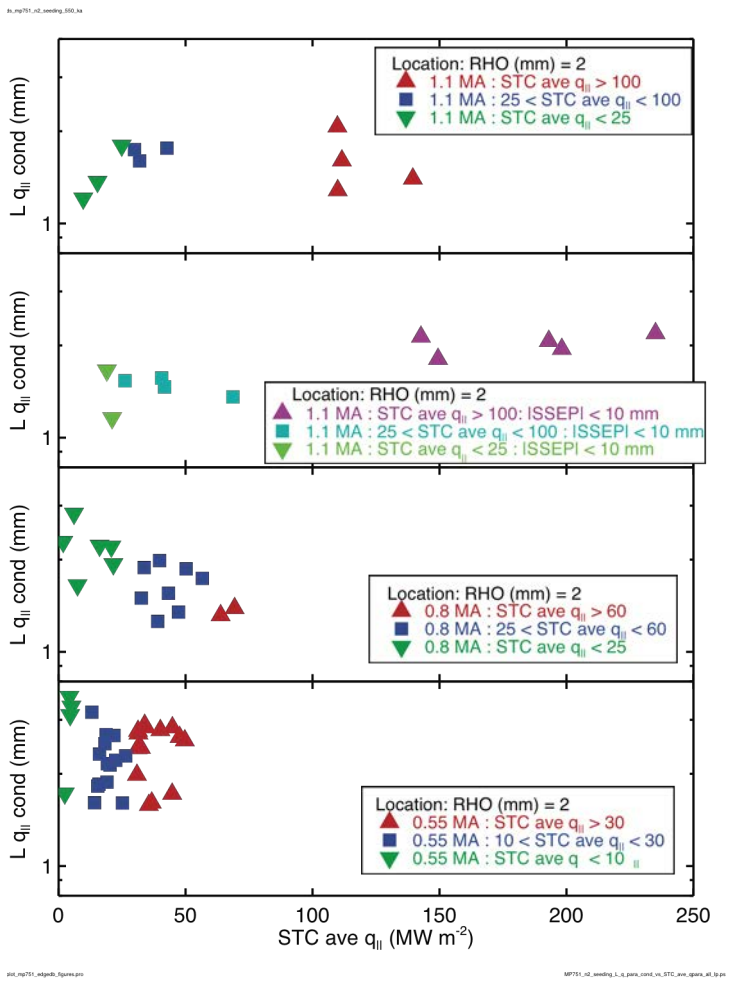

Figure 60. Electron heat flux power e-folding widths (λ_q) 2 mm into the scrape-off layer at the outer midplane versus average parallel heat flux arriving on divertor target for the four datasets studied. Here λ_q is taken to be proportional to the electron temperature e-folding length, $\lambda_q \sim 2L_{Te}/7$.

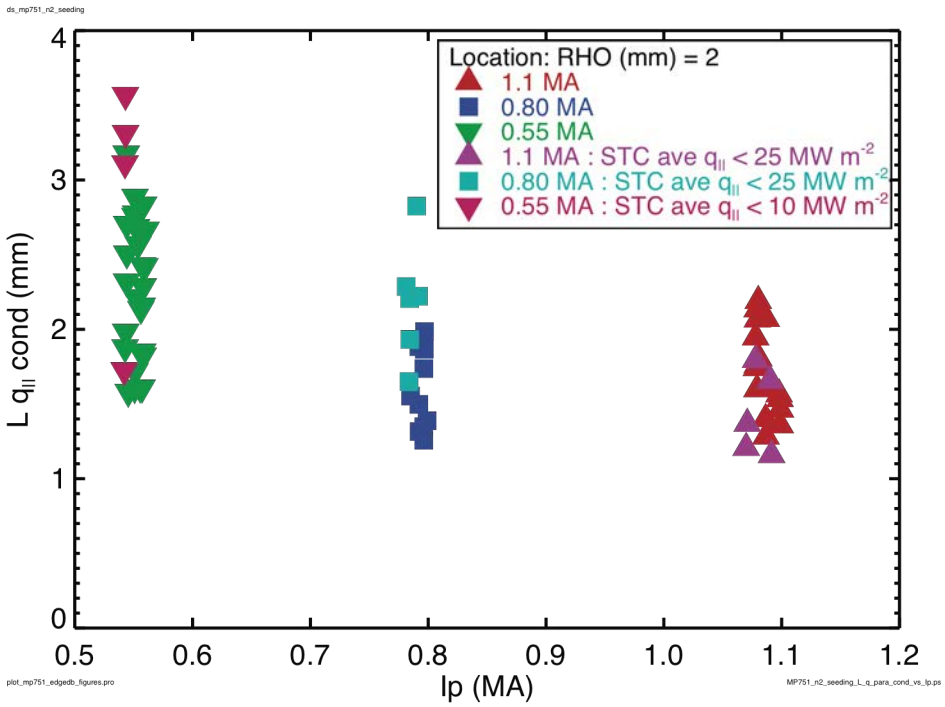

Figure 61. Electron heat flux power e-folding widths (λ_q) 2 mm into the scrape-off layer at the outer midplane versus plasma current. A trend of decreasing λ_q with increasing plasma current is evident. Considering the scatter in these data, the influence of divertor nitrogen seeding o λ_q is seen to be statistically insignificant.

Next Steps in Data Analyses

We are planning on presenting these initial observations at APS and PSI 2018 and publishing the results. At the same time, ongoing analysis will examine additional characteristics such as the behavior of fluctuations, plasma flows, transport fluxes, and plasma potentials upstream and a subset of these quantities at the target plate.

References

[1] V.A. Soukhanovskii, R. Maingi, C.E. Bush, R. Raman, R.E. Bell, R. Kaita, H.W. Kugel, C.J. Lasnier, B.P. LeBlanc, J.E. Menard, S.F. Paul, and A.L. Roquemore. “Divertor heat flux reduction and detachment experiments in NSTX”,J. Nucl. Mater., 363-365:432, 2007.

[2] V. A. Soukhanovskii, R. Maingi, D. A. Gates, J. E. Menard, S. F. Paul, R. Raman, A. L. Roquemore, M. G. Bell, R. E. Bell, J. A. Boedo, C. E. Bush, R. Kaita, H. W. Kugel, B. P. LeBlanc, D. Mueller, and the NSTX Team. “Divertor heat flux mitigation in the National Spherical Torus Experiment", *Phys. Plasmas*, 16, (2009).

[3] V. A. Soukhanovskii, R. Maingi, D. A. Gates , J. E. Menard, S. F. Paul, R. Raman, A. L. Roquemore, R. E. Bell, C. E. Bush, R. Kaita, H. W. Kugel, B. P. LeBlanc, D. Mueller, “Divertor Heat Flux Mitigation in High-Performance H-mode Plasmas in the National Spherical Torus Experiment", Nuclear Fusion, 49, 095025 (2009).

[4] V.A. Soukhanovskii, D.W. Johnson, R. Kaita, and A.L. Roquemore. “Electron density measurements in the National Spherical Torus Experiment detached divertor region using Stark broadening of deuterium infrared Paschen emission lines”, Rev. Sci. Instrum., 77:10127, 2006.

[5] F. Scotti, V.A. Soukhanovskii, M.L. Adams, H.A. Scott, H. W. Kugel, R. Kaita and A.L. Roquemore, “Observation and modeling of inner divertor re-attachment in discharges with lithium coatings in NSTX”, Journal of Nuclear Materials, Volume 415, Issue 1, Supplement, 1 August 2011, Pages S405-S408

[6] Maingi, R; Bush, CE; Kaita, R, *et al*. "Divertor heat flux scaling with heating power and plasma current in H-mode discharges in the National Spherical Torus eXperiment", *J. Nucl. Mater.*, **363**, 196-200, (2007).

[7] T. K. Gray, R. Maingi, V. A. Soukhanovskii, J. E. Surany, J.-W. Ahn, and A. G. McLean, “Dependence of divertor heat flux widths on heating power, flux expansion, and plasma current in the NSTX”, J. Nucl. Mater., vol. 415, no. 1, pp. S360–S364, 2011.

[8] V.A.Soukhanovskii, R.Maingi, R.E.Bell, C.E.Bush, D.A.Gates, R.Kaita, H.W.Kugel, B.P.LeBlanc, R.Maqueda, J.E.Menard, D.Mueller, S.F.Paul, R.Raman, A.L.Roquemore, “High flux expansion divertor studies in NSTX”, in 36th EPS Conf. on Plasma Phys., Sofia, Bulgaria, 2009, Paper P2.178, http://arxiv.org/abs/0912.4281.

[9] M. A. Makowski, D. Elder, T. K. Gray, B. LaBombard, C. J. Lasnier, A. W. Leonard, R. Maingi, T. H. Osborne, P. C. Stangeby, J. L. Terry, and J. Watkins, “Analysis of a multi-machine database on divertor heat fluxes”, Phys. Plasmas **19**, 056122 (2012)

[10] Final Report on the DOE OFES FY 2010 Joint Research Target on thermal SOL transport research, by Alcator C-Mod, DIII-D and NSTX staff

[11] T. K. Gray, et al. J. Nucl. Mater. **415** (2011) S360-S364

[12] R. Maingi, et al. J. Nucl. Mater. **337-339** (2005) 727-731

[13] J.-W. Ahn, et al. Rev. Sci. Instrum. **81** (2010) 023501

[14] A.G. McLean, et al. Rev. Sci. Instrum. **83** (2012) 053706

[15] T. Eich, et al. Phys. Rev. Lett. **107** (2011) 215001

[16] J.R. Harrison, et al. J. Nucl. Mater. **438** (2013) S375-S378

[17] M. Podesta, et al. Nucl. Fusion. **52** (2012) 033008

[18] LaBombard, B., Terry, J.L., Hughes, J.W., Brunner, D., Payne, J., Reinke, M.L., Cziegler, I., Granetz, R., Greenwald, M., Hutchinson, I.H., Irby, J., Lin, Y., Lipschultz, B., Ma, Y., Marmar, E.S., Rowan, W.L., Tsujii, N., Wallace, G., Whyte, D.G., Wolfe, S., Wukitch, S., Wurden, G., and Alcator C-Mod Team, "*Scaling of the power exhaust channel in Alcator C-Mod*," Phys. Plasmas **18** (2011) 056104.

[19] Eich, T., Leonard, A.W., Pitts, R.A., Fundamenski, W., Goldston, R.J., Gray, T.K., Herrmann, A., Kirk, A., Kallenbach, A., Kardaun, O., Kukushkin, A.S., LaBombard, B., Maingi, R., Makowski, M.A., Scarabosio, A., Sieglin, B., Terry, J., Thornton, A., ASDEX Upgrade Team, and JET EFDA Contributors, "*Scaling of the tokamak near the scrape-off layer H-mode power width and implications for ITER*," Nuclear Fusion **53** (2013) 093031.

[20] Goldston, R.J., "*Heuristic drift-based model of the power scrape-off width in low-gas-puff H-mode tokamaks*," Nucl. Fusion **52** (2012) 013009 (7 pp.).

[21] Chang, C.S., Ku, S., Loarte, A., Parail, V., Köchl, F., Romanelli, M., Maingi, R., Ahn, J.W., Gray, T., Hughes, J., LaBombard, B., Leonard, T., Makowski, M., and Terry, J., "*Gyrokinetic projection of the divertor heat-flux width from present tokamaks to ITER*," Nucl. Fusion **57** (2017) 116023.

[22] Terry, J.L., LaBombard, B., Brunner, D., Payne, J., and Wurden, G.A., "*Divertor IR thermography on Alcator C-Moda)*," Review of Scientific Instruments **81** (2010.

[23] Eich, T., Sieglin, B., Scarabosio, A., Fundamenski, W., Goldston, R.J., Herrmann, A., and Team, A.U., "*Inter-ELM Power Decay Length for JET and ASDEX Upgrade: Measurement and Comparison with Heuristic Drift-Based Model*," Physical Review Letters **107** (2011) 215001.

[24] Brunner, D., Burke, W., Kuang, A.Q., LaBombard, B., Lipschultz, B., and Wolfe, S., "*Feedback system for divertor impurity seeding based on real-time measurements of surface heat flux in the Alcator C-Mod tokamak*," Rev. Sci. Instrum. **87** (2016) 023504.

[25] LaBombard, B. and Lyons, L., "*Mirror Langmuir probe: A technique for real-time measurement of magnetized plasma conditions using a single Langmuir electrode*," Rev. Sci. Instrum. **78** (2007) 073501.

[26] LaBombard, B., Golfinopoulos, T., Terry, J.L., Brunner, D., Davis, E., Greenwald, M., Hughes, J.W., and Alcator C-Mod Team, "*New insights on boundary plasma turbulence and the quasi-coherent mode in Alcator C-Mod using a Mirror Langmuir Probe*," Phys. Plasmas **21** (2014) 056108.

[27] Brunner, D., Kuang, A.Q., LaBombard, B., and Burke, W., "*Linear servomotor probe drive system with real-time self-adaptive position control for the Alcator C-Mod tokamak,*" Rev. Sci. Instrum. **88** (2017) 073501.

[28] Kuang, A.Q., Brunner, D., LaBombard, B., Leccacorvi, R., and Vieira, R., "*Design and operation of a high-heat flux, flush-mounted 'rail' Langmuir probe array on Alcator C-Mod,*" Nuclear Materials and Energy (2016.

[29] Brunner, D., Umansky, M.V., LaBombard, B., and Rognlien, T.D., "*Divertor 'death-ray' explained: An artifact of a Langmuir probe operating at negative bias in a high-recycling divertor,*" J. Nucl. Mater. **438** (2013) S1196.